# An Investigation of the Electronic and Catalytic Properties of Ceria Nanocubes

A Thesis Submitted to the College of

Graduate Studies and Research

in Partial Fulfillment of the Requirements

for the Degree of Master of Science

in the Department of Chemistry

University of Saskatchewan

Saskatoon

By

MICHELLE NICOLE REVOY

# Permission to Use

In presenting this thesis/dissertation in partial fulfillment of the requirements for a Postgraduate degree from the University of Saskatchewan, I agree that the Libraries of this University may make it freely available for inspection. I further agree that permission for copying of this thesis/dissertation in any manner, in whole or in part, for scholarly purposes may be granted by the professor or professors who supervised my thesis/dissertation work or, in their absence, by the Head of the Department or the Dean of the College in which my thesis work was done. It is understood that any copying or publication or use of this thesis/dissertation or parts thereof for financial gain shall not be allowed without my written permission. It is also understood that due recognition shall be given to me and to the University of Saskatchewan in any scholarly use which may be made of any material in my thesis/dissertation.

Requests for permission to copy or to make other uses of materials in this thesis/dissertation in whole or part should be addressed to:

Head of the Department of Chemistry

University of Saskatchewan

Saskatoon, Saskatchewan S7N 5C9

Canada

# Abstract

The focus of this thesis was on the synthesis, characterization and application of ceria nanocubes. This thesis is divided into two main sections; the first section investigates the electronic properties of ceria nanocubes, and the second explores their catalytic applications towards alcohol oxidation reactions.

The first project of this thesis consisted of the X-ray characterization of hydrothermally synthesized ceria nanocubes of various sizes. For the first time, the electronic properties of such nanocubes were systematically studied using high resolution XPS and XANES. It was found that the concentration of $Ce^{3+}$ present within the nanocubes was independent of the particle size, as well as the Ce precursor used during synthesis. Throughout the analysis of the Ce 3d and 4d XPS spectra, it was observed that the surface of the ceria nanocube samples was undergoing photoreduction/damage over time. This damage was attributed to the samples' exposure to high intensity X-ray radiation. This was confirmed through examination of the Ce $M_{4,5}$- and $N_{4,5}$-edge XANES spectra. From these results, it was clear that the concentration of $Ce^{3+}$ on the surface of the ceria nanocubes was independent of particle size. This fact may become important when investigating their potential catalytic activity.

The second project of this thesis concentrated on the analysis of the catalytic activity of a variety of $CeO_2$, Au and $Au/CeO_2$ catalysts towards the oxidation of benzyl alcohol. The low temperature oxidation reactions were studied using $^1H$ NMR spectroscopy. It was observed that Au NPs, Au/bulk $CeO_2$, and $Au/CeO_2$ nanocubes in water and $K_2CO_3$ were active catalysts for this oxidation reaction at 60°C in both air and $O_2$ (g) atmospheres. Surprisingly, however, the Au/bulk $CeO_2$ and $Au/CeO_2$ nanocube catalysts showed very similar activities. It was also found that ceria nanocubes alone, and $Au_{25}(SR)_{18}$/bulk $CeO_2$ showed no activity for this reaction under similar conditions. It was determined that below a substrate to catalyst ratio of ~ 1500:1, the $Au/CeO_2$ catalysts, which showed the highest activities, were mass-transport limited with respect to the $O_2$ in the system. The turnover frequencies of the supported catalysts were approximately double those of the unsupported NPs. Furthermore, these reactions have indicated that activating $Au_{25}(SR)_{18}/CeO_2$ for catalysis is a non-trivial task, and more work needs to be done to understand the activation of such clusters.

# Acknowledgements

There are many people that I would like to thank for getting me through these past 2 years. First, I would like to thank my family and friends who have always supported me and given me constant encouragement throughout my academic career. I want to thank you for keeping me on the right track and pushing me to succeed.

I would especially like to thank both of my thesis supervisors, Dr. Andrew Grosvenor and Dr. Robert Scott. I appreciate all of the work you have put into making me a better chemist, a better technical writer, and overall a better researcher. Thank you for all of your wisdom and support throughout this project, as well as with unpleasant life events. Even though it was difficult at times to have two very different supervisors, I believe that it has allowed me to grow and thrive as an individual.

I would be remise if I did not thank all of the past and present Grosvenor and Scott group members. I would particularly like to thank John Hayes, James Walker and Esther Aluri for helping in the collection of the XANES data presented in Chapter 2. Atal Shivhare is also thanked for his assistance and encouragement during the initial stages of my catalytic work, presented in Chapter 3, and with the synthesis of the $Au_{25}(SR)_{18}$ MPCs.

Throughout this thesis, there have been many other notable scientists who have provided me with some much appreciated guidance. Dr. Tim Kelly is thanked for the use of his shiny new laboratory, including the use of the Thermo Scientific Sovall Biofuge Primo centrifuge used during synthesis, as well as the ultra-sonicator, vortex mixer and rotary evaporator. Dr. Guosheng Liu is thanked for assisting with the operation of the Philips CM10 TEM, located in the Biology department, University of Saskatchewan, as well as with the development of the TEM film. Dr. Dimitre Karpuzov and Dr. Shihong Xu from the Alberta Centre for Surface Engineering and Science (ACSES) at the University of Alberta are thanked for helping in the collection of the XPS spectra. Dr. Tom Regier and Dr. Lucia Zuin are thanked for helping with the soft X-ray XANES experiments using the SGM (11ID-1) and VLS-PGM (11ID-2) beamlines at the CLS. Dr. Ning Chen is thanked for the help in collecting the hard X-ray XANES and EXAFS experiments using the HXMA (06ID-1) beamline at the CLS. Dr. Keith Brown is

thanked for the training and help using the 500 MHz NMR spectrometer located at the Saskatchewan Structural Sciences Centre (SSSC).

Lastly, I would like thank the organizations who provided funding for the work done in this thesis. The Natural Sciences and Engineering Research Council (NSERC) of Canada is thanked for their support in the form of Discovery awards held by Dr. Robert Scott and Dr. Andrew Grosvenor. The Canadian Foundation for Innovation (CFI) is thanked for funding the purchase of the PANalytical Empyrean powder X-ray diffractometer used in this work. The CLS is supported by NSERC, the National Research Council of Canada, the Canadian Institutes of Health Research, the Province of Saskatchewan, Western Economic Diversification Canada, and the University of Saskatchewan.

# Table of Contents

**Chapter 3**

**Catalytic Performance of Ceria NCs and Au/$CeO_2$ Composites towards Benzyl Alcohol Oxidation Reactions**

# List of Tables

# List of Figures

# List of Abbreviations

| | |
|---|---|
| ACSES | Alberta Centre for Surface Engineering and Science |
| $Au/CeO_2$ | Gold Supported on Ceria |
| BE | Binding Energy |
| BF | Bright Field |
| CLS | Canadian Light Source |
| CN | Coordination Number |
| CTAB | Cetyltrimethylammonium Bromide |
| DF | Dark Field |
| EELS | Electron Energy Loss Spectroscopy |
| EXAFS | Extended X-ray Absorption Fine Structure |
| FCC | Face Centered Cubic |
| FWHM | Full Width at Half Maximum |
| FY | Fluorescence Yield |
| HXMA | Hard X-ray Micro-Analysis |
| IMFP | Inelastic Mean Free Path |
| KE | Kinetic Energy |
| MPC | Monolayer Protected Cluster |
| NC | Nanocube |
| NP | Nanoparticle |
| NR | Nanorod |
| OLA | Oleic Acid |
| OSC | Oxygen Storage Capacity |
| PFY | Partial Fluorescence Yield |
| PVP | Polyvinylpyrrolidone |
| SGM | Spherical Grating Monochromator |
| SOFC | Solid Oxide Fuel Cell |
| SR | Thiolate Ligands [Ch. 3: Phenylethanethiolate ligands] |
| SSSC | Saskatchewan Structural Sciences Centre |
| TEM | Transmission Electron Microscopy |

| | |
|---|---|
| TEY | Total Electron Yield |
| TFY | Total Fluorescence Yield |
| TGA | Thermogravimetric Analysis |
| THF | Tetrahydrofuran |
| TOF | Turnover Frequency |
| TWC | Three Way Catalyst |
| UHV | Ultra-High Vacuum |
| VLS-PGM | Variable Line Spacing – Plane Grating Monochromator |
| XRD | X-ray Diffraction |
| XANES | X-ray Absorption Near-Edge Spectroscopy |
| XAS | X-ray Absorption Spectroscopy |
| XPS | X-ray Photoelectron Spectroscopy |

# Chapter 1

# Introduction

## 1.1. Cerium Oxide

Cerium (Ce) has a ground state electronic configuration of [Xe] $6s^2$ $5d^1$ $4f^1$ and is the most abundant of the rare earth elements.[1] Cerium is even more abundant in the Earth's crust (66.5 ppm) than copper (60 ppm) and lithium (20 ppm).[1] Cerium has two common (stable) valence states, $Ce^{3+}$ and $Ce^{4+}$, which contribute to the unique properties associated with cerium-based materials. Of these materials, $CeO_2$ (ceria) has been researched the most. Ceria has a cubic fluorite ($CaF_2$) crystal structure with a space group of $Fm\bar{3}m$.[2] The face-centered cubic (fcc) structure of ceria is shown in Figure 1.1.

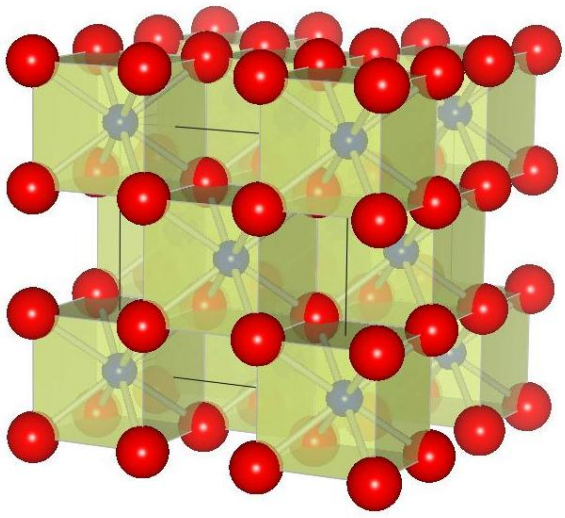

**Figure 1.1:** Crystal structure of $CeO_2$ ($Ce^{4+}$ ions are in blue; $O^{2-}$ ions are in red).

The $Ce^{4+}$ ions have a cubic closed packing arrangement, and are located at the corner and face centered positions of the unit cell, while the oxide ions ($O^{2-}$) occupy the tetrahedral sites. The octahedral sites within the unit cell remain vacant. A single unit cell consists of 4 $Ce^{4+}$ ions and 8 $O^{2-}$ ions (Z = 4). This fluorite structure can exhibit surface defects depending on the partial pressure of oxygen in the system.[1] It has been widely accepted that the reactivity of ceria can be related to the $Ce^{3+}$ / $Ce^{4+}$ redox couple ($E^o$ = -1.44 V) which allows for the easy reduction / oxidation of ceria under various conditions.[2] Under reducing conditions, ceria is known to form non-stoichiometric oxides having the basic formula of $CeO_{2-x}$ where $0 < x < 0.5$.[2] The partial pressure of oxygen will dictate how readily the Ce ions can reversibly switch between valence states, through the following equation:

$$CeO_2 \rightleftarrows CeO_{2-x} + \frac{x}{2} O_2 \qquad (1.1)$$

The amount of oxygen that is released and / or consumed during the reaction is referred to as the oxygen storage capacity (OSC) of the material.[2] These unique redox properties allow ceria to have many industrially and commercially important applications.

## 1.1.1. Applications

Ceria is a technologically important material because of its wide spread applications in the fields of catalysis,[3,4] oxygen storage,[5] fuel cells,[6,7] gas sensors,[8] self-cleaning ovens[9] and even sun-care products.[10] This section will focus on several examples of relevant ceria-based applications.

### 1.1.1.1. Three-Way Catalysts

Since the early 1980s, ceria has been employed in three-way catalytic (TWC) systems as an effective automotive pollution control method.[11] The development of TWCs was dictated by the need to simultaneously convert $NO_x$(g), CO(g) and other hydrocarbons from automobile exhaust into harmless $N_2$(g), $CO_2$(g) and $H_2O$(g), hence the name 'three-way' catalyst.[11] In order for the TWC to operate within vehicle emission control systems (catalytic converters), it must be able to operate at low to moderate temperatures, withstand thermal treatment up to 1000 °C, and

be responsive even under sulfur and lead poisoning (deactivating) conditions.[12] The impressive OSC and redox properties of ceria are the motivation for its use in such systems as it is directly linked to the efficiency of the TWC. Even though ceria-based TWCs have been used for decades, ceria's role is still ill-defined as multiple effects have been shown to occur. Ceria has been suggested to increase the stability of an $Al_2O_3$ support; to promote dispersion of supported noble metal nanoparticles (NPs); to store and release oxygen under various conditions; to promote CO oxidation and the water gas shift reaction; and show increased catalytic activity at the metal-support interface.[11,13] Mixed oxides, such as $(CeO_2)_x(ZrO_2)_{1-x}$ and noble metal supported $(CeO_2)_x(ZrO_2)_{1-x}$ materials, have been observed to have faster oxygen diffusion rates than in pure ceria-based systems.[13] The addition of $ZrO_2$ into the TWC system has shown to increase the thermal stability of the surface area and overall OSC.[11] Most current TWCs consist of several different active phases mainly composed of noble metal NPs, ceria-based oxides, and alumina.[12] As diesel engines were traditionally thought to be a cleaner / greener alternative to gasoline powered vehicles, the removal of $NO_x$ and soot (solid particulate matter) from their exhaust fumes has also been of significant research.[12] The pursuit of new effective removal techniques is an important current scientific and environmental challenge.

### 1.1.1.2. Solid Oxide Fuel Cell Technology

Ceria-based materials have also been employed in solid oxide fuel cell (SOFC) technology. This class of fuel cells has gained considerable attention due to their potential for providing green and reliable electrical power.[1] SOFCs produce electricity through the electrochemical combination of fuel and an oxidant across an ionic conducting solid oxide electrolyte.[14] In SOFCs, the electrolyte facilitates the migration of the oxide ions from the cathode to the anode where they react with a fuel ($H_2$, CO, hydrocarbons, etc.) to generate electricity.[15] In order for the cells to operate, they must be run at elevated temperatures to enable the successful migration of oxide ions through the electrolyte. At these elevated temperatures, although the direct oxidation of hydrocarbons is possible, there is an increased possibility of deactivation due to carbon deposition on the anode.[16] It has been reported that ceria can be used as an efficient oxygen ion-conductor within a cell.[1] In 2000, SOFCs containing a composite anode of copper and ceria (or samaria ($Sm_2O_3$)-doped ceria) were the first to show the direct

electrochemical oxidation of hydrocarbon fuels at 700 °C and 800 °C. [16] Copper was used as the current collector and to reduce the amount of carbon deposition on the anode, while ceria was used to increase the activity of the oxidation reactions and promote higher ionic conductivity.[1,16] It has been previously shown that the impressive redox capabilities of ceria can be used to increase the activity of a variety of catalytic reactions.[1] The aforementioned $Cu/CeO_2$ anodes had the advantage of being highly sulfur tolerant and also demonstrated high redox stability.[1] More recently, micro- and nano-structured ceria have also been implemented within cell structures to try to increase the overall efficiency.[1] Nevertheless, research in the field is still on-going with the aim to produce more efficient, greener fuel cells.

### 1.1.1.3. Self-Cleaning Oven Technology

As mentioned in the previous sections, the unique redox properties of ceria allow for a multitude of potential applications. The final example to be discussed in this section involves its use in self-cleaning oven technology. Recent developments in this technology have been prompted by manufacturers seeking to out-rank / top their competition.[9] In general, self-cleaning ovens can be separated into two categories: pyrolytic and catalytic.[9] Commonly, the main type of commercially available self-cleaning ovens are pyrolytic in nature and operate at high temperatures (> 500 °C).[9] More modern ovens utilize a catalytic cleaning process which can occur over a lower temperature range, therefore conserving energy and production costs.[9] A plethora of materials have been studied for uses in such ovens, and ceria catalysts have proven to be quite effective. The role of the ceria catalyst is to promote the combustion of carbonaceous materials which have adhered to the oven window.[9] The use of powdered ceria coatings has lowered the self-cleaning operation temperature by up to 100 °C, and las led to reduced CO emissions compared to conventional pyrolytic ovens.[9] It is clear from the aforementioned examples that ceria-based materials are extremely useful in both industrial and commercially relevant applications.

## 1.2. Ceria Nanostructures

Recently, the many uses of ceria NPs have been investigated as their properties are quite different from those of the bulk material. Oxygen defects, as well as the presence of $Ce^{3+}$ have been observed within the crystal structure of ceria NPs.[1,17] The degree of oxygen defects / vacancies at the surface of the NPs affect how easily the NPs can reversibly absorb and release oxygen, *i.e.* the OSC.[2] It has been reported that various shapes and sizes of ceria NPs can be synthesized through a variety of methods, including hydrothermal,[18] solvothermal,[17] precipitation,[19] micro-emulsion,[19] thermal decomposition,[20] sol-gel,[21] and microwave heating methods.[22] This section will describe different approaches that can be used to synthesize ceria NPs as well as the possible growth mechanisms for achieving different NP shapes and sizes.

### 1.2.1. Nanoparticle Synthesis

There are two basic methods used to synthesize nanomaterials: top-down or bottom-up approaches. The principle behind the two methodologies is different, yet they both yield particles which can be measured on a nanometer scale. The top-down approach involves mechanically breaking down the bulk material until nanostructures or NPs are formed. The bottom-up approach chemically builds up the materials from the bottom, *i.e.* atom-by-atom or cluster-by-cluster, usually using metal precursors.[23] Both approaches have their advantages and disadvantages depending on the desired final nanostructured product. A schematic diagram illustrating the differences between the top-down and bottom-up NP syntheses is presented in Figure 1.2.

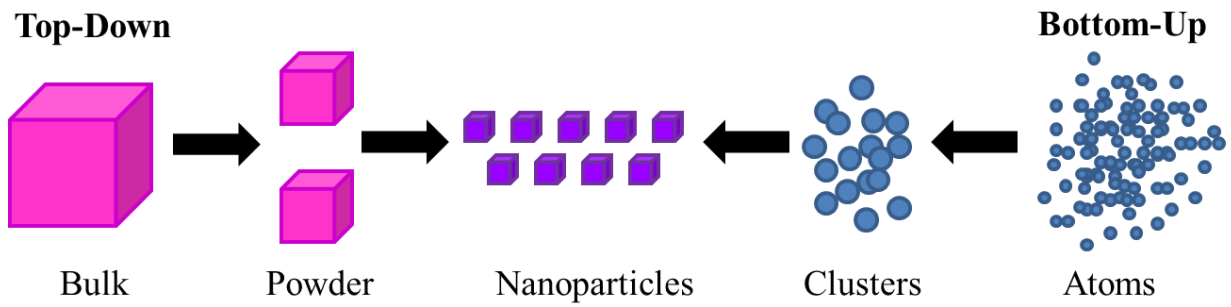


**Figure 1.2:** Schematic diagram of the top-down and bottom-up approaches for NP synthesis.

NP synthesis via the top-down approach is by far the simplest way to achieve nanomaterials. However, mechanically-based techniques are not widely used in the field as the resulting nanostructures are often polydisperse in both size and shape. Due to the harsh nature of the synthesis, imperfections or defects can also form on the surfaces of the obtained NPs.[23] These imperfections are formed during the breaking down of the bulk material as this introduces stress into the system. Both the physical and chemical properties of the NPs are significantly impacted by these defects. Lithographic techniques, film deposition and growth, laser beam processing, and mechanical techniques (*e.g.* ball milling), are examples of top-down NP syntheses.[24] Ideally, to study the obtained NPs, they should be monodisperse with respect to their size and shape, have identical chemical compositions and crystal structures, and be well dispersed within the reaction media.[23] For these reasons, the bottom-up approach is preferred amongst synthetic chemists.

The bottom-up approach promises a better chance to obtain NPs having the desired characteristics. There is a wealth of synthetic techniques available which utilize the principle of building up the NPs from common precursors; hydrothermal / solvothermal methods, chemical precipitation, self-assembly, surfactant-assisted methods, emulsion and microemulsion methods, thermal decomposition, sol-gel methods, and many more. The following sub-sections describe three common bottom-up techniques which can be used to produce ceria-based NPs.

#### 1.2.1.1. Hydrothermal / Solvothermal Method

The synthesis of NPs utilizing elevated temperatures and pressures is referred to as a hydrothermal synthetic route. More specifically, hydrothermal processing can be defined as any reaction that is performed under high temperature (> 100°C) and pressure conditions to facilitate the dissolution and recrystallization of materials in an aqueous system.[25] These conditions enable materials which are insoluble under standard conditions to undergo chemical reaction. Some researchers have further specified that hydrothermal conditions encompass any reaction that is taking place above room temperature and at a pressure greater than 1 atm, in a closed system.[25] Generally, the term solvothermal refers to any chemical reaction under high temperature and pressure conditions that is performed in the presence of a non-aqueous solvent or a solvent in supercritical conditions.[25] That being said, the terms hydrothermal and solvothermal are usually used interchangeably in the literature.

When the hydrothermal method is used to synthesize metal oxide NPs, the process is divided into three categories: hydrothermal synthesis, oxidation, and crystallization.[26] Hydrothermal synthesis is performed when synthesizing mixed metal oxides from their oxide or hydroxide metal precursors to yield well dispersed, uniform micro- to nano-sized particles.[26] By changing the reaction temperature and precursor concentration, the size and morphology of the obtained particles can be altered, along with the internal pressure of the reaction vessel. The oxidation method involves the direct oxidation of metals and alloys into oxide particles using solvents at high temperatures and pressures.[26] Finally, the most common hydrothermal technique used to prepare ceria-based NPs is the crystallization method. Typically, this process involves the precipitation of cerium salt solutions which are then treated at elevated temperature (and pressure) in sealed reaction vessels for several hours.[26] During this time, metal (hydro-) oxides are formed due to the shift in the reaction equilibrium.[27] Under sufficiently high temperatures, the equilibrium shifts further towards the formation of metal oxides to form the desired product.[27] The product is then washed and dried until a powdered product is achieved. The size and morphology of the particles formed depend on the reaction temperature, pressure, as well as the precursors used. It has been reported that smaller particles can be obtained through the use of lower temperatures and tetravalent cerium salt precursors.[26] The particle shapes and sizes can also be controlled through the addition of surfactants or stabilizers into the system. Figure 1.3a

depicts a typical synthetic strategy used to synthesize metal oxide NPs through the use of organic stabilizing agents.[28] A hydrothermal crystallization method is employed in this thesis to generate monodisperse ceria nanocubes with oleic acid stabilizers.[18] The sealed, high temperature pressure vessel in which the crystallization reaction is performed is shown in Figure 1.3b.

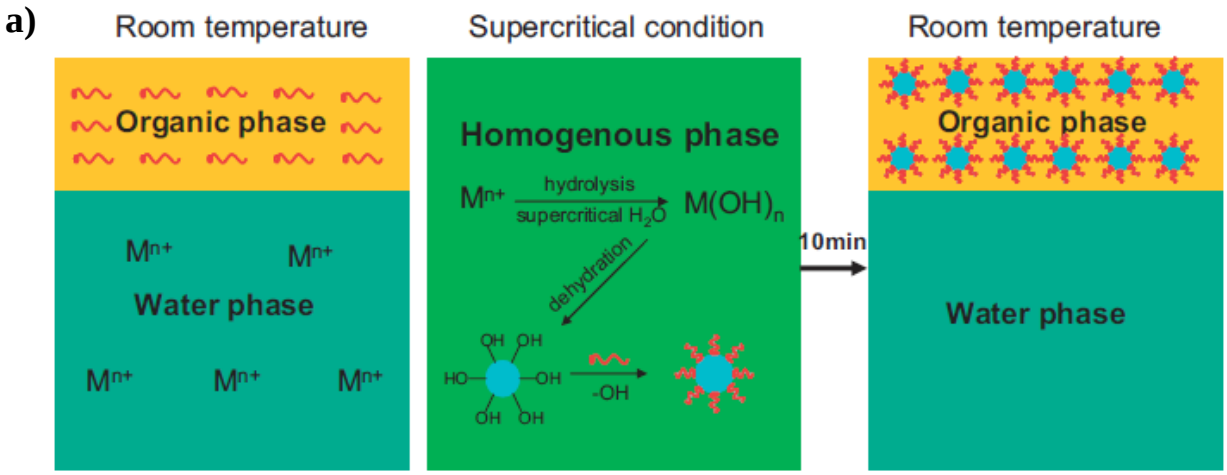


**Figure 1.3: a)** The strategy for the synthesis of metal oxide NPs by the organic-ligand-assisted supercritical hydrothermal process[28] [Reprinted with permission of Wiley-VCH from J. Zhang; S. Ohara; M. Umetsu; T. Naka; Y. Hatakeyama; T. Adschiri. *Adv. Mater.*, **2007**, 19, 203–206]; **b)** Stainless steel 23 mL acid digestion vessel and Teflon liner (Parr Instrument Company) used during this work.

### 1.2.1.2. Thermal Decomposition Method

Thermal decomposition of water soluble cerium salt precursors is another common technique employed to obtain high quality ceria NPs. The method is based on the chemical decomposition of the starting precursors through high temperature treatment. In a typical reaction mixture, the trivalent cerium salts, surfactants and high boiling point organic solvents are heated under reflux conditions for a specified reaction time.[20] Surfactants are added into the reaction mixture to protect the NPs from agglomeration and ensure that a narrow particle size distribution is achieved. Metal-carboxylate type precursors, *e.g.* metal-acetates, are preferred for this type of synthesis as they can generally be activated for decomposition by long chain amines or alcohols through the electron-deficient carbonyl group.[20] There are many factors, however, which can affect the final products of the reaction, therefore affecting the overall morphological control of the reaction. The reaction times and temperatures, as well as the addition of various long chain ligands and surfactants can affect the final obtained product.[20] Through the optimization of these parameters, various NP shapes and sizes can be synthesized, *e.g.* nanorods and nanoplates.[20]

### 1.2.1.3. Sol-gel Method

The sol-gel method is a wet chemical process which can be used to synthesize fine powdered materials having a variety of shapes and sizes.[26,29] There are three different types of sol-gel processes; colloidal or physical gel routes, inorganic polymeric gel routes, and organic polymeric gel routes.[29] All three syntheses contain multi-step processes that involve the conversion of a metal precursor solution (‘sol’) into a ‘gel’ and successively, with heating, into the desired oxide product.[29] The term ‘sol’ refers to a stable colloidal suspension of small particles.[26] The particles are suspended / dispersed in solution and electrostatic repulsion prevents aggregation. In the colloidal sol-gel system, the gelation step is governed by electrostatic or steric interactions between the suspended particles in solution.[29] In other sols, namely in the inorganic and organic gelation routes, the particles interact with each other to form a continuous integrated network of particles or clusters, called a gel.[26] This porous gel is then dried to form the final metal oxide product. Conventional drying, *i.e.* by solvent evaporation,

collapses the pore structure due to the surface tension while the capillary forces cause the gel to shrink and crack.[26] The resulting dried gel is referred to as a xerogel. If the wet gel is dried under supercritical conditions or through extraction of the solvent, the pore and network structure is maintained, and is referred to as an aerogel.[26]

The most common sol-gel method for the synthesis of ceria-based materials is the inorganic gel route. In this method, the sol is produced from the hydrolysis of a reactive metal complex through the addition of water. A metal alkoxide having the general formula $M(OR)_n$, where M is a metal and R is an alkyl group, *e.g.* $Ce(OCH(CH_3)_2)_4$ is dissolved in an alcohol to facilitate the reaction. The overall reaction can be represented as follows:

$$Ce(OCH(CH_3)_2)_4 + 4\ H_2O \rightarrow CeO_2 + 4\ ((CH_3)_2CH)OH \qquad (1.2)$$

The extent of the hydrolysis can be controlled by altering the ratio of water to metal alkoxide in the system. Following hydrolysis, a series of condensation reactions occur between the hydroxide groups through olation (and oxolation) polymeric processes.[26]

## 1.2.2. Controlled Synthesis

As briefly discussed in the previous sections, the controlled synthesis of ceria NPs having defined shapes and sizes has been of significant interest. The ability to control the morphology of the NPs allows for effective tuning of their properties as different shapes have different exposed surface structures and reactive planes. The formation of such nanostructures is defined by two essential processes: nucleation and growth. The successful control of the nucleation and growth rates can determine the final shape and size of the NPs.

Nucleation is the initial process in NP formation, *i.e.* when small nuclei are formed.[30] There are two types of nucleation processes: homogeneous and heterogeneous nucleation. Heterogeneous nucleation occurs much more readily than the homogeneous process as it requires less energy.[30] The heterogeneous nucleation process occurs at preferential sites (nucleation sites), such as phase boundaries and impurities, due to the fact that the surface energy at these sites is much lower than in the bulk of the solution.[30] This lowers the free energy barrier and promotes nucleation. The homogeneous process, on the other hand, occurs in the interior of a uniform

solution / medium.[30] This type of nucleation occurs much more randomly and with more difficulty as the spontaneous creation of nuclei consumes energy.[30] This spontaneous nucleation usually requires either super-heating or super-cooling of the reaction medium in order to proceed.[30] After the initial nucleation process, the growth of the nuclei occurs very rapidly and spreads outwards from the nucleation site. This growth will continue until the system reaches a state of equilibrium.

Both the nucleation and growth rates can be controlled to achieve a variety of different particle shapes and sizes. Generally, larger particles are derived at low nucleation rates while smaller particles are formed at high nucleation rates. This is due to the amount of initial nuclei that are formed and the subsequent growth processes.[30] In order to achieve monodisperse particles, the nucleation event must be separate from the particle growth, while shape control can be attained through the preferential growth of specific surface planes.[30] It has been reported that ceria nanocubes (NCs),[18] nanorods (NRs),[31] nanoplates,[32] nanowires,[33] nanotubes,[34] nanospheres,[35] nanoflowers,[35] and many more nanostructures, can be synthesized through controlled growth mechanisms.[30,36,37] Several of these mechanisms will be discussed in the following sub-sections, with the focus on the controlled synthesis of ceria NCs.

### 1.2.2.1. Oriented Growth

A common growth mechanism that is employed in the synthesis of ceria nanostructures is the oriented growth of the initially formed nuclei. This type of growth can be separated into two main categories: oriented growth directed by the crystallographic structure, and oriented growth directed by capping agents. Both methods allow for the morphological control of the synthesized nanostructures.

In the first method, the utilization of hydrothermal and precipitation reactions is quite common. Both of these treatments allow for the growth of small nanocrystals in the presence of an organic solvent. Section 1.2.1.1 described the detailed synthetic procedure involved in hydrothermal synthesis. Generally, the particles that are obtained through this synthetic method have defined faces, *i.e.* NCs, NRs, and nanooctahedra.[18,31,38] Previously, it has been shown that certain crystallographic surface planes of ceria are more stable than others.[39] Theoretical and experimental results have determined that the (111) surface of ceria is the most stable, followed

by the (110) and (001) surfaces.[39] It has been reported that the anions associated with the cerium salt precursors (*e.g.* $Cl^-$, $NO_3^-$, $SO_4^{2-}$, and $PO_4^{3-}$) have a large influence on the final morphology of the NPs.[30] The anions selectively interact with different surface planes, leading to various morphologies. For example, the hydrothermal synthesis of ceria NPs was performed in the presence of cerium (III) chloride and cerium (III) nitrate, and different morphologies were obtained.[40] In the presence of the $Cl^-$ anion, ceria NRs were obtained, while in the presence of the $NO_3^-$ anion, ceria NCs were obtained as the final product.[40] It was postulated that the $NO_3^-$ ions initially act as an oxidant and then selectively adsorb onto the (001) surfaces of the originally formed $Ce(OH)_3$ NRs.[40] This lead to the anisotropic growth of the (110) planes forming ceria NCs enclosed by six (001) planes.[40] The proposed growth mechanisms in the presence of both the $Cl^-$ and $NO_3^-$ anions are illustrated in Figure 1.4.[40] Although this method can produce nanomaterials which have high crystallinity, the particle size distributions can be quite poor. In order to improve these obtained size distributions, capping agents can be employed.

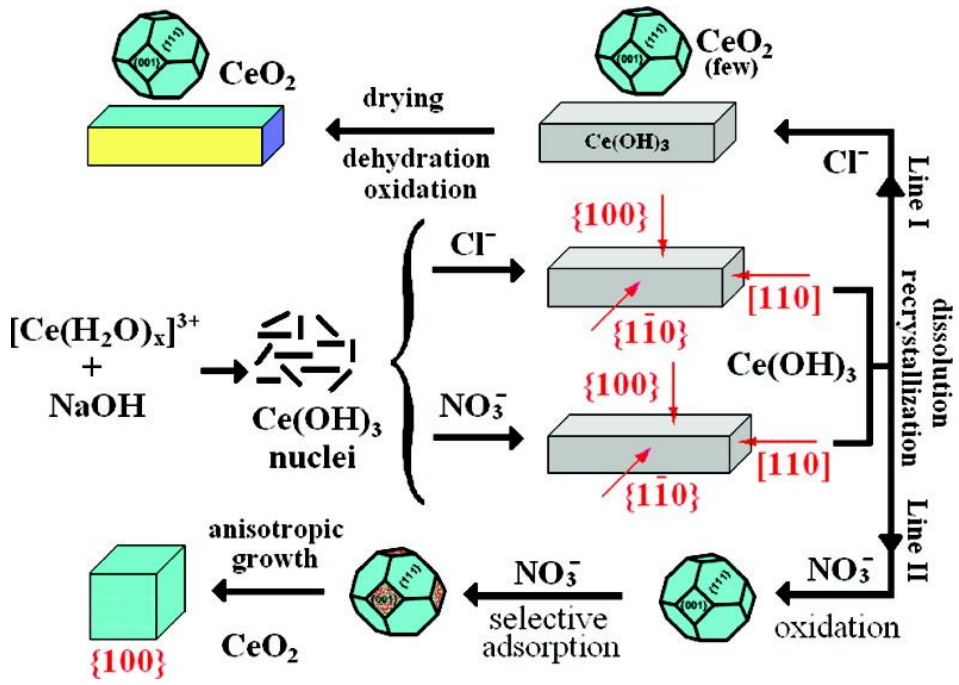


**Figure 1.4:** Schematic illustration for the conversion from nanorods to nanocubes.[40] [Reprinted with permission from Q. Wu; F. Zhang; P. Xiao; H.S. Tao; X.Z. Wang; Z. Hu; Y.N. Lu. *J. Phys. Chem. C*. **2008**, 112, 17076–17080. Copyright 2008 American Chemical Society]

The use of capping agents in NP synthesis has become very common in the literature. This method utilizes organic surfactants which can selectively adsorb onto specific surface planes of the particles and direct their growth. Common surfactants include cetyltrimethylammonium bromide (CTAB; $(C_{16}H_{33})N(CH_3)_3Br$), oleic acid (OLA; $CH_3(CH_2)_7CH=CH(CH_2)_7COOH$), oleylamine ($CH_3(CH_2)_7CH=CH(CH_2)_8NH_2$), and octadecylamine ($CH_3(CH_2)_{17}NH_2$).[30,18,20] This type of synthesis has the advantage of yielding small, monodisperse NPs having well defined surface planes. The use of surfactants aids in stabilizing the obtained NPs by tightly adsorbing onto the NP surface. This action protects the NPs from agglomeration due to the steric bulkiness of the adsorbed organic ligands. This also slows the growth rate, which promotes smaller particle formation. Yang *et al.* utilized a modified version of this procedure, known as the oriented aggregation mediated precursor growth method, to synthesize monodisperse ceria NCs.[18] This procedure is applied in this thesis and is further discussed in the following sub-section.

#### 1.2.2.1.1. Ceria Nanocubes

Yang *et al.* reported the hydrothermal synthesis of large ceria NCs (8 – 20 nm) using aqueous cerium (III) nitrate solutions, toluene, OLA (as surfactant) and *tert*-butylamine.[18] This oriented aggregation mediated precursor growth mechanism consists of three processes: nucleation, aggregation (with the removal of the surfactant molecules), and growth (from molecular precursors).[18,30] The large NCs are thought to have grown and assembled through the oriented attachment of two or more NPs.[18,41] The OLA surfactant molecules preferentially adsorb onto the (002) surface planes of the ceria NPs, which promotes the faster growth on the (111) planes.[18] This results in ceria NCs which are terminated with six (002) planes. The method in which the NCs self-assemble is dependent on the nature of the particles, the media in which they are dispersed, as well as the size of the particles.[42] For NPs which are smaller than 10 nm, van der Waals forces are usually dominant, with self-assembly being driven by interactions on a molecular level.[42] Due to the strong dipole-dipole interactions between the polar (002) surfaces, it was postulated that this was a driving force for the self-assembly of the ceria NCs into 3D arrays, separated by the OLA tails.[18] The size of the NCs was tuned through the OLA to Ce (III) molar ratio. With increasing molar ratio, the size of the NCs also increased.[18] In some cases, a

bimodal size distribution was observed, indicating that some of the NCs were grown as a result of Ostwald ripening, where larger particles grow at the expense of smaller ones.[18,41] This also indicated that the oriented attachment and Ostwald ripening growth modes were uncontrolled during the reaction.[41] Tuning these growth modes is difficult yet possible, as demonstrated by Taniguchi *et al.* in their examination of hydrothermally synthesized ceria NCs.[41] It was shown that the surface valence of the Ce cations played a critical role in promoting (or suppressing) the rate of the oriented attachment growth mode in the NCs.[41]

### 1.2.2.2. Template-Directed Growth

Ceria nanomaterials can also be prepared through the use of template-directed (or assisted) methods. This growth method can be used to prepare hollow ceria nano-structures, *e.g.* nanospheres and nanotubes.[30] Similarly with the oriented growth mechanism, there are a few different types of template synthesis; self-template synthesis, soft template-directed synthesis, and hard template-directed synthesis.[30] In the self-template synthetic process, an initially formed nanocrystal is used as a 'template' for the remainder of the reaction, confining the growth of the subsequent nanocrystals.[30] Soft template-directed synthesis uses a surfactant to control / direct the growth of the NPs, in a similar fashion to the oriented surfactant-assisted method discussed in the previous section. Lastly, the hard template-directed method is the most commonly used method to synthesize hollow nanostructures. Conventional hard templates include carbon nano-tubes, porous anodic alumina membranes, and silica spheres.[30] As an example, the successful coating of carbon nanotubes with ceria NPs is a key step to produce ceria nanotubes.[30] This method, although the most common, is also the most complex as there are two main steps involved; the mixture of the cerium precursor and the templates, then the removal of the templates to form the desired hollow ceria nanostructures, which is extremely difficult.[30] That being said, the obtained nanomaterials generally have uniform sizes which can be easily controlled. Due to the fact that these materials are usually hollow in nature, they offer an increased surface area which could be beneficial for catalytic applications.

There are numerous additional methods which can be employed to obtain the controlled synthesis of ceria nanomaterials. A few examples include electrochemical deposition, microwave

assisted synthesis, ultrasonic irradiation, and chemical vapour deposition.[30] However, these methods will not be discussed here.

## 1.3. Catalysis

The field of catalysis is an ever-growing and important area of research. Today, it is estimated that 85 – 90 % of the products made in the chemical industry are produced through some sort of catalytic process.[43] A catalyst can offer an energetically favourable mechanism allowing large scale industrial processes to be run under milder conditions than the non-catalytic reaction. A catalyst, in general terms, accelerates the rate of a chemical reaction. In doing so, the catalyst favourably interacts with the reactant molecules to promote the faster and more efficient formation of the final products.[43] The catalyst is however not consumed during the reaction, but is regenerated at the end. This process, no matter how complex, is referred to as a catalytic cycle.

Catalysts can come in a variety of forms (*e.g.* from small molecules to enzymes), and can be employed under various reaction conditions. These catalysts can be separated into two distinct classes: homogeneous catalysis and heterogeneous catalysis. The catalytic mechanisms in both cases are extremely different and therefore offer a wide range of opportunities to create diverse catalysts and catalytic systems for numerous applications. In homogeneous catalysis, both the catalyst and the reactants are in the same phase. Usually, the species are dissolved in the same solvent mixture; examples include organometallic catalysts (*e.g.* Grubb's catalyst), biocatalysts (*e.g.* enzymes and lipases) and NP catalysts (*e.g.* Au or Pd NPs). NP catalysis is sometimes considered to be a pseudo-homogeneous catalytic reaction as the solid NPs are typically not completely dissolved in the solvent, but rather suspended in the solution. Alternatively, in heterogeneous catalysis, the catalyst exists in an entirely different phase / state than the reactants. Generally, the catalyst is a solid and is used to catalyze reactions of gas- or liquid-phase molecules. The catalysis occurs at the surface of the solid particles at the catalytically 'active' sites. This thesis focuses on the use of Au and ceria-based materials as heterogeneous catalysts towards alcohol oxidation reactions.

### 1.3.1. Oxidation Reactions

Generally, the catalysis of oxidation reactions using a combination of molecular oxygen and heterogeneous catalytic systems have been shown to be extremely useful and important processes in the chemical industry; for example, in the production of fine chemicals and important precursor chemicals in the fragrance and pharmaceutical industries.[44] Typically, these oxidation reactions use stoichiometric amounts of inorganic oxidants, organic solvents, and produce large amounts of hazardous waste, which makes them both environmentally and economically undesirable. Although homogeneous oxidation catalysts that can use $O_2$ (g) as the oxidant can produce high yields, they tend to be quite difficult to separate from the reaction mixture, leading to the increasing interest in the development of new heterogeneous catalysts.[44] Ceria-based heterogeneous catalysts have been shown to be suitable catalytic systems for many different oxidation reactions, such as alcohol and CO oxidation reactions.[45]

### 1.3.2. Ceria-Based Catalytic Systems

Ceria-containing catalysts have been extensively studied over the past several decades with the main interest focusing on heterogeneous catalytic systems.[45] In such systems, ceria itself can act as the catalyst or can be used as a support system to increase the activity of the supported catalytically active compounds. Ceria has also been shown to affect different catalytic systems through secondary processes. For example, it has been known to affect the dispersion of supported metal NPs; store and release oxygen, hydrogen and sulfur; and form surface and bulk vacancies.[45] The exceptional redox properties of ceria, which are believed to be both size and shape dependent, are the main reason for its use in a variety of different systems.[45,46]

The relative catalytic activity of the three main ceria surface planes [(111), (001) and (110)] has been previously studied.[46,47] This was done to investigate if certain crystallographic surface planes are more reactive than others.[46,47] Using a powerful catalytic probe (the oxidation of CO), it was found that the more reactive (001) and (110) surfaces showed an increased activity for CO oxidation than the less reactive (111) surfaces.[46] The aforementioned study focused on altering the particle morphology in order to obtain the desired exposed surface planes for catalysis.[46] In doing so, the results demonstrated that ceria nanowires, which exhibited

exposed (110) and (001) planes, presented a higher catalytic activity for CO oxidation than ceria NRs, which also contained exposed (110) and (001) planes, and ceria NPs, which had exposed (111) planes.[46] The higher catalytic activity observed from the larger / longer ceria nanowires resulted from having a larger proportion of exposed reactive planes than the NRs.[46] In a similar study, the OSC of various ceria nanostructures was investigated.[38] It was found that large ceria NCs (~ 36 nm) having only exposed (001) surfaces exhibited the highest OSC as compared to NRs (enclosed by four (110) and two (001) planes) and nanopolyhedra (enclosed by eight (111) and six (001) planes).[38] With this in mind, the previously described hydrothermally synthesized ceria NCs having exposed (002) surfaces (Section 1.2.2.1.1) have the potential to be highly active towards catalysis.[18]

Even though ceria shows a high activity towards CO oxidation reactions, the activity can be significantly increased through the interaction with metal NPs, particularly Au NPs.[48] There are many reasons why the use of Au NPs have become almost common place in the catalytic literature. Originally, Au was thought to be catalytically inert, however it has been shown that its catalytic activity is directly related to the size of the Au species.[49] Since the influential work by Haruta *et al.*, CO oxidation catalyzed by metal oxide supported Au NPs has been extensively studied.[48] It has been elucidated that the major role of the support is to reduce the mobility of the Au NPs and therefore diminish their ability to agglomerate / sinter during the catalytic reactions.[48,49] The use of ceria as a support has attracted much attention in the scientific community due to its aforementioned redox capabilities. When used as a support, ceria can actively participate in the catalytic reaction which increases the overall activity of the reaction.[49] Au supported on ceria ($Au/CeO_2$) has been shown to be a catalyst for many important reactions, including CO oxidation,[48,49] alcohol oxidations,[50,51] hydrogenations,[52] and the water-gas shift reaction.[53]

Typically, supported catalysts are prepared using an impregnation method. The most commonly used method is known as the incipient wetness impregnation method. This method focuses on depositing ultrafine metal NPs onto a high surface area support.[26] The active catalyst is dispersed in an aqueous or organic solution and is then 'impregnated' into the pores of the support material.[26] To achieve optimal impregnation, the solution containing the catalytic metal must be of the same volume as the volume of pores within the support. Capillary action draws

the solution into the pores and the metal species adsorb onto the basic support sites ($O^{2-}$ or $OH^-$).[26] Subsequent drying and calcination adheres the particles to the support. This method is a fast and efficient way of dispersing small amounts of NPs onto the surface of a support. For example, Abad *et al.* utilized a Au salt precursor solution and a given amount of $CeO_2$ under basic conditions to prepare well defined $Au/CeO_2$ composites which were catalytically active towards the selective oxidation of primary and secondary alcohols.[51] This synthetic procedure was adapted and employed in this thesis.

The origin of the catalytic activity of $Au/CeO_2$ composites has been of much debate in the literature, as some researchers have suggested that the activity could be related to 'active' sites located at the Au-support interface; possible charge transfer from the support to the Au; or effects related to the exposed crystallographic surface planes of the support.[54] It has been shown, however, that with ceria-supported catalysts, the activity and selectivity of the catalyst is dramatically increased in the presence of strong metal-support interactions, which depend on the exposed surface planes of the ceria support.[54] The influence of different exposed ceria surface planes on the activity of the Au NPs has been previously investigated.[55] Surprisingly, it has been found that Au NPs (2 – 8 nm) supported on the (110) planes of ceria NRs showed a higher activity towards the water-gas shift and CO oxidation reactions than those supported on the (001) planes of ceria NCs.[55] These unexpected findings could be the result of the catalytic preparation methods. It could also be a result of the presence (or absence) of cationic Au species ($Au^{\delta+}$), as it has been reported that the catalytic activity in CO oxidation reactions involving Au depends on the presence of both cationic and reduced Au species during the reaction.[55] To explore this, Guan *et al.* studied the Au $L_3$-edge XANES spectra of the aforementioned $Au/CeO_2$ NR and $Au/CeO_2$ NC catalysts.[55] It was elucidated from the spectra that the Au NPs supported on ceria NRs were cationic in nature, while the Au NPs supported on the ceria NCs were primarily $Au^0$, and therefore showed a lower activity for CO oxidation reactions.[55]

In order to better understand this mechanism, researchers have begun to explore catalytic systems containing well-defined, monodisperse ultra-small Au NPs. The use of these Au NPs (referred to as Au nanoclusters) ensures uniform Au deposition on the support, as this has previously been found to be a challenge in the literature.[56] With conventional Au NPs, the structure of the active site is difficult to investigate as the surface structure of the Au is

unknown.[56] However, the atomic structure of various Au monolayer protected clusters (MPCs) has been experimentally determined by X-ray crystallography and extended X-ray absorption fine structure (EXAFS) spectroscopy.[56-58] These atomically precise Au nanoclusters are generally protected by thiolate ligands, referred to as $Au_n(SR)_m$ MPCs, where n and m represent the number of Au atoms and thiolate ligands (SR) present, respectively.[56-58] The structure of a typical Au MPC, $Au_{25}(SR)_{18}$ (Figure 1.5) consists of a $Au_{13}$ icosahedral core which is surrounded by Au-thiolate staples.[56-58]

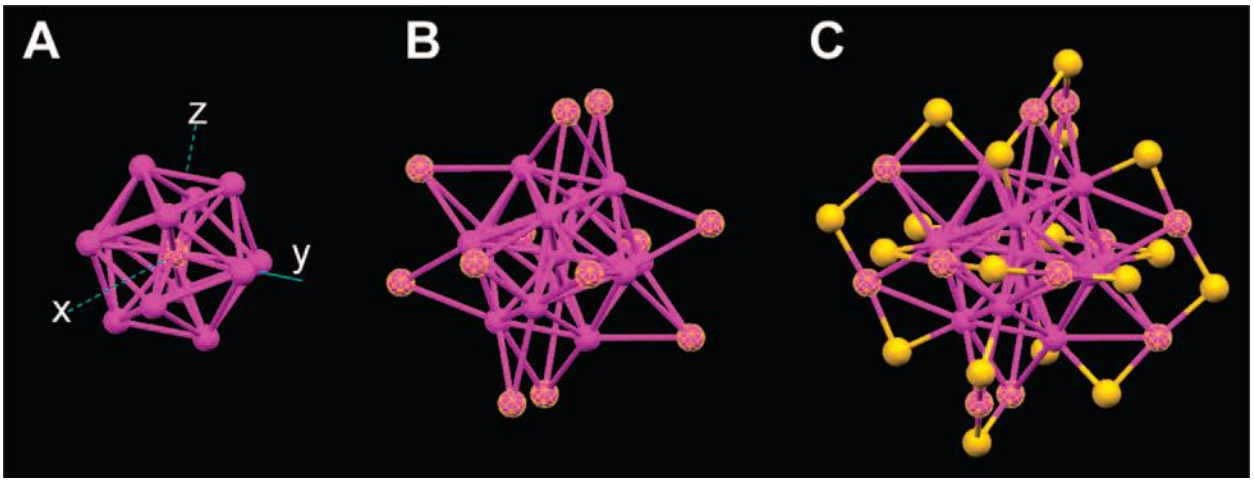


**Figure 1.5:** Crystal structure of **a)** $Au_{13}$ core; **b)** $Au_{13}$ core with exterior 12 Au atoms; **c)** $Au_{25}(SR)_{18}$ MPC (Au atoms are in purple; S atoms are in yellow; C atoms omitted for clarity).[58] [Reprinted with permission from M. Zhu; C.M. Aikens; F.J. Hollander; G.C. Schatz; R. Jin. *J. Am. Chem. Soc.*, **2008**, 130, 5883–5885. Copyright 2008 American Chemical Society.]

Recently, the $Au_{25}(SR)_{18}/CeO_2$ system has been studied and was found to exhibit a high activity for CO oxidation, especially after $O_2$ pre-treatment at moderate temperatures.[56] This reaction was preformed utilizing powdered / bulk ceria as the support system.[56] In this thesis, the activity of a variety of $Au_{25}(SR)_{18}/CeO_2$ catalysts are investigated through the oxidation of benzyl alcohol to test the versatility of such systems.

## 1.4. Characterization Techniques

In order to successfully probe the various properties of ceria-based materials, a variety of characterization techniques need to be used. This section discusses the key techniques that are used throughout this thesis for morphological and electronic structure characterization: transmission electron microscopy (TEM), X-ray photoelectron spectroscopy (XPS) and X-ray absorption near-edge spectroscopy (XANES).

### 1.4.1. Transmission Electron Microscopy

TEM is an invaluable technique used to characterize both the size and shape of synthesized nanomaterials. In this technique, a beam of high energy electrons (usually in the range of ~ 60 – 200 kV) is focused onto a thin sample specimen; the electrons irradiate and penetrate the sample, and are imaged by various lenses.[59,60] In typical TEM set-ups, samples can be magnified and imaged with a magnification in the range of $10^3$ to $10^6$ times their original size, allowing nanosized particles to be visualized. The TEM image is produced through the scattering of the incident electron beam by the atoms in the sample under investigation. The electron-optical system employed in TEM instruments can be divided into three main sections; the illumination system, the specimen stage, and the imaging system.[59] The electron gun that is used to produce the beam of electrons, along with several condenser lenses which focus the electrons onto the sample, are located in the illumination system.[59] The diameter as well as the intensity of the electron beam can be tuned through this system. The aptly named specimen stage is where the sample specimen is placed during imaging and holds the sample in a stationary position.[59] The sample under analysis is placed or drop-coated onto a carbon-coated copper grid which fits into the specimen stage. Finally, the imaging system is comprised of multiple lenses that are used together to produce a magnified image of the sample.[59] The image is then recorded on photographic film, a fluorescent screen, or a digital camera system depending on the TEM instrument. The TEM instrument used for NP characterization throughout this thesis utilizes a plate film camera for image acquisition, has a resolution of *ca.* 0.5 nm, and is depicted in Figure 1.6.

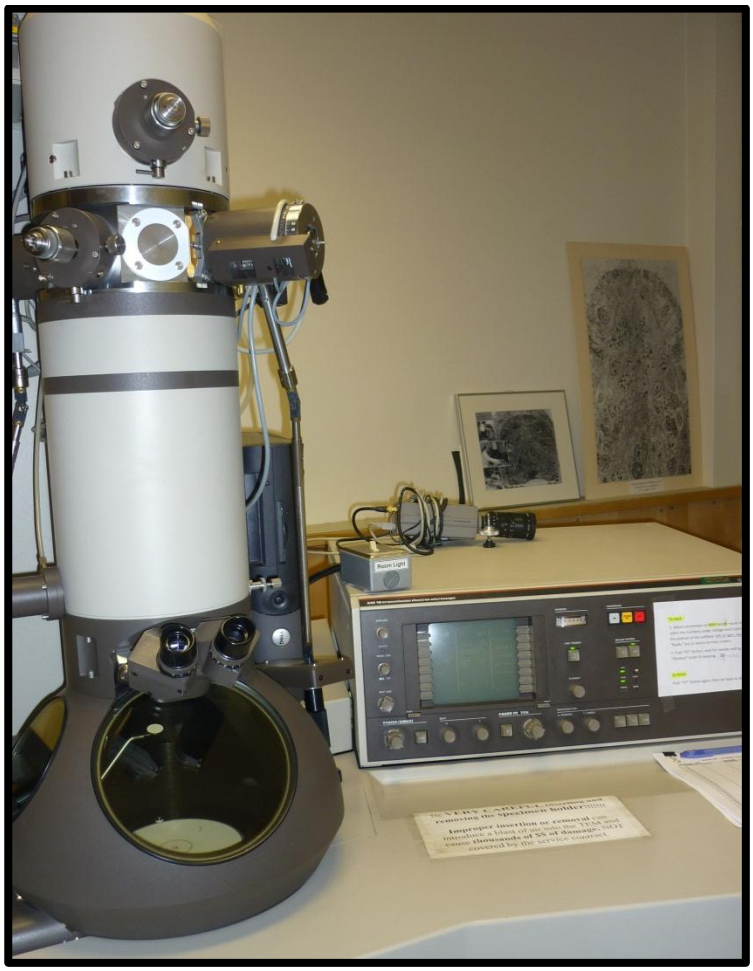

**Figure 1.6:** TEM instrument used throughout this thesis (Phillips CM10, located in the Biology Department, University of Saskatchewan).

There are two imaging techniques which are commonly used for NP characterization, bright field (BF) and dark field (DF) imaging modes.[59,61] These modes rely on how the incident electron beam interacts with the sample, as well as the position of the objective aperture in the back focal plane.[61] A BF image is formed when the aperture is positioned in such a way that only electrons which have been transmitted and not diffracted by the sample are allowed to pass.[61] The regions of the specimen grid which do not contain any sample, *i.e.* the background field (specimen grid), appear brighter than thicker regions which do contain sample. Typically, the specimen grid is carbon coated and appears very bright in comparison to the sample. The thickness of the sample, along with the atomic number (Z value) of the sample will affect how

bright or dark the image appears; the thicker the sample and the greater the electron density of the sample, the darker the image. Conversely, when the aperture is positioned to allow only some of the diffracted electrons to reach the imaging system, a DF image is produced.[61] When the incident electron beam comes into contact with the sample, the electrons experience Bragg scattering / diffraction. If the sample is crystalline, the electrons are diffracted onto the back focal plane which corresponds to the various crystallographic planes within the sample.[61] Optimization of the objective aperture allows for the selection of specific Bragg peaks which will appear in the image. The regions of the specimen grid which diffract these electrons, *i.e.* regions which contain high atomic weight elements, will appear as bright spots, while the regions which do not diffract electrons will remain dark. An example of bright and dark field images of $NbF_5$-doped $Ca(BH_4)_2$ prepared by Minella *et al*. is shown in Figure 1.7.[62] Both images show the same region of the specimen grid with opposing contrast. The DF image allows for the visualization of the bright Nb atoms which are doped throughout the $Ca(BH_4)_2$ matrix. The Nb atoms have a much higher Z value than the support matrix, allowing them to appear much brighter in comparison.

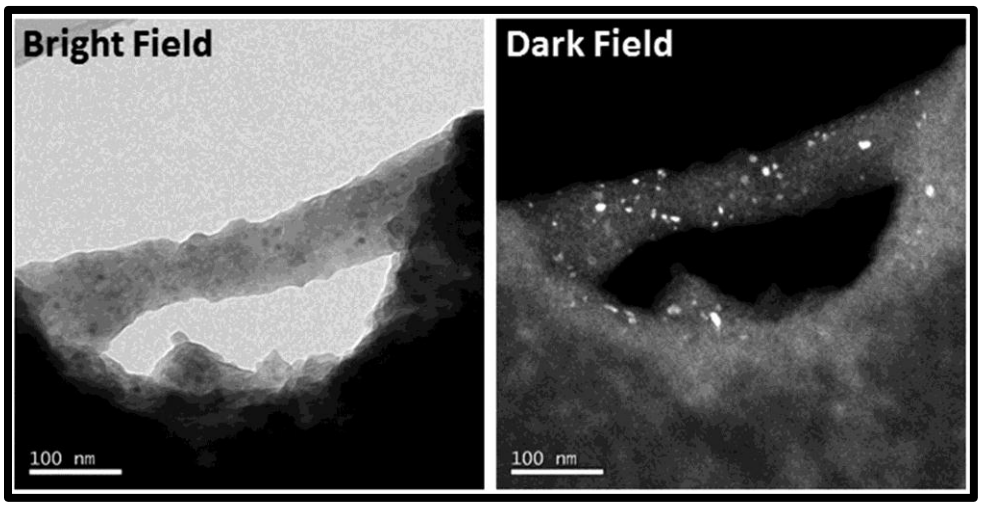


**Figure 1.7:** TEM images (bright and dark field) of a $Ca(BH_4)_2$ sample doped with $NbF_5$ fully desorbed at 450°C in vacuum.[62] [Reprinted with permission from C.B. Minella; E. Pellicer; E. Rossinyol; F. Karimi; C. Pistidda; S. Garroni; C. Milanese; P. Nolis; M.D. Baró; O. Gutfleisch et al. *J. Phys. Chem. C.* **2013**, 117, 4394-4403. Copyright 2013 American Chemical Society.]

As can be noted from Figure 1.7, both TEM imaging modes provide invaluable information about the size and morphology of the sample under investigation. The size of the particles can be measured through the use of imaging software (*e.g.* ImageJ).[63] Typically, when measuring NPs, a minimum of 100 particles is measured in order to determine an average particle size as well as the particle size distribution. This information is very important when dealing with catalytic systems that require monodisperse NP samples. TEM, however useful, only reveals structural information about the NPs in question. The use of spectrophotometric methods can allow for the investigation of the chemistry of the NPs.

## 1.4.2. X-ray Photoelectron Spectroscopy

X-ray techniques, such as XPS and XANES (to be discussed in Section 1.4.3), are extremely useful methods to investigate the presence of multiple oxidation states within a material. XPS is a characterization technique which utilizes the photoelectric effect. When a compound is irradiated with photons of sufficient energy, electrons are ejected as photoelectrons either from core or valence levels.[64] The kinetic energy (KE) of the ejected photoelectrons depends on the incident photon energy ($h\nu$) as well as the chemical environment within the material.[64] In a typical laboratory or synchrotron-based XPS set up, the emitted photoelectrons are ejected into vacuum and are analyzed by a hemispherical electron analyzer before reaching the detector. The electron analyzer ensures that only electrons of a given energy (pass energy) will reach the detector. Electrons having too high or too low of energy will come in contact with the walls of the analyzer, and will not reach the detector. The pass energy is typically varied between 5 and 200 eV; as the pass energy increases, the energy resolution deteriorates.[64] Prior to entering the electron analyzer, the emitted photoelectrons are slowed from their original energy, without altering their absolute energy, to achieve the necessary / improved energy resolution.[64] This process also aligns the KE of the photoelectrons with the defined pass energy of the analyzer. The detector then analyzes the incoming electrons and generates a plot of electron counts (intensity) as a function of the KE. As the binding energy (BE) of an electron is characteristic of the absorbing atom and an intrinsic property of the material, the presented spectra are typically converted from a KE to a BE scale through the following equation:

$$KE = h\nu - BE - \phi_s \quad (1.3)$$

where $\phi_s$ is the work function of the sample.[64] The work function is material-specific and denotes the minimum amount of energy required to eject an electron from the surface of a material into vacuum.[64,65] This value is typically difficult to determine, and is therefore eliminated from the equation by aligning the Fermi level energies ($E_F$) of the sample and the spectrometer by grounding the sample stage. The work function of the spectrometer ($\phi_{spec}$) is related to the $E_F$ and the vacuum level ($E_{vac}$) by the following equation, and can be substituted into eq. 1.3 to calculate the KE (or BE): [66]

$$\phi = \phi_{spec} + \phi_s \quad (1.4)$$

$$\text{Where } \phi_{spec} = E_F - E_{vac} \quad (1.5)$$

The relationship described in eq. 1.3 describes the elastic photoemission process that is occurring during experimentation; *i.e.* the emitted photoelectrons which have not suffered any energy loss as they travel through the solid material.[64] The inelastically scattered photoelectrons, *i.e.* those which have lost kinetic energy, give rise to the step-wise like background observed in XPS spectra. An example of this can be seen at higher BE in the XPS survey spectrum of bulk $CePO_4$ presented in Figure 1.8a which was collected as part of this thesis. Survey spectra are recorded over a wide energy range (≥ 1000 eV) using a large pass energy (100 – 200 eV) and a large step size (≥ 0.7 eV / step) to determine the overall elemental composition of the material under analysis. Using computer software programs like CasaXPS, the peaks in the spectrum can be assigned to their associated transitions.[67] To elucidate the finer chemical properties of the material, for example the oxidation states of the absorbing atoms, core-line spectra are recorded. These spectra are collected over a much narrower energy range using a lower pass energy (5 – 50 eV), and at a much smaller step size (≤ 0.1 eV / step) compared to survey spectra. Figure 1.8b presents the Ce 3d XPS core-line spectrum of bulk $CePO_4$. Using the CasaXPS software program, the background of this spectrum has also been removed / subtracted using a Shirley-type function, and the peaks have been fitted using synthetic (Gaussian / Lorentzian) components.[67,68] Removing the spectral background and fitting the spectrum allows for the in-depth analysis of the individual photoemission transitions. Further detail on the various Ce photoemission peaks are presented in Chapter 2.

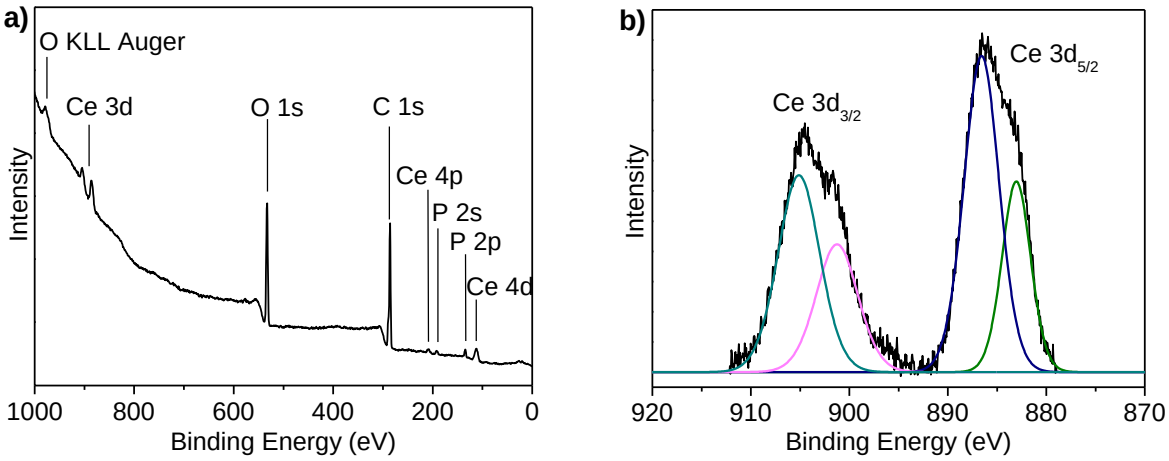


**Figure 1.8: a)** XPS survey spectrum (with labeled peak transitions), and **b)** background-subtracted and fitted Ce 3d XPS core-line spectrum of bulk $CePO_4$.

During the collection of XPS spectra, multiple transitions occur after the initial absorption of a photon by the absorbing atom. After the initial ejection of a photoelectron from a core level (Figure 1.9a), a core hole is produced. This core hole is extremely unstable and does not survive for very long. An electron from a higher, less tightly bound level can drop down (relax) to fill this core hole through a fluorescent process (Figure1.9b).[64] The core hole can also be filled through an Auger process (Figure 1.9c). This process involves the relaxation of an electron in a higher energy level, and coincides with the emission of an Auger electron.[64]

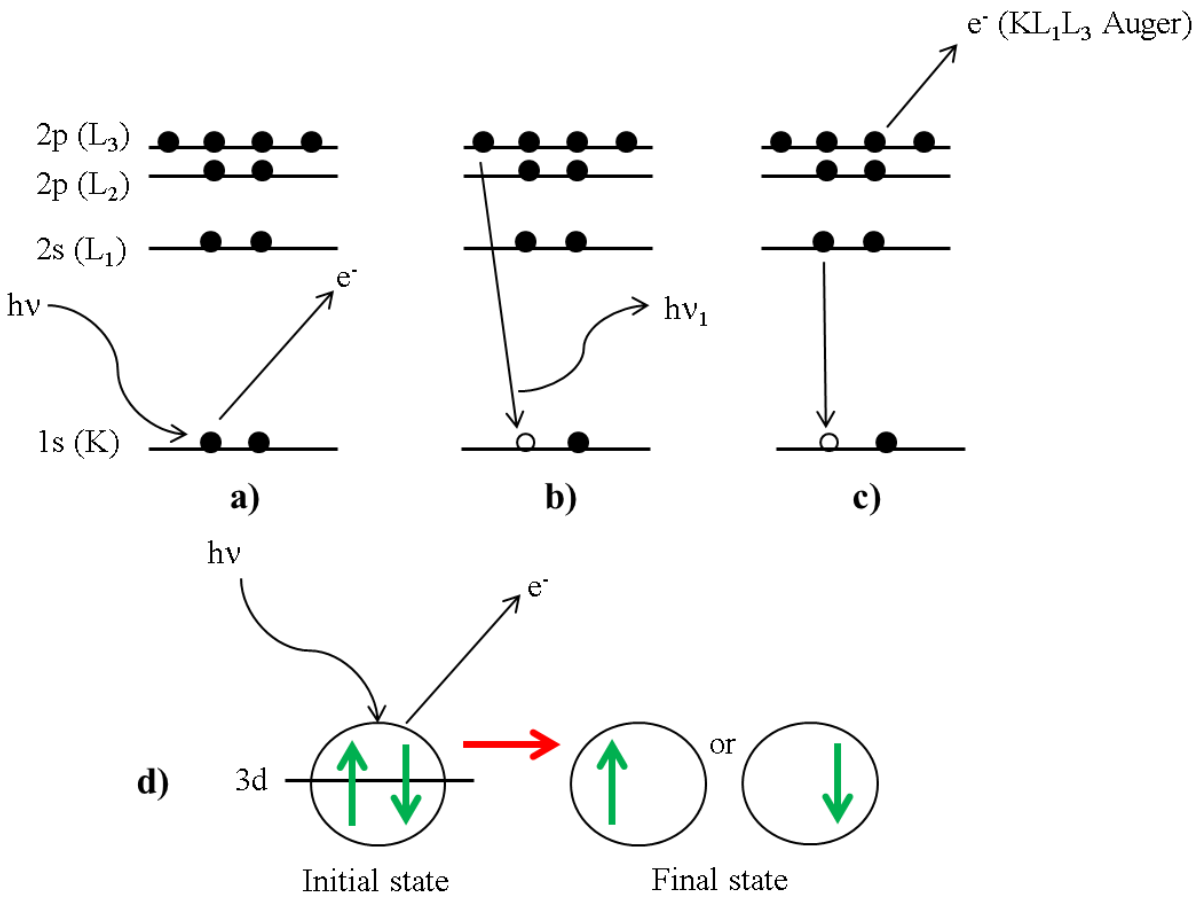


**Figure 1.9:** The various processes which occur after the initial absorption of a photon (hν) include **a)** emission of a photoelectron, **b)** relaxation and fluorescence ($h\nu_1$), and **c)** relaxation and emission of an Auger electron;[64] **d)** Emission of an electron from the 3d orbital and the two possible final states (spin up or spin down).[65]

Both the ejected photoelectrons and Auger electrons can be detected and analyzed by the hemispherical electron analyzer used in XPS experiments. As an example, in the survey spectrum of bulk $CePO_4$ (Figure 1.8a), the signals from the photoelectrons are labeled as the core-lines (Ce 3d, O 1s, C 1s, P 2p, and Ce 4d) and the Auger emissions are labeled using X-ray notation (O KLL). This notation, which is summarized in Table 1.1, denotes the three levels which are involved in the Auger emission process.[65] Initially, a photoelectron is ejected from a core level (K), producing a core hole. This core hole is then filled by an electron from a higher energy level ($L_1$), which transfers energy to another electron from the same or higher energy

level ($L_3$), and is emitted. The core-lines, on the other hand, are labeled based on the final state configuration after the photoelectron has been ejected.

**Table 1.1:** Nomenclature of various XPS peaks; where n is the principle quantum number, $\ell$ is the angular (orbital) quantum number, and j = $\ell$ + s (where s is the spin the electron).[65]

| n | $\ell$ | j | X-ray Notation | XPS Notation |
|---|---|---|---|---|
| 1 | 0 | 1/2 | K | $1s_{1/2}$ |
| 2 | 0 | 1/2 | $L_1$ | $2s_{1/2}$ |
| 2 | 1 | 1/2 | $L_2$ | $2p_{1/2}$ |
| 2 | 1 | 3/2 | $L_3$ | $2p_{3/2}$ |
| 3 | 0 | 1/2 | $M_1$ | $3s_{1/2}$ |
| 3 | 1 | 1/2 | $M_2$ | $3p_{1/2}$ |
| 3 | 1 | 3/2 | $M_3$ | $3p_{3/2}$ |
| 3 | 2 | 3/2 | $M_4$ | $3d_{3/2}$ |
| 3 | 2 | 5/2 | $M_5$ | $3d_{5/2}$ |
| ⋮ | ⋮ | ⋮ | ⋮ | ⋮ |

In the example of bulk $CePO_4$, the Ce 3d core-lines arise from the emission of a photoelectron from the Ce 3d core level. Figure 1.9d illustrates the two energetically equivalent final states which are possible after photoemission; the 'spin up' state (s = + ½) or the 'spin down' state (s = – ½).[65,69] When labeling these transitions, the following convention is used: (absorbing atom) n · $\ell_j$. For the Ce 3d core-lines, peaks corresponding to the Ce $3d_{5/2}$ and $3d_{3/2}$ components are observed (*c.f.* Figure 1.8b; Table 1.1). This phenomenon is known as spin-orbit splitting / coupling and is observed when $\ell > 0$.[69] This is referred to as fine structure since the splitting energy between the sets of peaks is typically quite small. The splitting arises from the parallel or antiparallel coupling of the spin angular momentum of an electron with its orbital angular momentum.[65] The area ratio between the two spin-orbit split peaks is considered to be fixed, regardless of the sample. The peak area ratio is described by:

$$(2j_1 + 1) / (2j_2 + 1), \quad (1.6)$$

where $j_1$ refers to the momentum of the unpaired 'spin up' core electron, and $j_2$ refers to the unpaired 'spin down' core electron. Utilizing the same example as above, bulk $CePO_4$, the Ce $3d_{5/2}$ / Ce $3d_{3/2}$ area ratio is calculated to be 3/2. As previously mentioned, the various Ce photoemission peaks are further discussed in Chapter 2.

Typically, when performing XPS experiments, tuning the sensitivity of the measurement is quite important as probing various depths within a sample can result in vastly different spectra, especially in the case of NP samples. Although the incident X-rays usually have a large attenuation length, typically on the order of microns, XPS experiments are inherently surface sensitive as only photoelectrons which are generated near the surface of the material have enough KE to escape the solid sample and be detected.[64] The X-ray attenuation length is defined as the X-ray penetration depth into a material, along the surface normal, where the intensity of the X-rays drops off to 1/e from its surface intensity.[70] The sampling depth of XPS however, describes the depth below the sample surface from which ~ 95 % of all photoelectrons emanate.[69] This is equivalent to ~ 3λ, where λ is defined as the distance an electron can travel through a solid before losing energy via inelastic electron scattering, *i.e.* the inelastic mean free path (IMFP) of the photoelectrons.[65,69] Being able to probe the surface of samples is quite important as the properties of the bulk material might be quite different. These differences can arise from surface adsorbates, defects in the crystallographic surface structure (*e.g.* oxygen vacancies), or a variety of other factors. As with most chemical reactions, the chemistry involved in NP catalytic systems occurs at the surface of the particles. This makes XPS an extremely useful characterization technique to study such systems.

### 1.4.3. X-ray Absorption Near-Edge Spectroscopy

X-ray absorption spectroscopy (XAS) is an extremely powerful technique used to study the elemental composition, chemical environment and oxidation states within a material. XAS is the measurement of the excitation of core level electrons of an absorbing atom into unoccupied conduction states or the continuum.[71] This excitation is prompted through the irradiation of the sample with a high intensity monochromatic X-ray beam, either using conventional or synchrotron-based X-ray sources. Nowadays, synchrotron-based techniques have become more common in the field due to the limitations of conventional X-ray tubes, including X-ray intensity and data collection time.[72] Synchrotron radiation has the advantage of providing tunable photon energies over a broad spectral range, *i.e.* both hard and soft X-rays, with a brightness on the order of $10^{19}$ photons / (s·mm$^2$·mrad$^2$·0.1% bandwidth).[72,73] The difference between hard and soft X-rays is the photon energy; soft X-rays have energies up to ~ 4 keV, while hard X-rays have energies which are greater than ~ 4 keV. To collect an XAS spectrum, the excitation energy is scanned through the absorption edge of the absorbing atom. The absorption edge occurs at a specific energy that is characteristic of the absorbing atom and appears as a sharp increase in the absorption cross section.[72] A typical XAS spectrum can be divided into two main regions; the XANES region, which extends out from the pre-edge (≥ 5 eV below the absorption edge) to ~ 50 eV above the edge, and the EXAFS (extended X-ray absorption fine structure) region which extends beyond ~ 50 eV above the absorption edge (see Figure 1.10).[71,72] The XANES region, which will be of main focus in this thesis, can provide detailed information about the oxidation state and coordination environment of the metal absorbing atom, while the EXAFS region can provide information on the radial distribution of atoms (*i.e.* the local bonding environment around the absorbing atom) from the analysis of the Fourier transform of the spectrum, in R space.[71,72] A typical XAS spectrum showing both the XANES and EXAFS regions is presented in Figure 1.10.

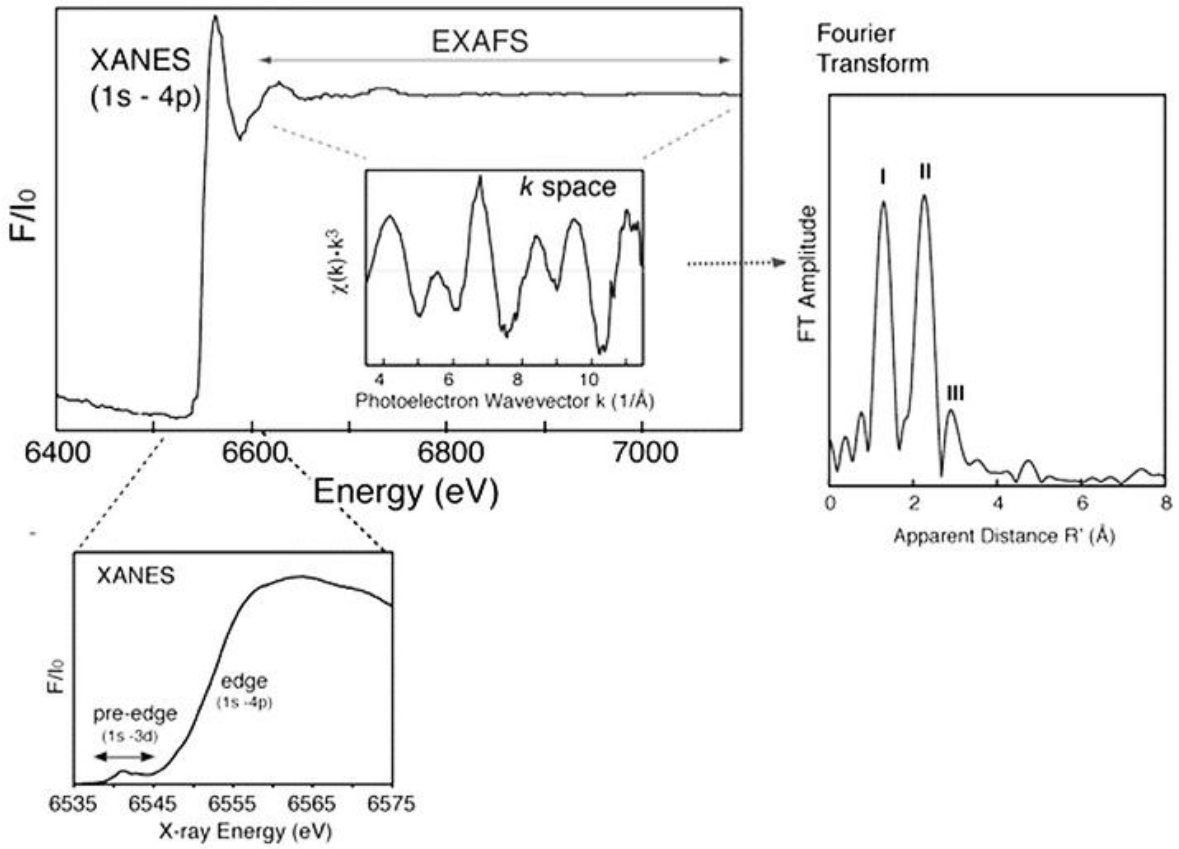


**Figure 1.10:** A typical Mn K-edge XAS spectrum showing the XANES and EXAFS regions. The enlargements show the Mn K-edge XANES and *k*-space EXAFS spectrum. The Fourier transform of the *k*-space EXAFS data is also shown.[71] [Reprinted with permission from J. Yano; V.K. Yachandra. *Photosynth. Res*. **2009**, 102, 241–254. Copyright 2009 Springer Science + Business Media.]

There are several different detection methods in which a XANES spectrum can be collected. In hard X-ray XANES measurements, transmission and fluorescence yield (FY) spectra are generally collected, while in soft X-ray XANES measurements, total electron yield (TEY) and FY are the most common detection methods. FY is typically measured as either the total fluorescence yield (TFY), which sums over the whole energy range, or as the partial fluorescence yield (PFY), which selectively detects the fluorescence from a narrower, selected energy range.[74] Since soft X-rays are too low in energy to fully penetrate the sample and interact strongly with matter, transmission measurements are not typically used.[75] The preferred

detection methods rely on the events which occur after the promotion of a core electron to an unoccupied conduction state. Figure 1.11 depicts a typical energy level diagram and shows the production of a core-hole after the excitation of core 1s, 2s and 2p electrons. Similarly with XPS experiments, there are several different pathways which can be followed after excitation; emission of photons (fluorescence – Figure 1.9b), direct emission of Auger or photoelectrons (Figure 1.9a, c), or indirect emission of secondary electrons through electron cascade events. As the names suggest, TFY/PFY measurements detect photons which are emitted by fluorescence, and TEY measurements detect the electrons (Auger, secondary and photoelectrons) which escape from the sample surface.

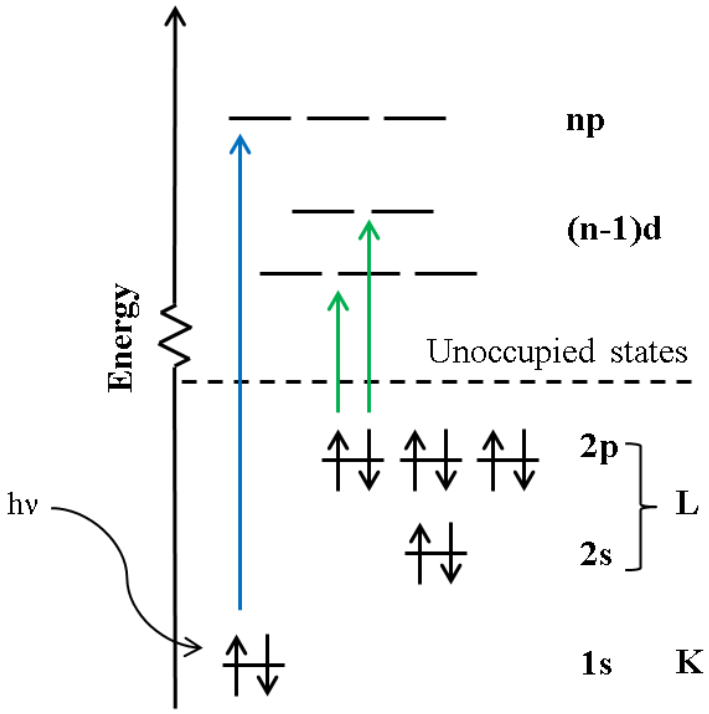


**Figure 1.11:** A typical energy level diagram showing K- and L-edge transitions (originating from the 1s and 2p orbitals, respectively) in XANES

The various photoemission events and detection methods allow for depth profiling within the material under investigation. Due to the nature of transmission experiments, the resulting spectra will provide bulk sensitive information. Similarly, FY measurements are also bulk sensitive as the depth sensitivity is governed by the penetration depth of the incident X-rays and the escape depth of the emitted photons (~ 100 nm in the soft X-ray region).[75] TEY measurements, on the other hand, are much more surface sensitive due to the depth sensitivity being a function of the escape depth of the electrons (~ 2 – 10 nm).[75] As briefly discussed in Section 1.4.2, electrons rapidly lose energy from inelastic scattering when travelling through a material. This means that only electrons which are generated near the surface of the material will have sufficient energy to escape and be detected. In this thesis, both soft and hard X-ray XANES techniques are used to probe the electronic structure of ceria NCs and $Au/CeO_2$ catalysts through the use of both TFY and TEY detection methods.

## 1.5. Thesis Overview

In this thesis, both the electronic and catalytic properties of ceria-based materials, including ceria NCs and $Au/CeO_2$ composites are discussed. Examining the various properties of these systems allows for a deeper fundamental understanding of how they behave under certain conditions.

The first objective of this thesis was to study the electronic properties of hydrothermally-synthesized ceria NCs. This was performed in order to determine how the concentration of $Ce^{3+}$ within the samples changed as a function of particle size. The changes associated with different Ce precursors and sample fractions were also investigated. High resolution Ce 3d and 4d XPS spectra were collected and analyzed for these purposes, along with Ce $M_{4,5}$- and $N_{4,5}$-edge XANES spectra. Through careful analysis, it was determined that the samples were experiencing severe damage associated with the high intensity X-ray beam in both the XPS and XANES measurements. Invaluable information was gained regarding the nature of the surface Ce species. This work is outlined in Chapter 2.

The second objective of this thesis was to build on the conclusions obtained from the first study, and investigate if the ceria NCs, with and without secondary metal NP catalysts, were

catalytically active towards the oxidation of benzyl alcohol. This is an essential organic reaction as it produces benzaldehyde, an important industrial precursor, as a major product. Various polymer-stabilized Au NPs, $Au_{25}(SR)_{18}/CeO_2$, and $Au/CeO_2$ catalysts were tested in this study. Working under optimized reaction conditions, the catalytic activity of the systems was followed by $^1H$ NMR spectroscopy. Au $L_3$-edge XANES and EXAFS measurements were also performed on two of the catalytic systems to better understand their differences. It was determined that the Au/bulk $CeO_2$ catalytic system showed the highest activity towards the tested benzyl alcohol oxidation reactions, while the $Au_{25}(SR)_{18}$/bulk $CeO_2$ system remained catalytically inert. This work is presented in Chapter 3.

# Chapter 2

# Ceria Nano-Cubes: Dependence of the Electronic Structure on Synthetic and Experimental Conditions [1]

## 2.1. Introduction

As outlined in Chapter 1, nanostructured ceria has gained increasing interest in the scientific community because of its unique redox capabilities. There have been many reports on the synthesis and characterization of ceria NPs having diverse shapes and sizes, and how these differences affect their redox capabilities.[17-22] Most of the literature which is focused on this area involves the study of the unit cell parameters of cubic $CeO_2$, and how the unit cell expands or contracts with varying [$Ce^{3+}$].[76,77] These reports show that smaller NPs have larger unit cell parameters, but it is unclear whether this correlation is due to an increased $Ce^{3+}$ presence in the smaller particles.[19]

X-ray and electron characterization techniques, such as XANES, XPS, and electron energy loss spectroscopy (EELS), are useful methods to investigate the presence of multiple oxidation states within a material. Using EELS, it has been shown that commercially available $CeO_{2-x}$ NPs contained a reduced $Ce^{3+}$ 'shell' that surrounded a 'core' composed mainly of $Ce^{4+}$.[78] The thickness of the 'shell' was found to be dependent upon the crystallographic surface type as well as the size of the NPs. This analysis showed that smaller particles (< 5 nm) appeared to be completely reduced (*i.e.* only $Ce^{3+}$ was observed) while larger particles (~ 30 nm) only contained a thin 'shell' of reduced $Ce^{3+}$. There has been significant interest for some time in examining how the $Ce^{3+}$ / $Ce^{4+}$ concentration varies as a function of particle size. It has been suggested that

[1] This chapter is adapted from a published manuscript. All of the experimental work and initial draft writing was carried out by M.N. Revoy. Copyright is owned by the American Chemical Society. Reprinted with permission from M.N. Revoy; R.W.J. Scott; A.P. Grosvenor. *J. Phys. Chem. C.* **2013**, 117, 10095-10105. DOI: 10.1021/jp3124814

smaller NPs contain a higher [$Ce^{3+}$].[79,80] This idea was explored by comparing the relative area ratios of the Ce $M_{4,5}$-edge EELS peaks of synthesized ceria NPs, and it was found that there was a greater [$Ce^{3+}$] as the particle size decreased.[79] The Ce L-, $M_{4,5}$- and O K-edge XANES spectra were also analyzed and exhibited similar trends.[80] A more recent report investigated how the defect concentration in polyhedral ceria NPs changed as a function of particle size and synthetic methodology.[19] It was established through the use of Ce K- and L-edge XANES that there was a correlation between the NP size and the unit cell parameters, where smaller NPs showed larger unit cell parameters. The results diverged from previous articles, however, as it was reported that the [$Ce^{3+}$] in the ceria NPs (2.0 - 9.6 nm) was less than 5 % and independent of the NP size.[19] The study also focused on the preparation method of the ceria NPs and showed that ceria NP samples prepared using a $Ce^{3+}$ precursor had a higher [$Ce^{3+}$] than those prepared using a $Ce^{4+}$ precursor, coinciding with previous observations.[19,22]

The aforementioned experiments were all performed under specific conditions to avoid damaging the ceria NPs by the characterization technique. It has been well established that photoreduction of $Ce^{4+}$ to $Ce^{3+}$ occurs when ceria is exposed to X-ray radiation.[81,82] The surface damage of bulk ceria has been previously studied as a function of irradiation time by XPS by collecting Ce 3d spectra after 15 and 300 minutes of X-ray exposure.[82] The Ce 3d XPS spectra revealed the reduction of $Ce^{4+}$ to $Ce^{3+}$ over time.[82] The Ce 4d spectra were also collected but were not as affected by the X-ray irradiation.[82] These spectra sample at a deeper depth than the Ce 3d spectra, suggesting that the X-ray damage was localized to the surface of the material.[82] It has also been suggested that vacuum conditions can affect the reduction of ceria.[83] A Ce 3d spectrum from micronsized $CeO_{2-x}$ was previously collected immediately after loading the sample in the ultra-high vacuum (UHV) sample chamber and then again after the sample was left in the chamber overnight.[83] Considerable differences were apparent between the spectra, with the initial spectrum being nearly identical to that of bulk $CeO_2$, with a calculated [$Ce^{3+}$] of 11.6 %, and the second spectrum being similar to that of bulk $Ce_2O_3$, with a [$Ce^{3+}$] of 29.3 %.[83] It is clear that the degree of ceria reduction depends on the X-ray irradiation time as well as other experimental conditions. In order to successfully reduce and / or eliminate the photoreduction that occurs in ceria NP samples, all of the experimental parameters must be taken into account, *i.e.* the photon flux (or the brightness of the X-ray source), the size of the X-ray beam, whether the sample chamber is under UHV or in air, the resolution of the instrument, the sample

irradiation time, and the synthetic methodology used. In an attempt to counter this effect, Turner *et al.* adjusted the beam dwell times on the samples and lowered the current for the reported Ce $M_{4,5}$-edge EELS experiments,[78] Wu *et al.* shortened the Ce $M_{4,5}$-edge EELS acquisition time to 2 seconds after seeing reduction within 30 seconds,[79] and Paun *et al.* acquired Ce L-edge XANES spectra over a period of 1 minute and only exposed the samples to irradiation during measurements using a fast shutter speed.[19] All of these methods seem to reduce the amount of sample damage observed, but in an inconsistent fashion. For example, the XANES experiments were conducted in air while the Ce $M_{4,5}$-edge EELS experiments, with resolution much higher than that of Ce K- and L-edge XANES, were performed under UHV, making comparison of the data difficult.

Here, a systematic study of the electronic properties of ceria NCs is reported. This is the first study of the electronic properties of such NCs. As a result of the growth mechanism, ceria NCs exhibit rough (002) surfaces which have the potential to provide unique catalytic opportunities.[18] The focus of this work was to methodically study how the electronic structure of the NCs change with variations in the particle size and Ce precursor used during synthesis. The effects associated with the characterization techniques on the samples were also investigated, as a secondary focus. TEM and powder X-ray diffraction (XRD) were used to characterize the morphology and size of the particles while high resolution XPS and XANES were used to determine the electronic properties of the NCs. As the activity of ceria-based catalytic systems depends on the degree of $Ce^{3+}$ on the surface of the particles, understanding the various properties of the particles and how to optimally measure the oxidation states of Ce should aid in the design of new and improved catalytic systems.

## 2.2. Experimental Methods

### 2.2.1. Materials

Cerium (III) nitrate hexahydrate [$Ce(NO_3)_3 \cdot 6H_2O$] (99.99%) was purchased from Sigma-Aldrich while cerium (IV) ammonium nitrate [$(NH_4)_2Ce(NO_3)_6$] (99.5%), oleic acid (OLA) (99%) and *tert*-butylamine (98%) were purchased from Alfa Aesar. All of the previously mentioned chemicals were used as obtained, without any further purification.

### 2.2.2. Synthesis of Ceria Nanocubes

The ceria NCs were synthesized using slight modifications of a previously reported method.[18] In a typical synthesis, appropriate amounts of aqueous cerium precursors, toluene (6.9 mL), OLA (0.70 mL), and *tert*-butylamine (0.07 mL) were added together in a 23 mL stainless steel Teflon-lined autoclave without stirring. The detailed parameters of the various syntheses are presented in Table 2.1. The sealed autoclave was placed in a furnace at 180 °C for 24 hours and then allowed to cool to room temperature after removal from the furnace. The resulting solution was centrifuged at 2500 rpm for 30 min using a Thermo Scientific Sorvall Biofuge Primo centrifuge and the initial precipitates were removed. These precipitates represent the fraction of larger NCs and are denoted here as fraction A. The remaining upper brown supernatant was then removed and further precipitated with a minimum volume of ethanol. These precipitates were isolated by further centrifugation. The centrifugation time and speed were optimized to ensure size selectivity. The final isolated product contained the fraction of smaller NCs, which are denoted as fraction B. The differences between the previously reported method and the one reported here include the size of the autoclave used, as well as the optimized centrifugation parameters.

**Table 2.1:** Detailed experimental parameters [a]

| Sample | $Ce(NO_3)_3 \cdot 6H_2O$ (g) | $(NH_4)_2Ce(NO_3)_6$ (g) | Molar ratio OLA:Ce(III/IV) | Fraction A or B [b] | Size (nm) [c] |
|---|---|---|---|---|---|
| 1 | 0.0976 | - | 9.9 | B | 5.8 ± 0.6 |
| 2 | 0.1204 | - | 8.0 | A<br>B | 8.0 ± 0.9<br>5.3 ± 0.7 |
| 3 | 0.0482 | - | 19.7 | B | 3.9 ± 0.5 |
| 4 | - | 0.1221 | 10.0 | B | 6.2 ± 0.6 |
| 5 | - | 0.1520 | 7.9 | A<br>B | 9.8 ± 1.5<br>4.8 ± 0.6 |
| 6 | - | 0.0607 | 20.0 | B | 3.3 ± 0.4 |
| 7 | 0.0518 | - | 18.3 | A<br>B | 11.8 ± 2.3<br>3.8 ± 1.1 |
| 8 | 0.0995 | - | 12.7 | A<br>B | 9.0 ± 1.6<br>6.0 ± 1.2 |
| 9 | 0.1248 | - | 10.1 | A<br>B | 7.9 ± 1.3<br>4.7 ± 1.1 |
| 10 | 0.1573 | - | 8.0 | A<br>B | 6.6 ± 1.6<br>5.1 ± 1.1 |
| 11 | 0.0534 | - | 18.0 | A<br>B | 6.8 ± 0.9<br>6.9 ± 0.8 |

*a.* The NC samples are labeled as "Sample # - fraction", *e.g.* Sample 1-B, throughout this chapter;

*b.* Fraction A represents the NCs that were initially precipitated out of solution after centrifugation, and Fraction B represents the second set of NCs that were precipitated using ethanol;

*c.* The average particle sizes were determined by TEM.

## 2.2.3. Characterization

A Philips 410 and a Philips CM10 electron microscope operating at 100 kV were used for TEM imaging. The samples were prepared by placing a drop of the ceria NC solution onto a carbon-coated Cu grid (Electron Microscopy Sciences, Hatfield, PA). To determine the average particle size, a minimum of 100 particles from each sample were manually measured using the ImageJ program.[63]

The ceria NC samples were analyzed with a PANalytical Empyrean powder XRD using a Cu $K_\alpha$ or Co $K_\alpha$ X-ray source. The samples were drop-coated onto a quartz disk and allowed to dry before analysis. The data was collected from 10 – 80 ° (2θ) at a scan rate of 0.02 ° per step. The resulting powder XRD patterns were analyzed using the X'Pert HighScore Plus program.[84]

XPS spectra were collected using a Kratos AXIS Ultra spectrometer and a monochromatic Al $K_\alpha$ (1486.7 eV) X-ray source. The resolution of the instrument was previously determined to be 0.4 eV.[85] The ceria NC solutions were drop-coated onto Au foil, allowed to dry, and then mounted on an electrically grounded sample holder. A charge neutralizer was used when more than one sweep of a spectrum was collected. High-resolution spectra of the Ce 3d, Ce 4d, O 1s, and C 1s core lines were collected using a pass energy of 20 eV, a step size of 0.05 eV, and a sweep time of 180 s. Data analysis was performed using the CasaXPS software program and all of the spectra were calibrated by setting the C 1s core-line peak arising from C-C / C-H interactions to 284.8 eV.[67] The spectral background was removed using a Shirley-type function and the spectra were fitted using component peaks having a combined Gaussian (70%) and Lorentzian (30%) line profile.[68]

Ce $M_{4,5}$-edge XANES spectra from the ceria NCs, bulk $CeO_2$ (Alfa Aesar, 99.9%), and bulk $CePO_4$ (Alfa Aesar, 99%) were collected using the Spherical Grating Monochromator beamline (SGM, 11ID-1) located at the Canadian Light Source (CLS). The photon flux of this beamline is 4 x $10^{12}$ photons/(s·0.1% bandwidth) at 250 eV and decreases to $10^{11}$ photons/(s·0.1% bandwidth) at 1900 eV; the resolution of the beamline is 0.3 eV at energies below 1500 eV.[86] Powdered samples were deposited on carbon tape while the liquid NC samples were drop-coated onto Al foil and allowed to dry prior to being loaded into the vacuum chamber. Ce $M_{4,5}$-edge spectra were collected using the TEY mode and were measured by stepping the

excitation energy by 0.1 eV increments through the absorption edges. The attenuation length of the incident X-rays was calculated to be ~ 93 nm through the absorption edge.[70] To investigate the effect of photon flux on the samples, Ce $M_{4,5}$-edge spectra were collected before and after detuning the undulator of the SGM beamline. Detuning the undulator resulted in a much lower photon flux being seen by each sample compared to when the undulator was tuned. All spectra were calibrated by collecting spectra from Cu metal, which has a well-known absorption energy (Cu $L_3$-edge: 932.7 eV).[87]

The Ce $N_{4,5}$-edge XANES spectra were collected using the Variable Line Spacing Plane Grating Monochromator beamline (VLS-PGM, 11ID-2) located at the CLS. The photon flux is 2 x $10^{11}$ photons/(s·0.1%bandwidth) from 9 - 240 eV, and the resolution is better than 0.01 eV at 100 eV.[88] The spectra from powdered samples were deposited on carbon tape while the NC samples were drop-coated onto Al foil and collected in TFY mode. The excitation energy was stepped by 0.05 eV increments through the absorption edge, and the attenuation length of the incident X-rays was calculated to be ~ 7 nm through the absorption edge.[70] Spectra from sulfur powder were collected as a calibration standard, and the S $L_3$-edge absorption energy was set to its accepted value of 162.5 eV.[87] All of the XANES spectra collected during this study were analyzed using the Athena software program.[89]

## 2.3. Results and Discussion

### 2.3.1. TEM Imaging

The morphology and size of the ceria NCs were examined by TEM. Figure 2.1 shows typical TEM images of the NCs as well as their particle size distributions. All of the TEM images displayed well defined, monodisperse NCs regardless of the changes in synthetic parameters. The average particle sizes and standard deviations are presented in Table 2.1. The synthetic methodology showed high size selectivity as the larger particles were contained in the A fractions, while the smaller particles were contained in the B fractions.

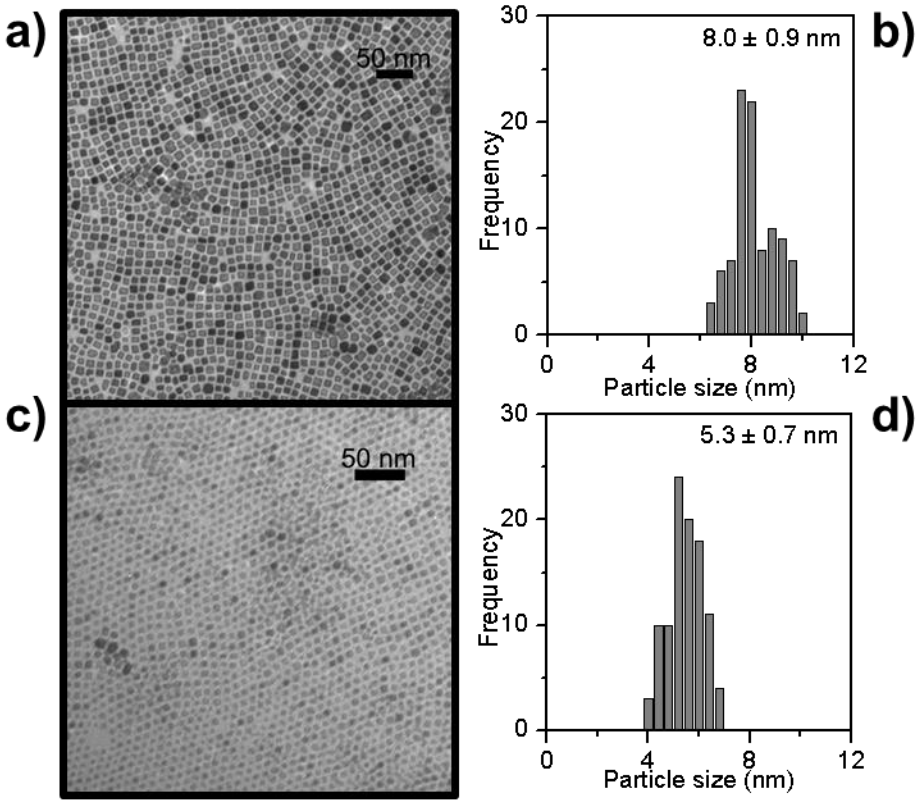


**Figure 2.1: a)** TEM image of ceria NC sample 2-A (50 nm scale bar), **b)** Particle size distribution of sample 2-A, **c)** TEM image of ceria NC sample 2-B (50 nm scale bar), and **d)** Particle size distribution of sample 2-B.

## 2.3.2. XRD

The powder XRD patterns for all of the ceria NC samples are shown in Figure 2.2. The main diffraction peak in all of the XRD patterns corresponds to the (002) planes of the cubic phase of ceria ($Fm\bar{3}m$). Peaks corresponding to the (220), (311), (222) and (331) diffraction planes were not observed. As the ceria NCs are smaller than 10 - 15 nm, the detected peaks displayed Scherrer broadening effects. The powder XRD patterns from sample 2-A, 5-A and 5-B also exhibited a low intensity (111) diffraction peak. The presence of this peak indicates that although there is a significant preferred orientation effect, the NCs did not assemble into perfectly flat layers when deposited on the quartz disk prior to analysis. These results are similar to those previously reported for ceria NCs.[18]

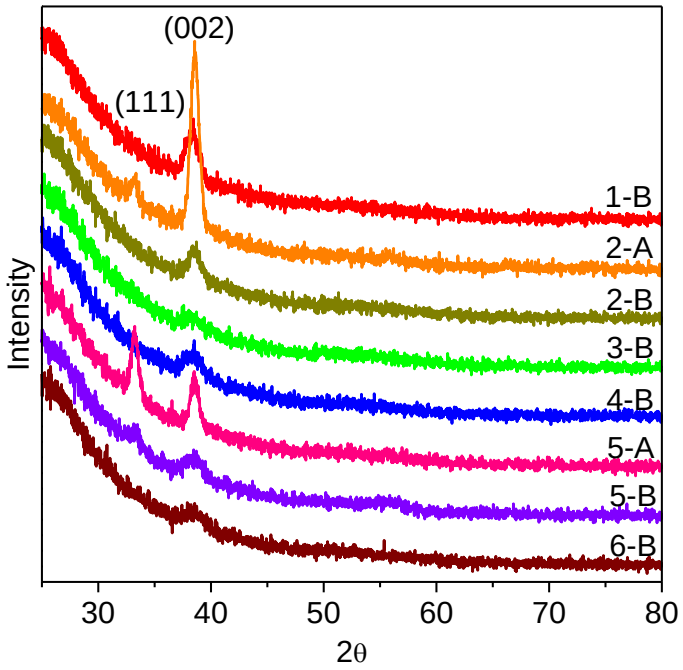


**Figure 2.2:** Powder XRD patterns from the ceria NC samples.

## 2.3.3. Ce 3d and 4d XPS

### 2.3.3.1. Ce 3d XPS spectra

Typical high resolution Ce 3d XPS spectra are shown in Figure 2.3. Twelve peaks corresponding to six pairs of spin-orbit split peaks were used to fit the spectrum from bulk $CeO_2$. The bulk $CeO_2$ standard spectrum used in this study contained traces of $Ce^{3+}$ as a result of surface defects, *i.e.* oxygen vacancies within the material. The Ce $3d_{5/2}$ components are labeled as v and u, referring to the $Ce^{4+}$ and $Ce^{3+}$ components respectively, while the Ce $3d_{3/2}$ components are labeled as v' and u'. The multiple components representing the spin-orbit split peaks in the spectrum from bulk $CeO_2$ ($Ce^{4+}$) arise from the different Ce 4f occupancies in the final state ($4f^{0,1,2}$), as well as the presence of satellite peaks.[90] Kaindl *et al.* described three possible final states which can arise from the excitation of a Ce 3d core electron; Ce $3d^9$ $4f^0$ O $2p^6$, Ce $3d^9$ $4f^1$ O $2p^5$, and Ce $3d^9$ $4f^2$ O $2p^4$.[90] The Ce $4f^0$ final state is the most predominant, while the $4f^{1,2}$ final states arise from possible hybridization between the Ce 4f and O 2p levels.[90] The Ce 3d spectra from bulk $CeCl_3$ and $CePO_4$ ($Ce^{3+}$) show two pairs of spin-orbit split peaks. The broad peak at 896 eV in the $CeCl_3$ spectrum could be the result of sample charging effects, as it is not commonly observed in spectra from $Ce^{3+}$ compounds. The spectra presented in Figure 2.3 are consistent with those previously reported and were fitted using a modified version of a previously reported peak fitting procedure.[83,91-93]

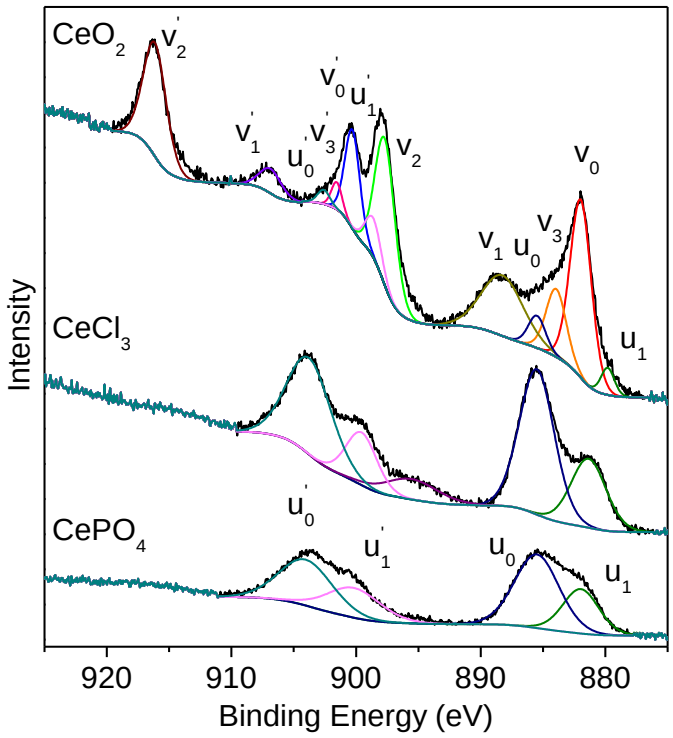


**Figure 2.3:** Fitted Ce 3d XPS spectra from bulk $CeO_2$, $CeCl_3$, and $CePO_4$.

There has been much controversy in the literature regarding the true assignment of the various $Ce^{3+}$ and $Ce^{4+}$ photoemission components in the Ce 3d spectrum of ceria and substituted ceria compounds.[94] Most of the disagreement lies in the assignment of the features at lower binding energy (BE) vs. higher BE within the Ce $3d_{5/2}$ and $3d_{3/2}$ spin-orbit split spectrum.[94] Out of the many explanations, the most common interpretation involves a ligand-to-metal shake-up process, where the lower BE peak represents the core-line, and the higher BE peak represents a shake-up satellite.[94,95] Shake-up satellites arise from a secondary process which can occur once an atom has been excited and a photoelectron has been ejected. The process involves the excitation of a valence electron on the ligand to an empty conduction state on the metal.[94] This process reduces the kinetic energy of the photoelectron, which is observed in the spectrum as an increase in BE. In the spectrum of bulk $CePO_4$, the lowest BE peaks in each spin-orbit doublet, here labeled as $u_1$ and $u_1$', represent the core-lines while the higher BE peaks, $u_0$ and $u_0$', are

shake-up satellites.[95] A similar assignment holds for the spin-orbit split doublets in the spectrum of bulk $CeO_2$.

The assignment of the various transitions associated with each peak is quite difficult; however, the core-lines arising from the multiple Ce $4f^{0,1,2}$ final states appear at lower BE while the shake-up transitions appear at higher BE.[95] The peaks here labeled as $v_3$ and $v_3$' have not been previously recognized as distinct peaks by other researchers, though similar spectral features have been observed.[91] Previously, these peaks were accounted for by assuming that components $v_o$ and $v_o$' were asymmetric in nature, which reduced the total number of fitted peaks in the Ce 3d spectra from $Ce_xMn_{1-x}O_{2-y}$.[91,92] It is proposed here that these features, $v_3$ and $v_3$', are related to a $Ce^{4+}$ component. The identification of the individual peak transitions is beyond the scope of this thesis as only the integrated peak areas of the fitted component peaks were used to calculate the relative [$Ce^{3+}$] in the ceria NC samples.[91] This method of analysis does induce some degree of error in the peak assignments since it was assumed that each component was related solely to a $Ce^{3+}$ or $Ce^{4+}$ contribution. Some of components could consist of an overlap of contributions from both Ce oxidation states.

The Ce 3d XPS spectra were obtained for ceria NC samples 1 – 6 (see Table 2.1). In order to ensure that minimal / no X-ray damage had occurred, a single sweep of each spectrum was initially collected, where a single sweep of a sample took ~ 3 minutes of data collection time. The changes associated with prolonged X-ray exposure were studied through the analysis of spectra collected by averaging 20 sweeps of the spectra. After 20 sweeps, the samples were exposed to X-ray irradiation for ~ 90 minutes. As the total X-ray exposure time is an approximation, due to the ~ 1.5 minutes of detector dead time per sweep, the various spectra to be discussed will be solely associated with the total number of sweeps collected.

Figure 2.4 presents the fitted Ce 3d spectra of ceria NC samples 1 – 6 collected after a single sweep of each spectrum. The spectra were fitted using the above mentioned fitting procedure, and the component BEs are listed in Table 2.2.[91] The $Ce^{4+}$ component was fitted with 8 peaks: $v_0$ (BE ~ 882.36 eV), $v_3$ (BE ~ 883.96 eV), $v_1$ (BE ~ 888.71 eV), $v_2$ (BE ~ 898.09 eV), $v_0$' (BE ~ 900.78 eV), $v_3$' (BE ~ 901.99 eV), $v_1$' (BE ~ 907.63 eV), and $v_2$' (BE ~ 916.57 eV). The $Ce^{3+}$ component, on the other hand, was fitted with 4 peaks: $u_1$ (BE ~ 880.58 eV), $u_0$ (BE ~ 885.39 eV), $u_1$' (BE ~ 899.07 eV), and $u_0$' (BE ~ 903.35 eV). Additional constraints were

applied to reduce the error in the curve fitting procedure. The individual peak positions, the full-width at half maximum (FWHM) of the peaks, as well as the peak areas were restricted during fitting. The FWHM of the components was constrained to within ± 0.3 eV for both the $Ce^{3+}$ and $Ce^{4+}$ contributions; the average FWHM values are listed in Table 2.3. Even though a single sweep of the spectrum exhibited a low signal-to-noise ratio, the added constraints increased the precision of the curve fitting procedure.

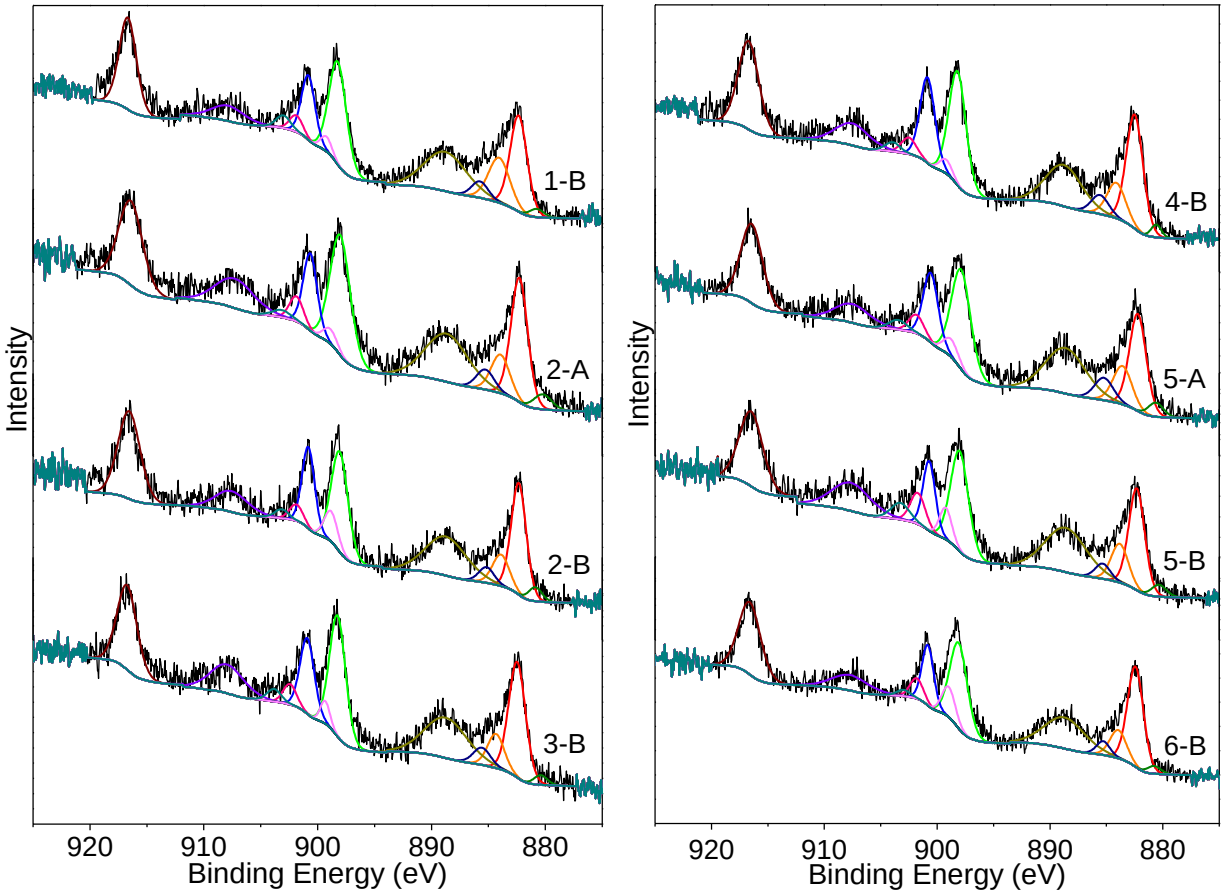


**Figure 2.4:** Fitted Ce 3d XPS spectra from ceria NC samples 1−6 collected after 1 sweep

**Table 2.2:** Energy positions, in eV, of the spectral components used to fit the Ce 3d spectra collected after a single sweep, and calculated [$Ce^{3+}$] in the ceria NC samples

| Entry | $v_o$ | $v_3$ | $v_1$ | $v_2$ | $v_o'$ | $v_3'$ | $v_1'$ | $v_2'$ | $u_1$ | $u_o$ | $u_1'$ | $u_o'$ | [$Ce^{3+}$] (%) |
|---|---|---|---|---|---|---|---|---|---|---|---|---|---|
| **1-B** | 882.34 | 884.06 | 888.80 | 898.23 | 900.91 | 901.88 | 907.87 | 916.67 | 880.76 | 885.75 | 899.24 | 903.01 | 7.5 |
| **2-A** | 882.28 | 883.94 | 888.68 | 898.02 | 900.65 | 901.87 | 907.29 | 916.41 | 880.23 | 885.27 | 898.90 | 903.16 | 7.6 |
| **2-B** | 882.33 | 883.89 | 888.73 | 898.06 | 900.81 | 901.87 | 907.56 | 916.56 | 880.88 | 885.16 | 898.83 | 903.15 | 9.3 |
| **3-B** | 882.47 | 884.34 | 888.75 | 898.25 | 900.92 | 902.44 | 907.95 | 916.74 | 880.41 | 885.57 | 899.34 | 903.83 | 7.5 |
| **4-B** | 882.49 | 884.12 | 888.78 | 898.19 | 900.85 | 902.51 | 907.52 | 916.70 | 880.59 | 885.57 | 899.21 | 903.94 | 7.1 |
| **5-A** | 882.22 | 883.57 | 888.64 | 897.87 | 900.57 | 901.85 | 907.52 | 916.43 | 880.62 | 885.22 | 898.79 | 903.45 | 9.9 |
| **5-B** | 882.31 | 883.81 | 888.60 | 898.01 | 900.71 | 901.71 | 907.63 | 916.47 | 880.34 | 885.33 | 899.24 | 903.27 | 9.8 |
| **6-B** | 882.42 | 883.95 | 888.72 | 898.09 | 900.83 | 901.81 | 907.69 | 916.60 | 880.78 | 885.28 | 898.98 | 902.99 | 9.0 |
| **Mean** | 882.36 | 883.96 | 888.71 | 898.09 | 900.78 | 901.99 | 907.63 | 916.57 | 880.58 | 885.39 | 899.07 | 903.35 | 8.5 |
| **Ref.** | | | | | | | | | | | | | |
| **[91]** | 882.1 | - | 888.1 | 897.9 | 900.8 | - | 906.6 | 916.2 | 880.2 | 884.8 | 898.2 | 903.4 | - |
| **[96]** | 882.2 | - | 888.6 | 898.0 | 900.7 | - | 907.2 | 916.5 | 880.6 | 884.4 | 899.3 | 903.9 | - |

**Table 2.3:** The average FWHM values, in eV, of the component peaks used to fit the Ce 3d spectra from the ceria NC samples

| # Sweeps | $v_o$ | $v_3$ | $v_1$ | $v_2$ | $v_o'$ | $v_3'$ | $v_1'$ | $v_2'$ | $u_1$ | $u_o$ | $u_1'$ | $u_o'$ |
|---|---|---|---|---|---|---|---|---|---|---|---|---|
| 1 | 1.70 | 1.87 | 4.20 | 1.86 | 1.40 | 1.45 | 3.67 | 2.20 | 1.46 | 1.70 | 1.32 | 1.62 |
| 20 | 2.21 | 1.82 | 3.08 | 2.04 | 1.65 | 1.62 | 2.47 | 2.03 | 1.68 | 2.72 | 1.55 | 2.02 |

As previously mentioned, there have been many studies which have found that with decreasing particle size, the [$Ce^{3+}$] increases in ceria containing materials.[79,80] It is evident from the Ce 3d spectra presented in Figure 2.4 that this is not the case for the ceria NCs studied here. Based on a visual inspection of the spectra, all of the samples seem to be predominately composed of $Ce^{4+}$ (*c.f.* the Ce 3d spectrum from bulk $CeO_2$ in Figure 2.3). This result alone is quite interesting as the synthesized ceria NCs studied here have a variety of sizes and were synthesized using different Ce precursors. To confirm this observation, the relative [$Ce^{3+}$] in the ceria NCs was calculated using the following equations:

$$Ce(III) = u_1 + u_0 + u_1' + u_0' \quad (2.1)$$

$$Ce(IV) = v_0 + v_3 + v_1 + v_2 + v_0' + v_3' + v_1' + v_2' \quad (2.2)$$

$$[Ce^{3+}] = \frac{Ce(III)}{Ce(III)+Ce(IV)} \quad (2.3)$$

where Ce(III) and Ce(IV) represent the sums of the integrated peak areas of the various $Ce^{3+}$ and $Ce^{4+}$ components.[83] The calculated [$Ce^{3+}$] values are listed in Table 2.2 and range from ~ 7 to < 10 %. This is in good agreement with the observation made previously, that the spectra presented in Figure 2.4 do not change with varying size of the ceria NCs. This statement gives credence to the results reported by Paun *et al.* where it was suggested that the [$Ce^{3+}$] was ~ 5 % regardless of the size of the polycrystalline NPs studied, which is slightly lower than that reported here.[19] There could be several reasons for this discrepancy. The ceria NCs studied here exhibit exposed (002) surfaces and defined edges while the polyhedral particles studied by Paun *et al.* do not, affecting the number of surface defects present in the material.[19] Also, the Ce 3d XPS spectra

reported here are of a much higher resolution than the Ce K-edge XANES spectra reported by Paun *et al.*[19] The relative [$Ce^{3+}$] was also studied as a function of the preparation method, *i.e.* whether the samples were synthesized using a $Ce^{3+}$ or $Ce^{4+}$ precursor. The results presented here indicate that the relative [$Ce^{3+}$] remains relatively constant irrespective of the Ce precursor used. Thus, it has been shown that the [$Ce^{3+}$] on the surface of the synthesized ceria NCs does not change considerably with variations in particle size and / or Ce precursor used during synthesis.

The effect of prolonged X-ray irradiation on the NCs was studied by comparing spectra collected after averaging 20 sweeps. Figure 2.5 illustrates the fitted Ce 3d spectra from the ceria NC samples after 20 sweeps were collected; the component BEs are listed in Table 2.4. In a similar fashion to the fitting applied to the spectra collected after a single sweep, the FWHM of the components were constrained to within ± 0.3 eV for both the $Ce^{3+}$ and $Ce^{4+}$ contributions (Table 2.3).

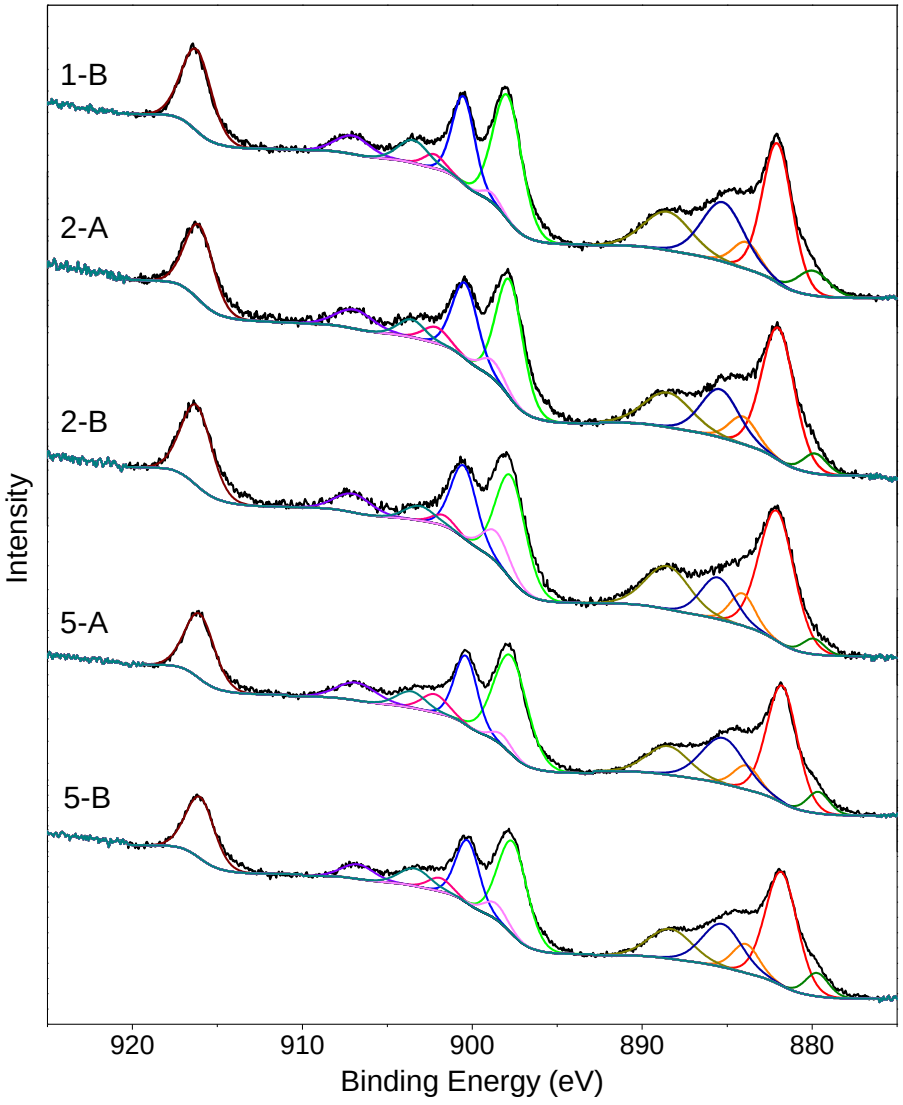


**Figure 2.5:** Fitted Ce 3d XPS spectra from ceria NC samples 1, 2, and 5 collected after 20 sweeps.

**Table 2.4:** Energy positions, in eV, of the spectral components used to fit the Ce 3d spectra collected after 20 sweeps and the calculated [$Ce^{3+}$] in the ceria NC samples

| Entry | $v_o$ | $v_3$ | $v_1$ | $v_2$ | $v_o'$ | $v_3'$ | $v_1'$ | $v_2'$ | $u_1$ | $u_o$ | $u_1'$ | $u_o'$ | [$Ce^{3+}$] (%) |
|---|---|---|---|---|---|---|---|---|---|---|---|---|---|
| **1-B** | 882.04 | 883.87 | 888.51 | 897.92 | 900.50 | 902.23 | 907.04 | 916.22 | 879.95 | 885.24 | 898.87 | 903.46 | 21.0 |
| **2-A** | 882.00 | 884.06 | 888.50 | 897.80 | 900.42 | 902.16 | 906.93 | 916.07 | 879.82 | 885.42 | 898.81 | 903.58 | 17.5 |
| **2-B** | 882.09 | 884.10 | 888.51 | 897.73 | 900.50 | 901.72 | 907.03 | 916.22 | 879.92 | 885.55 | 898.60 | 903.10 | 16.1 |
| **5-A** | 881.77 | 883.85 | 888.48 | 897.73 | 900.37 | 902.20 | 906.81 | 916.03 | 879.63 | 885.24 | 898.26 | 903.58 | 19.1 |
| **5-B** | 881.80 | 883.90 | 888.34 | 897.62 | 900.27 | 901.90 | 906.73 | 916.00 | 879.71 | 885.30 | 898.63 | 903.37 | 20.4 |
| **Mean** | 881.94 | 883.96 | 888.47 | 897.76 | 900.41 | 902.04 | 906.91 | 916.11 | 879.81 | 885.35 | 898.63 | 903.42 | 18.8 |
| **Ref.** | | | | | | | | | | | | | |
| **[91]** | 882.1 | - | 888.1 | 897.9 | 900.8 | - | 906.6 | 916.2 | 880.2 | 884.8 | 898.2 | 903.4 | - |
| **[96]** | 882.2 | - | 888.6 | 898.0 | 900.7 | - | 907.2 | 916.5 | 880.6 | 884.4 | 899.3 | 903.9 | - |

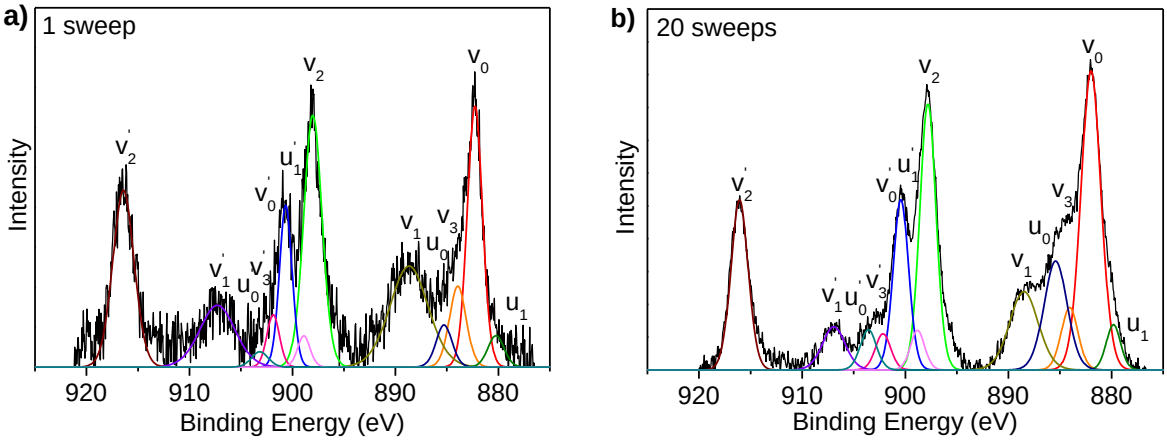


**Figure 2.6:** Background subtracted and fitted Ce 3d XPS spectra from ceria NC sample 2-A after collection of **a**) 1 sweep and **b)** 20 sweeps.

A comparison of the fitted Ce 3d spectra from sample 2-A taken after a single sweep and again after 20 sweeps is shown in Figure 2.6. It is evident from this comparison that the features associated with $Ce^{3+}$ ($u_0$ and $u_0$') increase in intensity as the X-ray irradiation time increases. It has been previously shown that the formation of $Ce^{3+}$ within a material is characterized by an increase in the intensity of the features associated with $Ce^{3+}$ along with the broadening of the lower BE peak ($u_1$), over time.[82] From Table 2.3, it can be noted that this is the case for the Ce 3d spectra presented here, as the FWHM of the lower BE peak broadens over time; from 1.46 eV after 1 sweep to 1.68 eV after 20 sweeps. The relative [$Ce^{3+}$] from the spectra collected after averaging 20 sweeps was calculated utilizing equations 2.1 – 2.3 and is presented in Table 2.4. The calculated [$Ce^{3+}$] values range from ~ 16 to 21 %, demonstrating a clear increase in the [$Ce^{3+}$] after prolonged X-ray irradiation. Some of the variation in the calculated [$Ce^{3+}$] may be accounted for by fitting errors as the samples may not be reduced to the same extent due to small differences in sample thickness and concentration. Given that the spectra were collected by averaging over 20 sweeps, the calculated relative [$Ce^{3+}$] is slightly underestimated, therefore underestimating the degree of reduction which is occurring within the NC samples.

Figure 2.7 illustrates how the relative [$Ce^{3+}$] varies as a function of the particle size and Ce precursor for all of the ceria NC samples studied; the results obtained by Paun *et al.* are also presented for comparison.[19] It is quite evident from the plot that the individual sample conditions (*i.e.* size and preparation method) do not strongly influence the calculated [$Ce^{3+}$]. In order to ensure that the X-ray induced reduction occurred gradually over time, a comparison between spectra collected after averaging an intermediate number of sweeps was performed. A comparison between spectra collected after 1, 7 and 20 sweeps was performed for two of the ceria NC samples (1 and 4) and it was clear that the $Ce^{3+}$ features increased in intensity with increasing number of sweeps. As the X-ray induced reduction of $Ce^{4+}$ was not the main focus of this chapter, the actual rate of reduction was not fully investigated. The fact that X-ray induced reduction was occurring at all was the primary focus so that it could be minimized / eliminated.

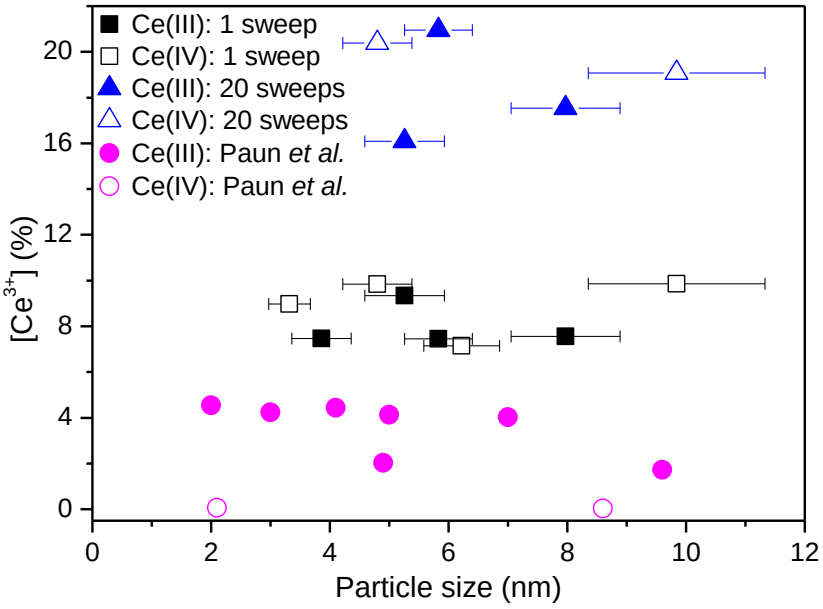


**Figure 2.7:** The calculated [$Ce^{3+}$] from the Ce 3d spectra collected after 1 and 20 sweeps as a function of the ceria NC size. The data obtained by Paun *et al*. is also shown for comparison.[19] The Ce(III) and Ce(IV) denoted in the legend refer to the oxidation state of the Ce precursor used during synthesis.

There are several proposed mechanisms associated with the reduction of ceria after long exposure to X-ray irradiation. One mechanism suggests that the damage may be due to a large number of low energy photoelectrons having high or favorable cross sections for dissociation or desorption which could initiate chemical changes within the material.[97] Another mechanism suggests that the damage is due to the creation of holes in the valence band via Auger decay.[82] This process is then followed by electron shake-up transitions that lead to the occupancy of the conduction states, reducing $Ce^{4+}$ to $Ce^{3+}$. Yet another mechanism relates the reduction of $Ce^{4+}$ to intense local heating of the sample surface by the X-ray beam as it has been demonstrated that ceria undergoes decomposition when it is heated to temperatures greater than 627 °C.[81,92] Some studies have also proposed that the UHV conditions in the sample chamber, along with the X-ray beam, are responsible for some of the damage seen in ceria-containing samples.[19,83] Zhang *et al.* suggested that the high [$Ce^{3+}$] observed was the result of surface reduction in the UHV chamber.[83] This reduction process is enhanced by the fast reaction kinetics located at the NP surfaces.[83] In this current study, the UHV conditions in the XPS experiments did not seem to affect the collected spectra. A single sweep of the core-line spectra was collected almost immediately after the samples were loaded into the chamber, and again after ~ 24 hours. No changes were apparent in the spectra that would suggest the gradual reduction of $Ce^{4+}$. This observation indicates that the noted surface reduction / damage on the ceria NCs is due, at least primarily, to X-ray irradiation. Further experimental and theoretical work is needed to fully understand the X-ray induced reduction process, as the true mechanism associated with the reduction of $Ce^{4+}$ on the surface of ceria containing compounds after X-ray irradiation has not yet been ascertained.

### 2.3.3.2. Ce 4d XPS spectra

The Ce 4d spectra were analyzed in this study to investigate how the reduction of $Ce^{4+}$ occurred as a function of sample depth within the ceria NC samples. During the collection of the Ce 3d spectra, the ejected photoelectrons have an IMFP of ~ 1.2 nm and a sampling depth (3λ) of ~ 3.6 nm, while the ejected Ce 4d photoelectrons have an IMFP of ~ 2.2 nm and a sampling depth of ~ 6.6 nm.[98] (The IMFPs were calculated using the QUASES – IMFP – TPP2M program.[99]) The differences in the IMFPs of the photoelectrons allow for both surface and 'bulk' sensitive measurements. Typical Ce 4d XPS spectra are shown in Figure 2.8a. The highest BE peaks in the spectrum of bulk $CeO_2$, labeled as W''' and X''', refer to the Ce $4d_{3/2}$ and $4d_{5/2}$ components, respectively, and were labeled following the convention established by Burroughs *et al.*[92] The lower BE peaks (A, B, C), however, cannot be separated into spin-orbit split doublets.[92,93] The Ce 4d spectra from bulk $CePO_4$ and $CeCl_3$ exhibit typical line shapes for $Ce^{3+}$ containing compounds.[92,93] As with the Ce 3d spectra, the assignment of the individual transitions associated with each peak is beyond the scope of this study. As the Ce 4d spectra are much more complex than the Ce 3d spectra, the application of a simple peak fitting procedure was not possible for quantification. The two high BE features (W''' and X''') are reported to be solely associated with $Ce^{4+}$, as they are completely absent in spectra of $Ce^{3+}$ containing compounds.[93] These peaks, at higher BE, were therefore the main indicators for the presence of either $Ce^{3+}$ or $Ce^{4+}$ in the ceria NC samples.

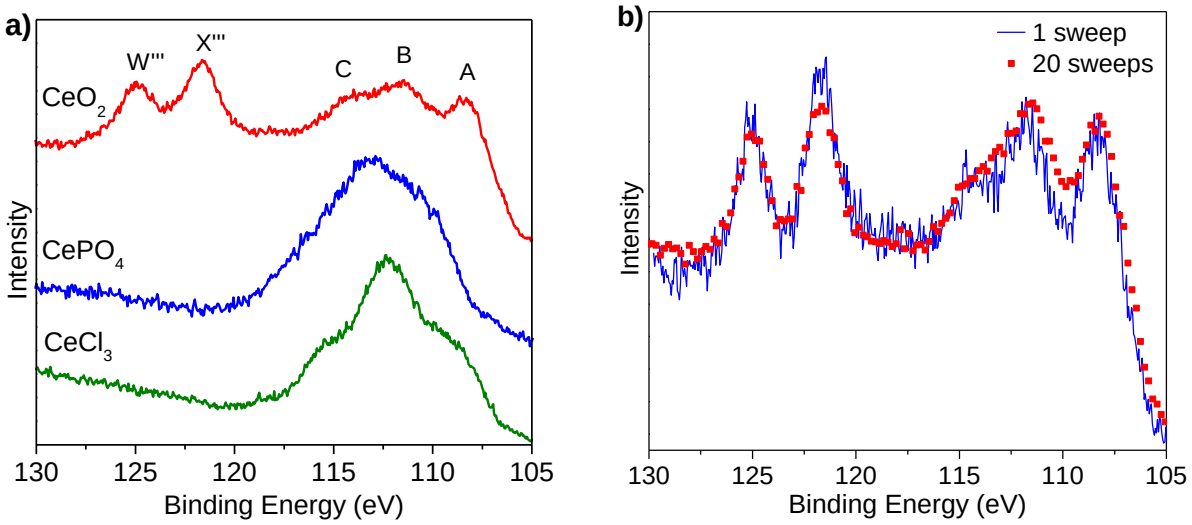


**Figure 2.8:** Ce 4d spectra from **a)** bulk $CeO_2$, $CePO_4$ and $CeCl_3$, and **b)** ceria NC sample 2-A after a total of 1 and 20 sweeps.

The Ce 4d spectra were collected from ceria NC samples 1 – 6 (see Table 2.1). Figure 2.8b illustrates a comparison between the Ce 4d spectra of sample 2-A taken after a single sweep and again after 20 sweeps. The collected Ce 4d spectra from the remainder of the ceria NC samples are presented in Figure 2.9. All of the ceria NC samples showed similar trends as those presented in Figure 2.8b. The spectrum that was collected after a single sweep resembles that of bulk $CeO_2$ (Figure 2.8a) while the spectrum of the sample irradiated for a longer period of time is similar, but does show some changes. The W''' and X''' peaks show a slight decrease in intensity while the lower BE peaks show some broadening over time, which is indicative of the formation of some $Ce^{3+}$.[93] Since the differences between the spectra are slight, it is reasonable to conclude that the degree of reduction of $Ce^{4+}$ identified in the Ce 4d spectra after 20 sweeps is minor in comparison to that observed in the Ce 3d spectra. This illustrates that most of the damage occurred at the surface of the ceria NC samples, as the collected Ce 3d spectra are more surface sensitive than the Ce 4d spectra.

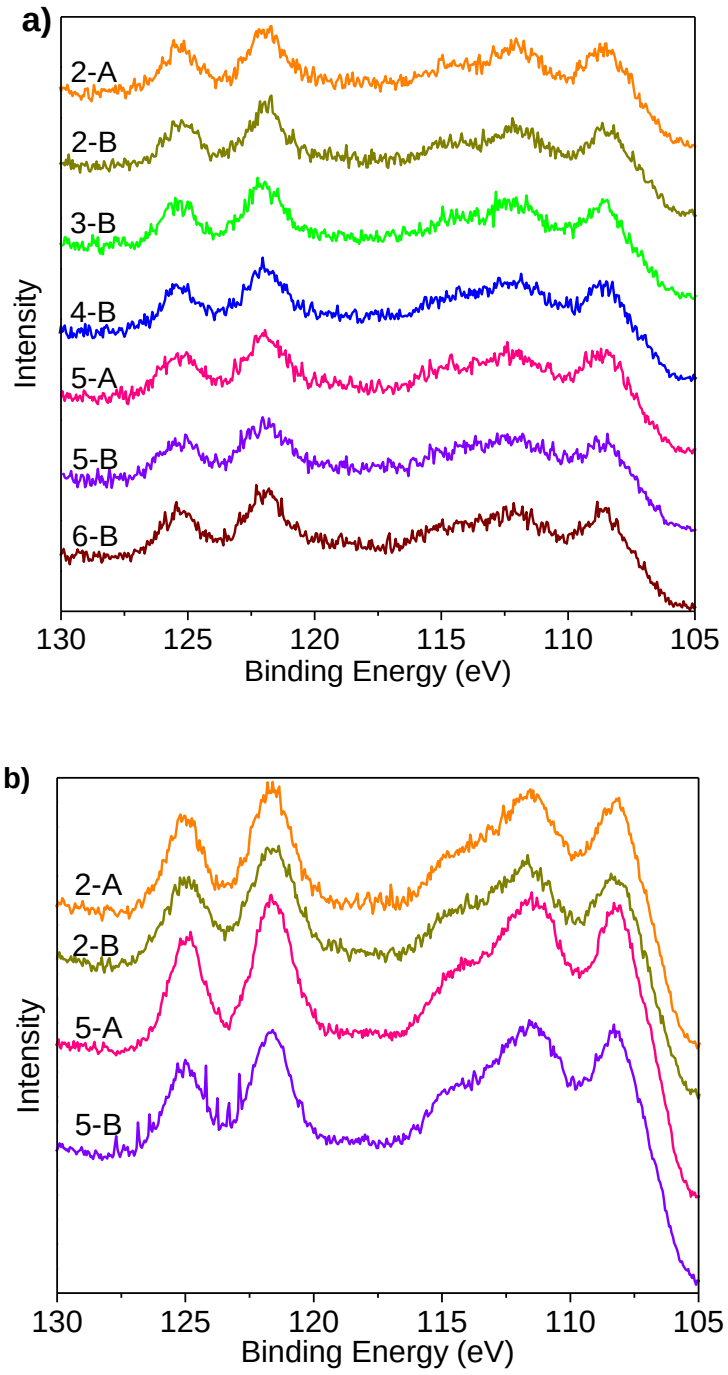


**Figure 2.9:** Ce 4d XPS spectra from the ceria NC samples after **a)** 1 sweep and after **b)** 20 sweeps.

## 2.3.4. Ce $M_{4,5}$- and $N_{4,5}$-edge XANES

The Ce $M_{4,5}$- and $N_{4,5}$-edge XANES spectra from the ceria NCs were also collected and analyzed in an attempt to further understand the electronic properties of these materials. The Ce $M_{4,5}$-edge spectra probe deeper into the sample than the Ce $N_{4,5}$-edge spectra, allowing for a more bulk sensitive measurement (see Section 2.2.3). Figure 2.10 depicts the collected Ce $M_5$-edge spectra from ceria NC samples 9-A and 10-A, as well as spectra from standard materials.

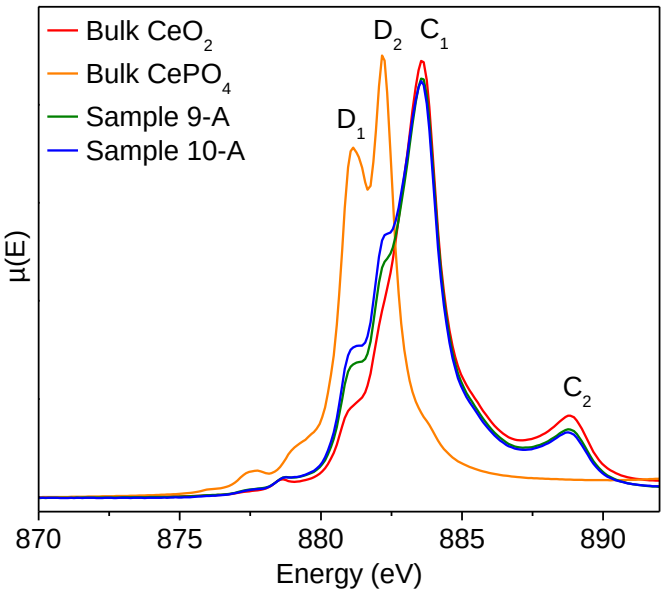


**Figure 2.10:** Ce $M_5$-edge XANES spectra from bulk $CeO_2$ and $CePO_4$, and ceria NC samples 9-A and 10-A.

The Ce $M_5$-edge (Figure 2.10) represents one of the two spin-orbit split peaks arising from the transition of Ce 3d electrons into unoccupied Ce 4f states. The spectrum from bulk $CeO_2$ shows two main features, labeled $C_1$ and $C_2$, which are indicative of $Ce^{4+}$.[100] The spectrum from bulk $CePO_4$ also shows two main features, labeled $D_1$ and $D_2$, and these features are indicative of $Ce^{3+}$.[100] From the spectra from the ceria NC samples presented in Figure 2.10, it is clear that there are differences between sample 9-A and the smaller sample 10-A (*c.f.* Table 2.1).

The relative intensities of the $D_1$ and $D_2$ features are greater in sample 10-A, implying that the smaller NC sample has a slightly higher [$Ce^{3+}$]. Analyzing these results alone would lead one to believe that previous authors are correct in their conclusions regarding the relationship between the particle size and the [$Ce^{3+}$].[79,80] However, the XPS results presented here indicate that this is not the case. The observed difference between the XPS and XANES measurements is most likely due to the X-ray induced damage incurred by the ceria NCs. All of the XANES spectra were collected using a synchrotron radiation source, which offers a higher photon flux (higher brightness) than metal X-ray sources used in typical XPS experiments. The brightness of a typical laboratory XPS instrument is on the order of $10^8$ – $10^{10}$ photons/(s·mm$^2$·mrad$^2$·0.1% bandwidth) while the brightness of synchrotron generated light is on the order of $10^{19}$ photons/(s·mm$^2$·mrad$^2$·0.1% bandwidth).[101,102] It is presumed here that this increased brightness is responsible for reducing the ceria NC surface almost immediately upon exposure, which would account for the observed changes between the XANES and XPS spectra. The differences in the energy of the incident X-rays could also be an attributing factor. Considering that smaller NCs have a larger surface contribution, these NCs would show a greater degree of damage over time. It has been previously suggested that the majority of the reduced $Ce^{4+}$ is present on the surface of ceria NPs and therefore the reduction would show a dependence on the NP size.[19,82] This trend was however not observed in the collected XPS spectra. To confirm this hypothesis, the photon flux used during the collection of the Ce $M_{4,5}$-edge spectra was decreased. This was accomplished by detuning the undulator of the SGM beamline. Figure 2.11 demonstrates the effects that both a high and low photon flux have on a ceria NC sample. It is clear from the spectra that the higher photon flux reduces the sample to a greater extent compared to when the photon flux is lowered. This trend was observed for a variety of ceria NC samples studied. This observation demonstrates that the intensity of the incoming X-ray beam, i.e. the photon flux, has a dramatic effect on the reduction of $Ce^{4+}$ within the samples.

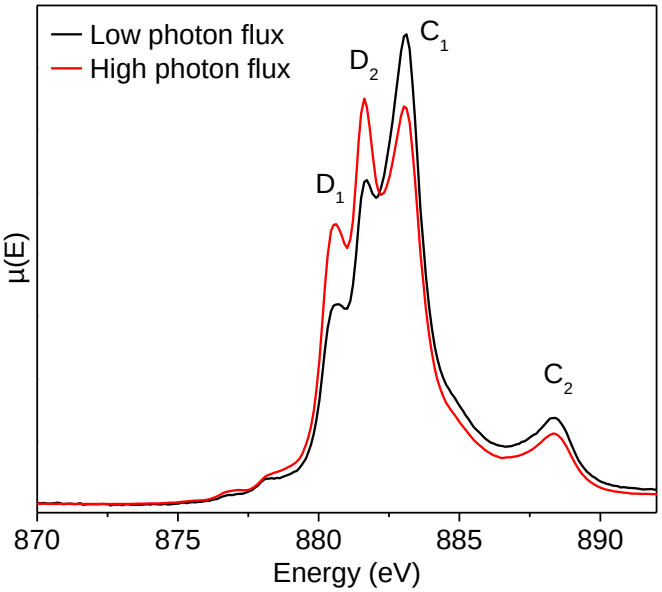


**Figure 2.11:** Ce $M_5$-edge XANES spectra from ceria NC sample 11-A collected using both a high and low photon flux. (The peaks are labeled similarly to Figure 2.10.)

Analysis of Ce $N_{4,5}$-edge XANES spectra was also performed during this study. These spectra are much more complex than the Ce $M_{4,5}$-edge spectra and arise from the transitions of Ce 4d electrons into unoccupied Ce 4f states. The attenuation length of the X-rays and the escape depth of the emitted photons probe at a similar sample depth to that of the Ce 4d XPS spectra (~ 7 nm).[70] The Ce $N_{4,5}$-edge spectra are separated into two main regions; a sharp, low intensity dipole forbidden region, and a broad, high intensity dipole allowed region at higher energy.[100] A comparison of the resulting Ce $N_{4,5}$-edge spectra of samples 7-A and 8-A, along with spectra from standard materials, are presented in Figure 2.12a. In the spectrum from bulk $CeO_2$, the lower energy peaks are somewhat broad while the main, higher energy feature is located at ~ 130 eV. In the spectrum of bulk $CePO_4$, the lower energy peaks are sharper while the main, higher energy region is found at ~ 118 eV. The differences between the standard spectra reflect the differences observed when a material contains either $Ce^{4+}$ or $Ce^{3+}$ species. By examination of the first derivative of the spectra (inset in Figure 2.12a), the smaller ceria NC sample (sample 8-A) showed an increased intensity of the $Ce^{3+}$ features as compared to the larger NC sample (sample

7-A). These results validate the previous conclusion, where smaller NCs exhibited a greater degree of surface damage than their larger counterparts.

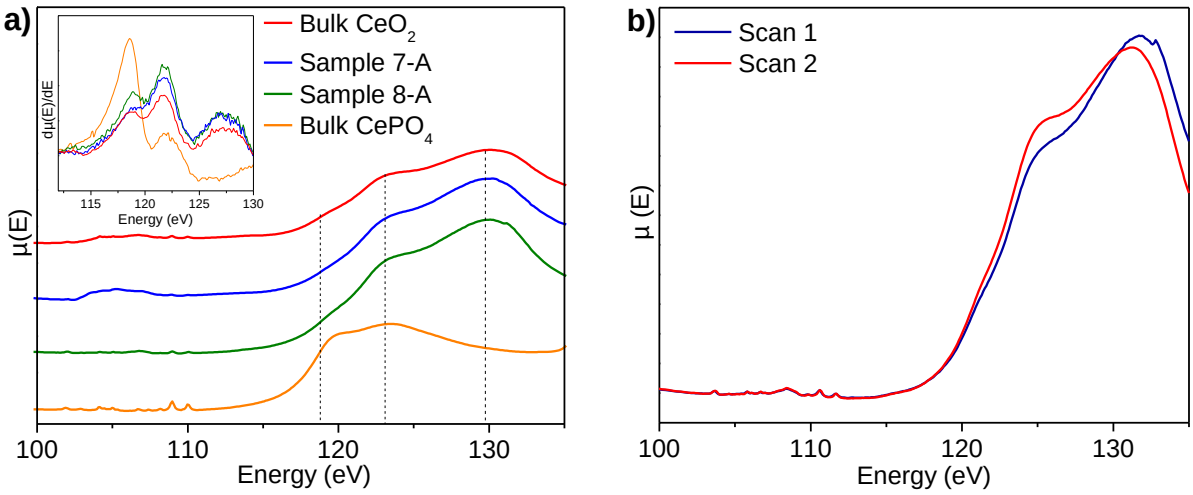


**Figure 2.12: a)** Ce $N_{4,5}$-edge XANES spectra from bulk $CeO_2$ and $CePO_4$, and ceria NC samples 7-A and 8-A. The inset illustrates the first derivative of the Ce $N_{4,5}$-edge spectra; **b)** Scan 1 and 2 of the Ce $N_{4,5}$-edge from ceria NC sample 8-A.

It is clear from the obtained results that the samples measured using XANES show a higher degree of reduction than those measured using XPS. It is now understood why researchers in the past have come to the conclusion that the [$Ce^{3+}$] on the surface of ceria NPs is related to the size of the particles. The high photon flux associated with XANES experiments performed under UHV conditions damage the sample to such a degree that any sort of electronic structure analysis would be affected, which is evident from the Ce $N_{4,5}$-edge spectra reported here. The spectra that are presented in Figure 2.12a represent multiple scans of the same spectrum which have been merged together. Each individual scan of the spectrum is slightly different than the other, due to some damage that is occurring within the sample. Figure 2.12b illustrates that sample damage can be observed after 2 sequential scans collected from sample 8-A. The intensity of the broad feature at higher energy was slightly decreased in intensity and shifted to

lower energy from scan 1 to scan 2, which is indicative of the reduction of $Ce^{4+}$ to $Ce^{3+}$ within the ceria NC sample (*c.f.* the spectra from bulk $CeO_2$ and $CePO_4$ in Figure 2.12a).

## 2.4. Conclusions

Monodisperse ceria NCs having exposed (002) surfaces with average particle sizes ranging from ~ 3 to 10 nm were successfully synthesized utilizing a hydrothermal method. The changes in the electronic structure associated with variations in synthetic conditions were analyzed using both XPS and XANES characterization techniques. It was determined, through the analysis of the Ce 3d XPS spectra collected after a single sweep, that the [$Ce^{3+}$] was independent of the individual sample conditions as the calculated values ranged from ~ 7 to < 10 % regardless of the particle size or Ce precursor. The X-ray induced reduction of $Ce^{4+}$ was also examined in this study by comparing the Ce 3d spectra collected after a single sweep with those collected after averaging 20 sweeps. Upon analysis of the Ce 3d spectra collected after 20 sweeps, it was determined that the degree of $Ce^{4+}$ reduction was also independent of the individual sample conditions, with calculated [$Ce^{3+}$] values ranging from ~ 16 to 21 %. A comparison of the more bulk sensitive Ce 4d spectra collected after 1 and 20 sweeps indicated that the X-ray damage was localized mainly to the surface of the ceria NC samples. To further confirm the obtained results, the Ce $M_{4,5}$- and $N_{4,5}$-edge XANES spectra of the NCs were collected and showed a higher degree of $Ce^{4+}$ reduction than the XPS spectra. It was shown here that the increased brightness of synchrotron radiation used to collect XANES spectra reduced the surface of the ceria NCs more rapidly than in XPS experiments.

The results from this study demonstrate that XPS is an extremely useful technique for examining the changes in the electronic structure of ceria NCs. Even though typical XPS spectra from $CeO_2$ do show some damage over time, the XPS spectra collected after a single sweep provided highly accurate results. It has been successfully established that the [$Ce^{3+}$] within the synthesized ceria NCs is not affected by changes in the synthetic methodology, but remains relatively constant regardless of the particle size or Ce precursor used. This study also demonstrated that certain experimental conditions, *i.e.* a focused X-ray beam, can be harmful to the samples under analysis. To avoid damaging these materials, it is evident that additional

precautions and constraints must be taken into account during the analytical process. These findings will be useful in developing a deeper understanding of the electronic properties of nanostructured ceria-containing compounds.

# Chapter 3

# Catalytic Performance of Ceria NCs and Au/$CeO_2$ Composites towards Benzyl Alcohol Oxidation Reactions

## 3.1. Introduction

Alcohol oxidation reactions are extremely important organic reactions, especially in the production of intermediates (typically aldehydes) in the fine chemical industry.[103] As briefly mentioned in Section 1.3.1, the need to develop new heterogeneous catalytic systems which use mild oxidative conditions, less toxic chemicals / oxidants, and produce less waste has become of significant interest in the scientific community. For example, benzaldehyde is a notable intermediate in the production of pharmaceuticals, perfumes, dyes, and agro-chemicals, and is commercially manufactured through the hydrolysis and oxidation of benzyl chloride.[104] This process leaves traces of chloride in the product, which can potentially poison any further reactions.[103] As a result, the liquid-phase oxidation of benzyl alcohol to benzaldehyde under mild aerobic conditions has gained significant attention over the past several years.[105]

Benzyl alcohol was chosen as a substrate for this study as it has been previously examined in the Scott research group.[106] This substrate serves as a model system as it can undergo a wide range of reactions, depending on the reaction conditions. For example, benzyl alcohol can be oxidized to form benzaldehyde, benzoic acid and benzyl benzoate, as illustrated in Figure 3.1. It can also undergo disproportionation to form benzaldehyde, toluene and water, dehydrated to form dibenzylether, and can self-condensate to form anthracene and stilbene.[103] Using low temperature liquid-phase oxidative conditions, only the products depicted in Figure 3.1 are those which are typically observed.[103] Generally, under the aforementioned conditions, benzaldehyde is the major oxidation product, while the acid and ester are formed as the result of over-oxidation.

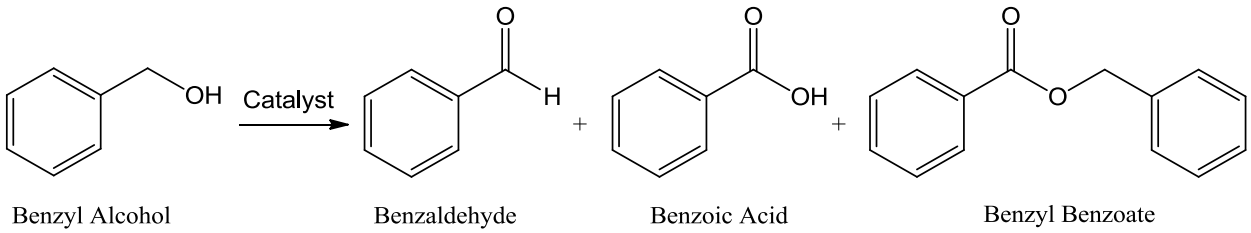


**Figure 3.1:** The catalytic oxidation of benzyl alcohol to benzaldehyde, benzoic acid, and benzyl benzoate.

Since the discovery that metal oxide supported Au NPs are extremely catalytically active towards low temperature CO oxidation reactions, researchers have searched to find other reactions for which Au NP catalysis is possible.[48,105] As discussed in detail in Section 1.3.2, Au supported ceria ($Au/CeO_2$) catalysts have been shown to catalyze many important reactions, including the oxidation of benzyl alcohol.[105] Recently, it was shown that 2 – 5 nm Au NPs supported on Sm-doped ceria (25 – 30 nm) can selectively oxidize benzyl alcohol to benzaldehyde in the presence of molecular oxygen, with conversions ranging from ~ 5 – 27 %.[105] It was demonstrated that the nature of the support played an important role in the oxidation reactions via strong metal-support interactions.[105] The purpose of this study was to investigate the role of the ceria support in different catalytic systems; bulk ceria and (002)-terminated ceria NCs.

In this chapter, the catalytic activity of a variety of different Au, $CeO_2$ and $Au/CeO_2$ systems, including supported $Au_{25}(SR)_{18}$ MPCs, are studied through the oxidation of benzyl alcohol. The structure and morphology of the various systems were characterized using thermogravimetric analysis (TGA) and TEM, while the activity of the systems was followed using $^1H$ NMR spectroscopy. Au $L_3$-edge XANES and EXAFS spectra were also collected on the Au/bulk $CeO_2$ and $Au_{25}(SR)_{18}$/bulk $CeO_2$ catalytic systems to better understand the differences between them. Through the in-depth analysis of ceria-based catalytic systems, it was found that catalysts derived from $Au_{25}(SR)_{18}$ MPCs were catalytically inactive for benzyl alcohol oxidation reactions while Au/bulk $CeO_2$ catalysts generated from $AuCl_4^-$ salts were active.

## 3.2. Experimental Methods

### 3.2.1. Materials

Cerium (III) nitrate hexahydrate (99.99%) and cerium (IV) oxide (< 5 μm, 99.9%) were purchased from Sigma-Aldrich. Oleic acid (99%), tert-butylamine (98%), polyvinylpyrrolidone (PVP; M.W. 58,000) and hydrogen tetrachloroaurate trihydrate [$HAuCl_4 \cdot 3H_2O$] (99.99%) were purchased from Alfa Aesar. Sodium borohydride powder [$NaBH_4$] was obtained from Fisher Chemical. Anhydrous potassium carbonate [$K_2CO_3$] (99.0%) was obtained from EMD Chemicals Inc. Benzyl alcohol [$C_7H_8O$] (99%) was obtained from EM Science. Deuterated chloroform [$CDCl_3$] was purchased from Cambridge Isotope Laboratories Inc. All of the previously mentioned chemicals were used as obtained, without any further purification.

### 3.2.2. Synthesis of Ceria NCs

The ceria NCs were synthesized following the procedure outlined in Section 2.2.2. The NCs were then concentrated and calcined at 500 °C for 1 – 2 hours until a yellow powder was obtained.

### 3.2.3. Synthesis of PVP-stabilized Au NPs

The Au NPs were synthesized using a previously reported procedure from the Scott group.[106] In a typical procedure, 0.25 mL of a 10 mM $HAuCl_4 \cdot 3H_2O$ solution ($2.5 \times 10^{-6}$ mol) was added to 2.0 mL of distilled $H_2O$ with stirring. 0.5 mL of a 1.39 mM PVP solution ($6.95 \times 10^{-7}$ mol) was then added and stirred at 0°C for 30 minutes in an ice-water bath. 0.25 mL of a fresh 0.1 M $NaBH_4$ solution ($2.5 \times 10^{-5}$ mol) was added, then the solution was stirred at 0°C for an additional 30 minutes, and then diluted to 5.0 mL.

### 3.2.4. Synthesis of $Au/CeO_2$

Supported $Au/CeO_2$ catalysts were prepared using a slightly modified literature procedure, using either bulk or NC $CeO_2$.[51] Typically, the desired amount of $HAuCl_4 \cdot 3H_2O$ in water was brought to pH 10 through the slow addition of 0.2 M NaOH. The desired amount of $CeO_2$ was then added to the solution, and the pH was readjusted to a value of 10. To achieve a 1 wt% Au loading on bulk $CeO_2$, 0.500 g of $CeO_2$ was added to an aqueous solution of $HAuCl_4 \cdot 3H_2O$ (1.0 mg). The solution was then vigorously stirred for $\geq$ 20 hours at room temperature. The $Au/CeO_2$ was then filtered and extensively washed with distilled water. The product was air dried, followed by calcination at 200 °C for 2 hours.

The $Au_{25}(SR)_{18}$ MPCs (SR = phenylethanethiolate) which were used during this study were prepared by A. Shivhare utilizing a previously published procedure from the Scott group.[57] Two distinct procedures were used to support the $Au_{25}(SR)_{18}$ MPCs on $CeO_2$. In the first procedure, the as-prepared $Au_{25}(SR)_{18}$ MPCs were dispersed in a solution of THF. An appropriate amount of either bulk or NC ceria powder was then stirred into the solution, and the solvent was evaporated under a constant flow of $N_2$ gas. The obtained powder was then calcined at 150 °C to remove the thiolate ligands. Alternatively, the desired amount of $Au_{25}(SR)_{18}$ MPCs were dispersed in a solution of $CH_2Cl_2$ followed by addition of the $CeO_2$ (bulk or NC), and then left for 24 hours in a sealed vial with stirring.[56] The $Au_{25}(SR)_{18}/CeO_2$ product was then calcined at temperatures ranging from 150 – 350 °C for 2 hours.

### 3.2.5. Oxidation Reactions – Optimized Conditions

The benzyl alcohol oxidation reactions were performed under similar conditions to those which have been previously reported in the Scott group.[106] In a typical procedure, the desired amount of catalyst, 51.9 mg of $K_2CO_3$ ($3.75 \times 10^{-4}$ mol), 7.5 mL of distilled water and 0.13 mL of benzyl alcohol ($1.25 \times 10^{-3}$ mol) were mixed together in a round bottom flask (with a condenser attached to minimize substrate/product loss) under vigorous stirring (1200 rpm). The reaction was then heated to 60 °C for 7 hours. Typically, the reactions were performed in an air atmosphere. When required, however, a constant flow of $O_2$ (g) was bubbled into the system.

Once the reaction was complete, the solid catalyst was removed by centrifugation and 1 mL of solution was transferred into a vial for analysis. 0.5 mL of a 0.1 M HCl solution ($5 \times 10^{-4}$ mol) and 1 mL of $CDCl_3$ were then added to the vial. To transfer the products and remaining substrate into the organic phase, the vial was rapidly shaken and mixed. The organic ($CDCl_3$) phase was then extracted and characterized using $^1H$ NMR spectroscopy to determine the relative yields / conversions and selectivities.

### 3.2.6. Characterization

TGA was conducted using a TA Q5000 thermogravimetric analyzer and high temperature platinum pans. Samples were heated from 25 °C to 120 °C at a rate of 10 °C / min, held at 120 °C for 1 hour to remove excess solvent, then further heated to 900 °C at a rate of 10 °C / min. These measurements were all performed under a constant flow of either nitrogen (25.00 mL / min) or air depending on the experiment.

A Philips CM10 electron microscope operating at 80 - 100 kV was used for TEM imaging. The samples were dispersed in toluene and drop-coated onto a carbon-coated Cu grid. To determine the average particle sizes and standard deviations, the particles were manually measured using the ImageJ program.[63]

$^1H$ NMR spectra were obtained using a Bruker 500 MHz Advance NMR spectrometer, located at the Saskatchewan Structural Sciences Centre (SSSC), and were collected after 128 scans of each spectrum. The resulting chemical shifts were referenced to the residual protons of the deuterated solvent ($CDCl_3$; singlet at 7.26 ppm).[107]

Au $L_3$-edge XANES and EXAFS spectra were collected at the CLS using the Hard X-ray Microanalysis beamline (HXMA, 06ID-1) and a Si (111) crystal monochromator. The photon flux of this beamline is $10^{12}$ photons/(s·0.1% bandwidth) at 120 keV and the resolution of the beamline is 1.2 eV at 11919 eV. The samples were prepared by spreading a thin layer of finely ground powder onto Kapton tape. Multiple layers of sample were prepared in order to increase the sample thickness and uniformity. Au $L_3$-edge spectra were collected using TFY mode and were measured by stepping the excitation energy by 0.5 eV increments through the absorption edge. A 32 element detector with a Ge filter was used to remove the direct elastic and inelastic

scatter. The spectra were internally calibrated by collecting spectra from Au foil, which has a well-known absorption energy (Au $L_3$-edge; 11919 eV).[87] The XANES spectra collected during this study were analyzed using the Athena software program, and the EXAFS spectra were analyzed and fitted using the Artemis software program.[89] During the EXAFS analysis, a Au fcc model was used to fit the first shell of Au foil, Au/bulk $CeO_2$ and $Au_{25}(SR)_{18}$/bulk $CeO_2$ catalysts. The amplitude reduction factor was determined from Au foil and fixed at 0.90 for all remaining fits while the *R*-range used was 1.85 - 3.45 Å.

# 3.3. Results and Discussion

## 3.3.1. Thermogravimetric Analysis

It has been previously shown that ceria NCs having adsorbed OLA ligands exhibit highly variable weight losses in TGA plots.[108] Lv *et al.* calculated the theoretically largest amount of densely packed OLA ligands on the surface of ceria NCs to be 41 wt%, yet their TGA measurements showed a much higher percentage (~ 75 wt% total weight loss, in air, at ~ 530 °C).[108] This indicated that some of the OLA molecules were physically blended into the chemically adsorbed layer on the surface of the NCs.[108] The analysis of IR spectra confirmed the coexistence of two different OLA species present in the ceria NC samples.[108] As the ceria NC studied here are slightly different than those in the aforementioned study, the TGA plots of several ceria NC samples were analyzed in order to determine the optimal calcination temperature, *i.e.* the temperature at which all of the organic ligands have been removed. Figure 3.2 illustrates the TGA weight loss plots for the ceria NC samples studied here.

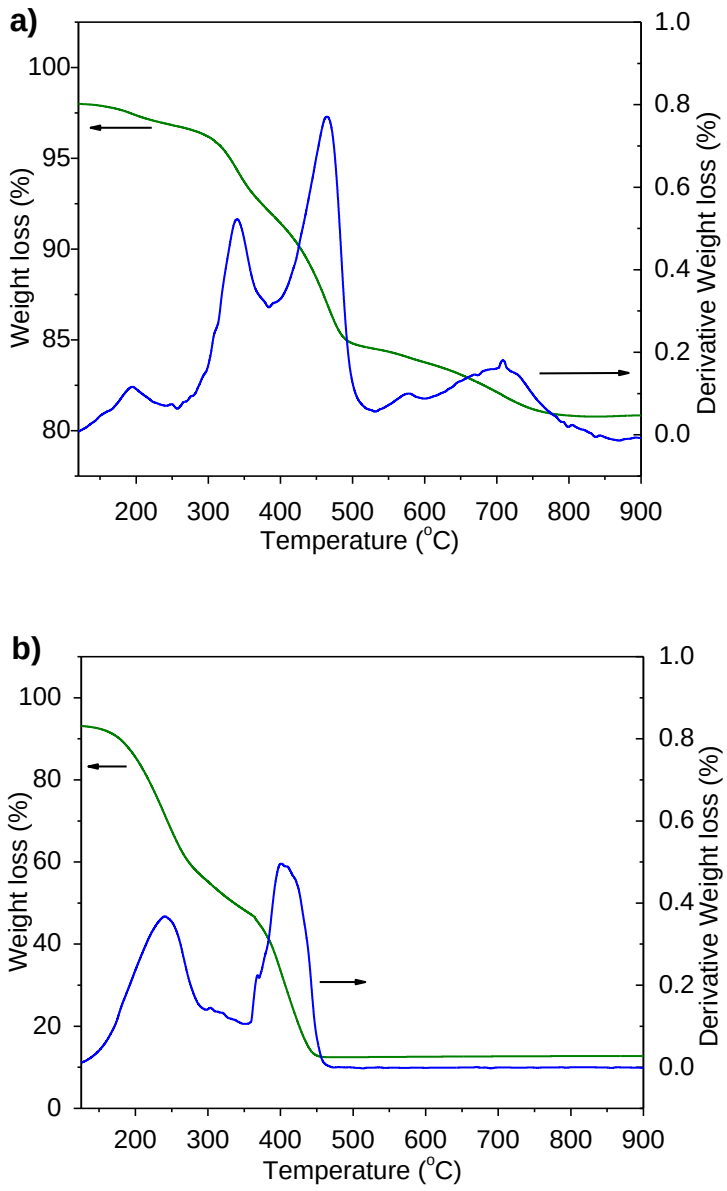


**Figure 3.2:** TGA plots from ceria NCs under a constant flow of **a)** $N_2$ gas, and **b)** air.

Four distinct weight loss features were observed when the TGA experiment was performed under a constant flow of $N_2$ gas (Figure 3.2a). It is presumed here that the feature at ~ 195 °C is related to the cerium precursor ($Ce(NO_3)_3 \cdot 6H_2O$), while the features at ~ 340 °C and 470 °C are related to the two types of OLA ligands present on the surface of the NC samples (the

boiling point of OLA is 360 °C). The final feature (~ 700 °C) can be explained through the examination of the TGA plot which was obtained using a constant flow of air, rather than $N_2$ (g) (Figure 3.2b). The feature was completely absent in this case indicating that some high temperature $O_2$ loss occurred when $N_2$ was used as a flow gas. The weight loss features in Figure 3.2b are slightly broadened and shifted from those in Figure 3.2a due to the presence of $O_2$ (g) in the air which can react with the sample. This is also apparent when one compares the total weight losses in both atmospheres; ~ 15 wt% lost under $N_2$ (g) and ~ 75 wt% lost in air. This large difference could be attributed to the fact that not all of the OLA ligands had been removed under $N_2$ (g), possibly due to polymerization of the ligands. In both cases, however, the final weight loss feature occurred at ~ 450 – 500 °C. This indicated that the ceria NC samples were thermally stable above this temperature range, and was therefore determined to be the ideal calcination temperature range.

## 3.3.2. TEM Imaging

### 3.3.2.1. Ceria NCs

The ceria NC samples were further examined through the use of TEM to determine the optimal calcination temperature. The NCs were calcined at temperatures ranging from 350 °C to 600 °C, in air, to examine how the structure of the NCs changed at different temperatures. After calcination at the various temperatures, a fine yellow powder NC product was obtained, except for the sample that was calcined at 350 °C, which was black. Figure 3.3 presents the TEM images of the ceria NCs before and after calcination at 450 °C and 500 °C.

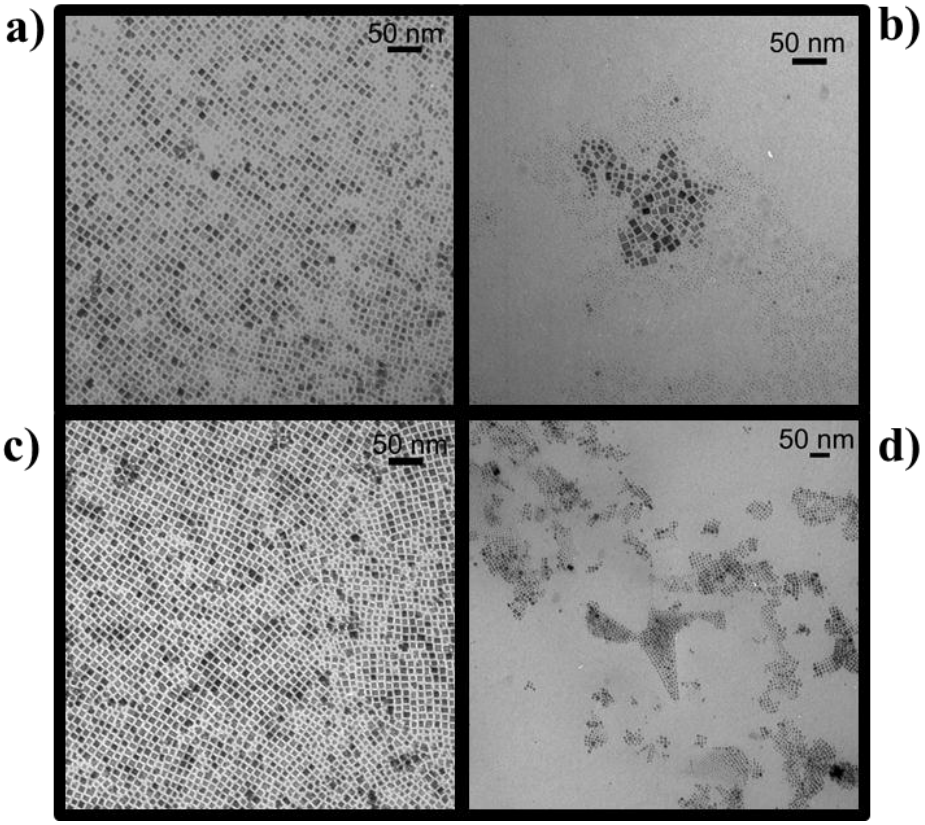


**Figure 3.3:** TEM images of **a)** ceria NCs before and **b)** after calcination at 450 °C, and **c)** ceria NCs before and **d)** after calcination at 500 °C.

Before calcination at 450 °C, the NCs had an average particle size of 6.3 ± 0.7 nm, while after calcination, the NCs exhibited a bimodal size distribution (6.4 ± 1.0 nm and 2.6 ± 0.5 nm). Similar results were obtained for NCs which were calcined at 400 °C (not shown). This effect was not observed when the calcination temperature was increased to 500 °C (and higher). The NCs did however appear to have slightly decreased in size after calcination, from 6.2 ± 0.8 nm to 5.3 ± 0.7 nm (Figure 3.3c, d). This effect has been attributed to a slight contraction of the NCs after the removal of the OLA ligands and crystallization of the ceria. These results, along with those obtained from the TGA experiments, indicated that 500 °C was the ideal calcination temperature for the ceria NCs.

### 3.3.2.2. Au NPs and Au/$CeO_2$

PVP-stabilized Au NPs were synthesized via reduction of the metal salt precursor in the presence of polymer by a $NaBH_4$ solution.[105] Figure 3.4a illustrates a typical TEM image of the synthesized Au NPs. The average size of the NPs was determined to be 2.7 ± 0.8 nm, similar to those which have been previously reported.[105]

The PVP-stabilized Au NPs were of similar size to those which have been supported on bulk $CeO_2$ utilizing the metal salt precursor under basic conditions.[51] With a Au loading of 2.7 wt%, the decoration of Au NPs (2.4 ± 0.5 nm) on the $CeO_2$ support is clearly evident from Figure 3.4b. Upon decreasing the Au loading to 1.8 wt%, the Au NPs appeared to be slightly smaller in size (2.1 ± 0.5 nm) (Figure 3.4c). TEM images were also taken of bulk $CeO_2$ as a control experiment (not shown) to verify that the presumed Au decoration was in fact Au, and not an artifact of the $CeO_2$. No artifacts were present on the bulk $CeO_2$ used.

A TEM micrograph from the $Au_{25}(SR)_{18}$ MPCs / NPs (3.0 ± 0.5 nm) supported on bulk $CeO_2$ is illustrated in Figure 3.4d. This catalytic system was prepared utilizing a literature procedure and a calcination temperature of 200 °C.[56] The size similarity of all of the Au NPs in the different environments allow for an effective comparative study of how the environment affects the activity of Au towards benzyl alcohol oxidation reactions. It should be noted, however, that due to the poor contrast between Au and $CeO_2$, as well as the resolution limit of the TEM used (*ca.* 0.5 nm), the measured particle sizes might be an overestimation of the true value. On the same note, due to the size similarity of the Au NPs and the ceria NCs, it was nearly impossible to distinguish between the two by conventional BF TEM in the Au/$CeO_2$ NC catalytic system (Figure 3.4e).

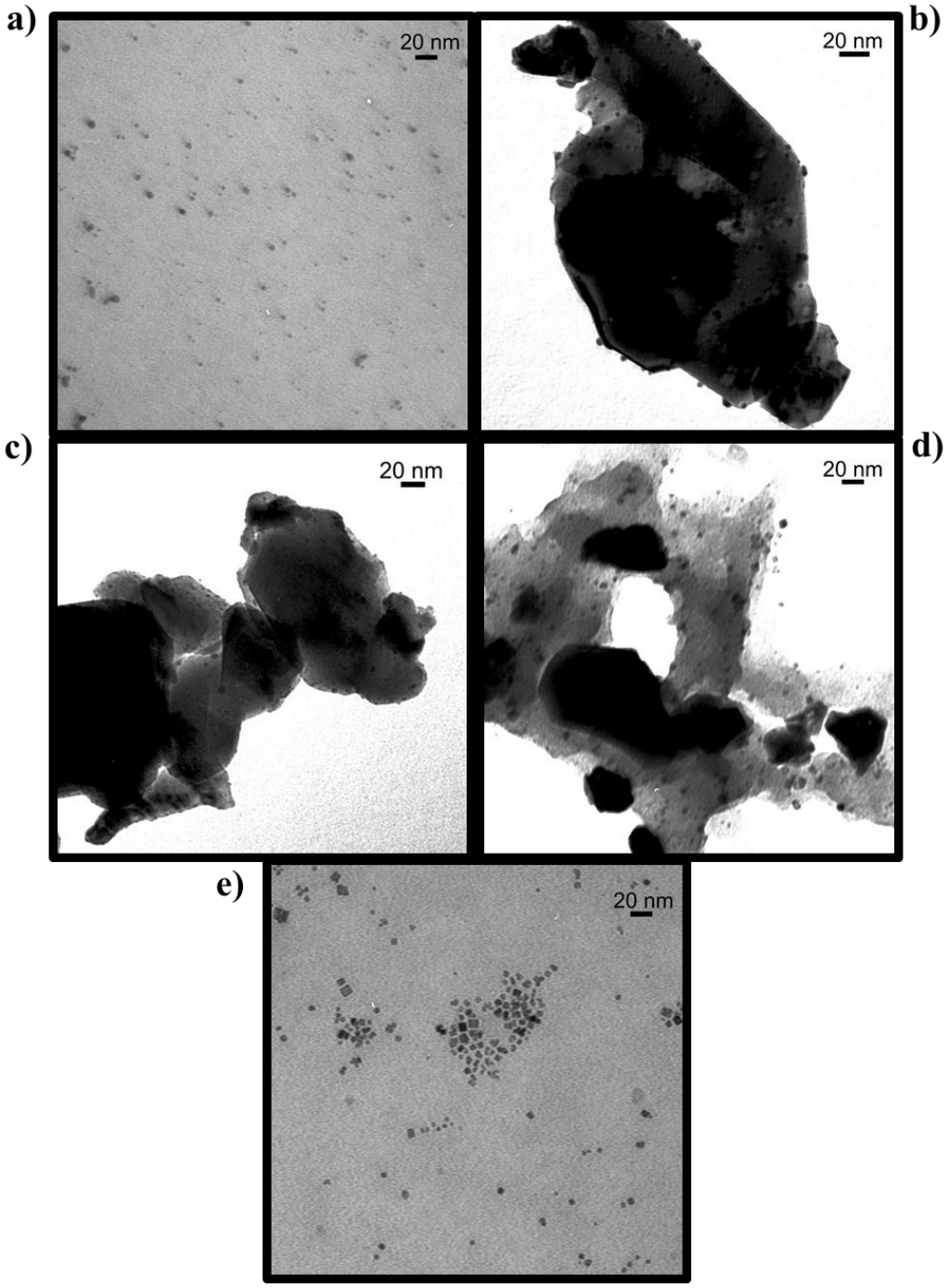


**Figure 3.4:** TEM images of **a)** PVP-stabilized Au NPs, **b)** Au/bulk $CeO_2$ (2.7 wt% Au loading), **c)** Au/bulk $CeO_2$ (1.8 wt% Au loading), **d)** $Au_{25}(SR)_{18}$/bulk $CeO_2$ (0.6 wt% Au loading), and **e)** Au/$CeO_2$ NCs (3.6 wt% Au loading).

### 3.3.3. Benzyl Alcohol Oxidation Reactions

The catalytic activity of ceria NCs, Au NPs and $Au/CeO_2$ catalysts has been studied in this work through the oxidation of benzyl alcohol. In order to determine how far a reaction had progressed, a $^1H$ NMR spectrum was obtained of the final reaction mixture. The resulting spectrum indicated whether or not any significant substrate conversion had occurred, as the three expected products have very distinct signals. The percentage of benzyl alcohol conversion indicates how much of the substrate has been successfully oxidized, while the turnover frequency (TOF) of the reaction defines the activity of the catalyst. The average TOF is calculated as follows:

$$\text{TOF} = \left[\frac{\text{mol product (benzaldehyde+benzoic acid+benzyl benzoate)}}{\text{mol Au (active sites)}}\right] \div \text{rxn time (h)} \qquad (3.1)$$

This equation assumes that all of the Au sites are active sites and that the reactions proceed linearly with time with respect to the formed products. These assumptions can induce some error in the calculated values. Figure 3.5 illustrates the differences between the $^1H$ NMR spectra of benzyl alcohol, the substrate, and the desired major product, benzaldehyde. The main indication of the formation of benzaldehyde is the singlet located at 10 ppm, representing the aldehydic proton ($H_F$).

This section primarily follows a chronological timeline. The first sub-section outlines the reactions which were performed using unsupported ceria catalysts, the second describes those which were performed using Au NP catalysts, and the third summarizes the oxidation reactions performed using $Au/CeO_2$ catalysts.

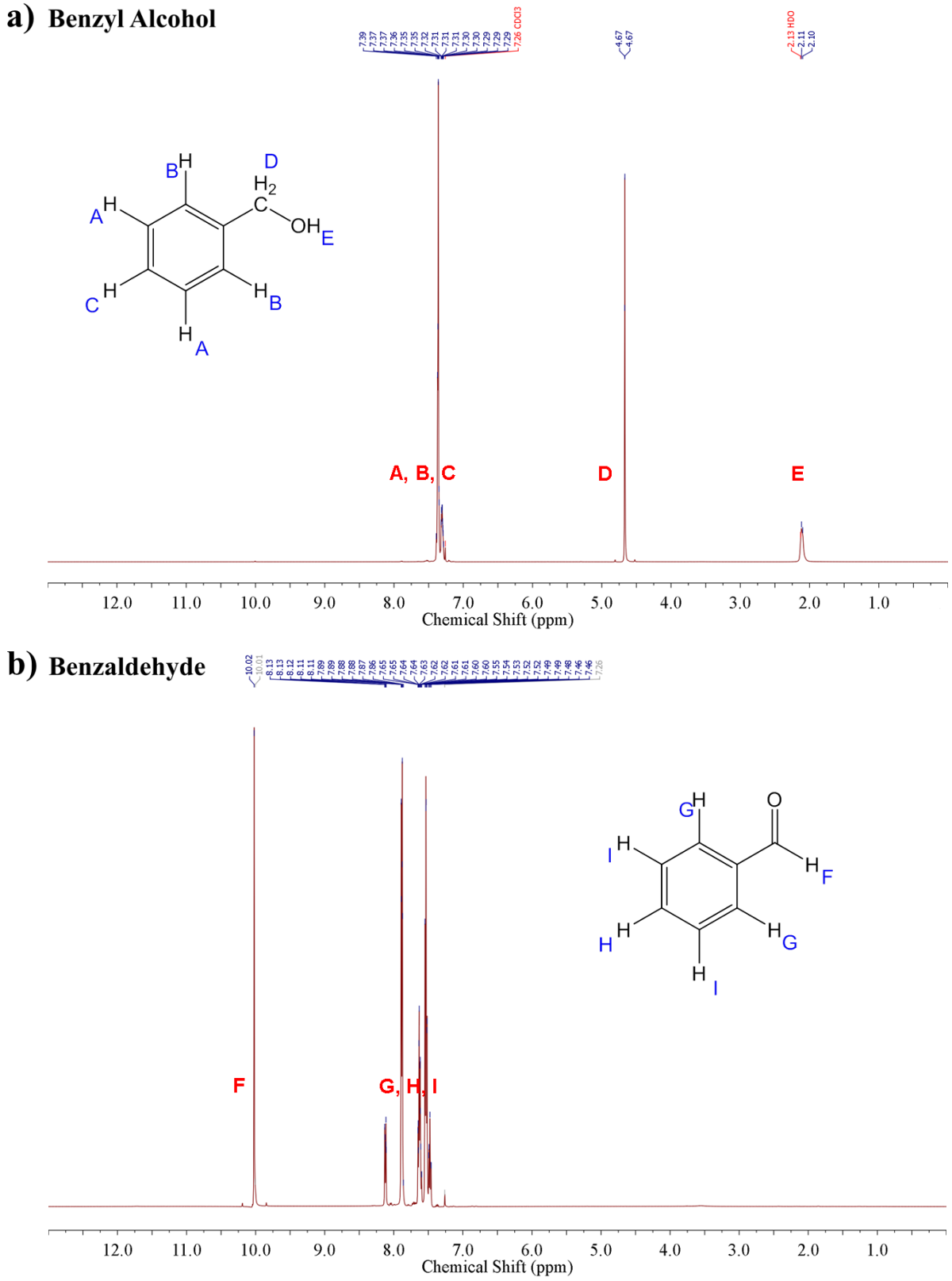


**Figure 3.5:** Labeled $^{1}$H NMR standard spectra from **a)** benzyl alcohol and **b)** benzaldehyde.

### 3.3.3.1. Ceria Catalysts

The first reactions that were tested utilized the as-synthesized and calcined ceria NCs (at 500 °C) and bulk ceria in order to see if there were any stoichiometric reactions occurring between the ceria and the substrate. All of the reactions had the same basic set up: 5 – 10 mL solvent, stoichiometric amounts of substrate and ceria catalyst, excess oxidant (when used), and heated to (typically) 60 °C for a given period of time. A variety of different reaction conditions were tested. Table 3.1 details all of the experimental parameters used. However, after thorough analysis of the resulting $^1$H NMR spectra, it was clear that no products had formed in any of the attempts to oxidize benzyl alcohol. This indicated that under typical conditions, there were no stoichiometric or catalytic reactions occurring between the ceria NCs (or bulk ceria) and the substrate. Knowing this, subsequent experiments were conducted to see if the addition of Au NPs would be able to successfully oxidize benzyl alcohol.

**Table 3.1:** Benzyl alcohol oxidation reaction conditions using a variety of ceria catalysts. [a]

| Entry [b] | Ceria Catalyst | Size (nm) | Substrate / catalyst [c] | Oxidant | Solvent | Temp. (°C) | Time (h) |
|---|---|---|---|---|---|---|---|
| 1 | Bulk $CeO_2$ | - | 10:1 | - | $H_2O$ | 80 | 7 |
| 2 | NCs – before calc. | 6.8 ± 0.8 | - | $O_2$ (g) | - [d] | 60 | 7 |
| 3 | Calcined NCs | 7.2 ± 0.8 | 6.6:1 | - | $H_2O$ | 60 | 5.5 |
| 4 | Calcined NCs | 5.5 ± 0.7 | 21:1 | - | $H_2O$ | 60 | 7 |
| 5 | Calcined NCs | 6.2 ± 0.8 | 6.9:1 | $H_2O_2$ | $H_2O$ | 60 | 5.5 |
| 6 | Calcined NCs | 5.2 ± 0.7 | 9.7:1 | $^t$BuOOH | $H_2O$ | 60 | 5.5 |
| 7 | Bulk $CeO_2$ | - | 8.2:1 | $H_2O_2$ | THF | 60 | 4 |
| 8 | NCs – before calc. | 6.9 ± 0.7 | - | $O_2$ (g) | THF | 60 | 6 |
| 9 | Calcined NCs | 8.0 ± 1.0 | 6.5:1 | $O_2$ (g) | THF | 60 | 6 |
| 10 | Calcined NCs | 5.2 ± 0.7 | 5.3:1 | $H_2O_2$ | THF | 60 | 6 |
| 11 | Calcined NCs | 5.5 ± 0.8 | 5.3:1 | $^t$BuOOH | THF | 60 | 6 |

*a.* Reactions were performed in the presence of 5 – 10 mL of solvent and excess oxidant

*b.* Dashed line separates the reactions which used $H_2O$ and THF as solvent

*c.* Substrate/catalyst molar ratios were calculated assuming all of the ceria sites are active

*d.* ~ 5 mL of benzyl alcohol was used as the 'solvent'

### 3.3.3.2. Au NP Catalysts

As previously mentioned, benzyl alcohol oxidation reactions have been performed successfully in the Scott research group, along with many others research groups.[103-106] Au, Pd, and bimetallic AuPd NP catalysts have been shown to oxidize benzyl alcohol under mild aqueous (basic) conditions.[106] As the aforementioned conditions in Section 3.3.3.1 were not suitable to catalyze this reaction, the conditions established by Hou *et al.* were used.[106] Table 3.2 outlines the benzyl alcohol oxidation reaction conditions for a variety of Au NP catalysts.

**Table 3.2:** Benzyl alcohol oxidation reaction conditions and turnover frequencies using a variety of Au NP catalysts. [a]

| Entry [b] | Substrate / Catalyst [c] | Oxidant | Temp. (°C) | Conversion [e] (%) | TOF [e] ($h^{-1}$) | Selectivity (%) Aldehyde | Acid + Ester |
|---|---|---|---|---|---|---|---|
| 1 | 500:1 | - | RT | 17 | 12.1 | 25 | 75 |
| 2 | 500:1 | - | 60 | 43 | 30.7 | 24 | 76 |
| 3 | 500:1 | $O_2$ (g) | 60 | 31 | 22.1 | 27 | 73 |
| 4 | 1500:1 | - | 60 | 10 | 21.4 | 47 | 53 |
| 5 | 1800:1 | - | 60 | 5 | 21.4 | 58 | 42 |
| [106] [d] | 500:1 | - | RT | 10 | 8.6 | 52.8 | 47.2 |
| [106] [d] | 500:1 | $O_2$ (g) | RT | 5 | 3.9 | 100 | 0 |
| [106] [d] | 500:1 | $O_2$ (g) | 85 | 17 | 14.3 | 97.3 | 2.7 |

*a.* Reactions were performed in $H_2O$ over 7 hours

*b.* Dashed line separates the literature reaction conditions. Benzaldehyde and benzyl benzoate were the only products

*c.* Substrate/catalyst molar ratios were calculated assuming all of the Au sites are active

*d.* Literature reaction conditions and results using Au NP catalysts[106]

*e.* Conversion error: ± 2 %; TOF error: ± 4.4 $h^{-1}$

The percentage of the substrate which had oxidized (the relative yield, or the conversion) was determined utilizing the integration of the respective product peaks in the $^1$H NMR spectra, and the TOF of the reactions was calculated using equation 3.1. Figure 3.6 depicts a typical $^1$H NMR

spectrum of the products obtained during a reaction. From the peak integrations, it is clear that benzaldehyde and benzoic acid are the major products, while benzyl benzoate is a minor product. Due to the fact that the most predominant peaks associated with benzoic acid (~ 8.1 ppm) slightly overlap the peaks associated with benzyl benzoate, separation of the individual products was difficult. For this reason, these products were grouped together in the calculation of relative product selectivity. To determine the amount of error associated with this method of analysis, several oxidation reactions were performed under the exact same conditions. It was determined that the calculated benzyl alcohol conversion percentage was within 2 %, and the TOF was within 4.4 $h^{-1}$.

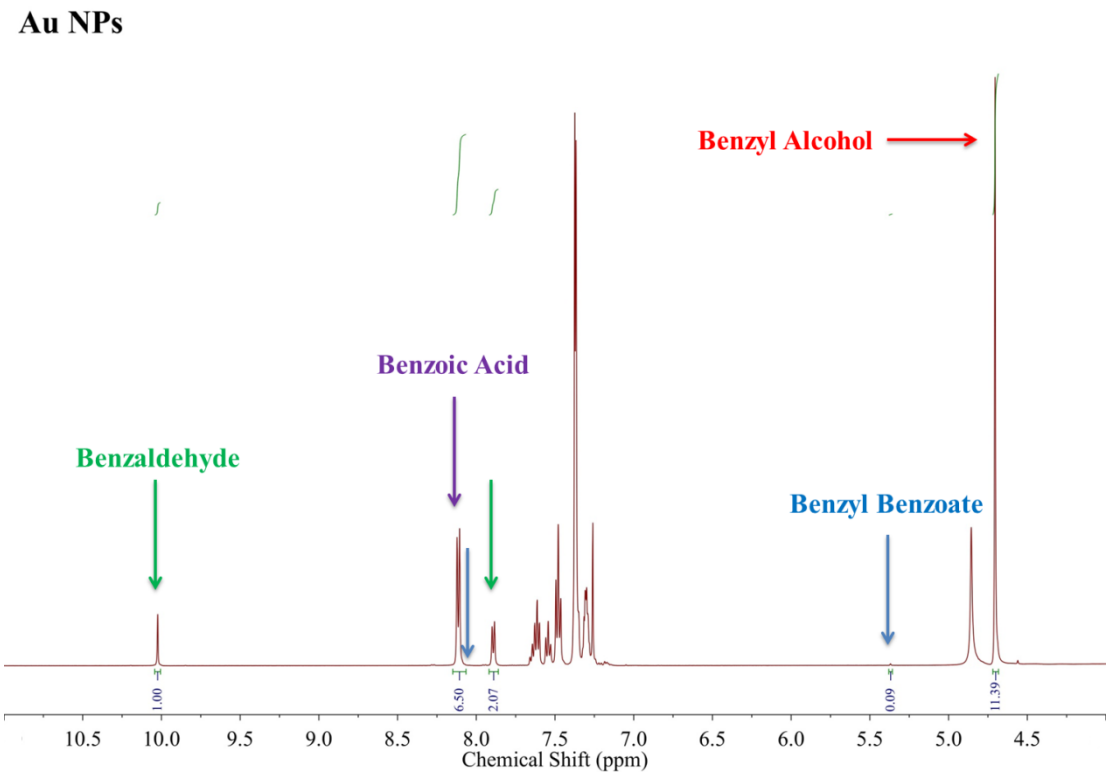


**Figure 3.6:** $^{1}$H NMR spectrum from the obtained products of a benzyl alcohol oxidation reaction using a Au NP catalyst, (Entry 2, Table 3.2); the integrations and major product peaks are labelled.

From Table 3.2, it is clear that the previously published reaction conditions were ideal conditions to oxidize benzyl alcohol.[106] The obtained conversions and TOFs are slightly higher than those previously reported, with the selectivities being slightly different as well. These slight differences can be accounted for by the fact that not all researchers perform experiments in the exact same way; there may be minor differences in how the reactions were set-up, depending on the available instrumentation at the time. However, it can be noted that in the reactions performed here and in the literature, the conversions and TOFs increased with increasing reaction temperature demonstrating an increase in the overall catalytic activity of the Au NPs.[105] It should also be noted that with increasing substrate to catalyst ratio, the benzyl alcohol conversion decreased while the selectivity towards benzaldehyde increased. It was previously found that the solubility of oxygen in the aqueous reaction mixture was a rate-limiting factor and, therefore, could be the cause of this trend.[106]

### 3.3.3.3. Au/$CeO_2$ Catalysts

As $Au_{25}(SR)_{18}$ MPCs were readily available in the Scott lab (synthesized by A. Shivhare), these MPCs were the first Au particles to be supported on ceria (NC and bulk).[57] Initially, the first procedure detailed in Section 3.2.4 was used to prepare the supported catalysts while the oxidation reactions were performed using similar conditions as the unsupported ceria catalysts (Section 3.3.3.1). THF was originally chosen as a solvent for the reactions due to the fact that the $Au_{25}(SR)_{18}/CeO_2$ samples could be readily dispersed in solution. It was thought that this would greatly enhance their ability to catalyze the reaction as a pseudo-homogenous catalyst. Unfortunately, this was not the case. No catalytic activity was observed for the $Au_{25}(SR)_{18}/CeO_2$ catalysts after reaction times of 4 and 8 hours, even in the presence of excess oxidant (Table 3.3). Once this was determined, it was clear that new reaction conditions were required in order to successfully oxidize benzyl alcohol with the $Au_{25}(SR)_{18}/CeO_2$ catalysts.

**Table 3.3:** Benzyl alcohol oxidation reaction conditions using a variety of $Au_{25}(SR)_{18}/CeO_2$ catalysts. [a]

| Entry | Catalyst | NC Size (nm) | wt% $Au_{25}(SR)_{18}$ | Substrate / catalyst [b] | Oxidant | Time (h) |
|---|---|---|---|---|---|---|
| 1 | $Au_{25}(SR)_{18}/CeO_2$ NC | 6.5 ± 1.0 | 1.0 | 789:1 | $O_2$ (g) | 4 |
| 2 | $Au_{25}(SR)_{18}/CeO_2$ NC | 6.5 ± 1.0 | 1.0 | 817:1 | $H_2O_2$ | 4 |
| 3 | $Au_{25}(SR)_{18}/CeO_2$ NC | 5.2 ± 0.8 | 0.8 | 1377:1 | $H_2O_2$ | 4 |
| 4 | $Au_{25}(SR)_{18}$/bulk $CeO_2$ | - | 1.0 | 873:1 | $H_2O_2$ | 4 |
| 5 | $Au_{25}(SR)_{18}$/bulk $CeO_2$ | - | 1.0 | 915:1 | $H_2O_2$ | 4 |
| 6 | $Au_{25}(SR)_{18}$/bulk $CeO_2$ | - | 1.0 | 920:1 | $H_2O_2$ | 8 |
| 7 | $Au_{25}(SR)_{18}$/bulk $CeO_2$ | - | 1.0 | 885:1 | $H_2O_2$ | 8 |

*a.* Reactions were performed in the presence of 10 mL of THF (solvent), under an excess of oxidant, and at 60 °C

*b.* Substrate/catalyst molar ratios were calculated assuming all of the $Au_{25}(SR)_{18}$ sites are active

As the initially tested conditions did not produce any positive results for the $Au_{25}(SR)_{18}/CeO_2$ catalysts, the well-established conditions which were used in the Au NP systems were further examined. It was clear that the $Au_{25}(SR)_{18}/CeO_2$ system was less active than expected, so another $Au/CeO_2$ system was studied. Utilizing a $HAuCl_4$ salt, Au NPs were synthesized on bulk $CeO_2$ (see Figure 3.3b, c).[51] The catalytic activity of the Au/bulk $CeO_2$ catalyst towards the oxidation of benzyl alcohol was measured using $^1H$ NMR spectroscopy, and the formation of the three expected products was observed. The reaction conditions, e.g. the reaction temperature and time, were varied in order to determine the conditions which would maximize the overall activity (see Table 3.4). Interestingly, it was found that with increasing reaction temperature, from 60 – 80 °C, the conversions and TOFs were not significantly affected. Yet, when the temperature was increased to 90 °C, the TOF decreased from 20.6 $h^{-1}$ (at 80 °C) to 11.3 $h^{-1}$. This decrease in activity could be related to the fact that the reaction was close to the boiling point of the solvent and not all of the reaction mixture re-condensed into the flask. When the reaction time was increased from 7 to 16 hours, the conversion of benzyl alcohol nearly doubled, but the TOF decreased significantly from 36.3 $h^{-1}$ to 24.5 $h^{-1}$, indicating that some deactivation occured. To

examine if the high temperature calcination treatment of the Au/bulk $CeO_2$ catalyst was affecting its ability to oxidize the substrate, various calcination temperatures were tested (100, 200, and 300 °C). After all three temperature treatments, the benzyl alcohol conversion remained relatively constant (within error), while the TOFs were a different matter (entries 7 – 9, Table 3.4). It appeared that the activity fluctuated significantly over this temperature range. However, it should be noted that the substrate to catalyst ratios used in the reactions were not identical and, therefore, cannot be perfectly compared. That being said, when comparing the reactions performed using calcination temperatures of 100 and 300 °C, it was evident that the TOFs were also not particularly affected by the change in calcination temperature. This finding led to the query of how the substrate to catalyst ratio affected the catalytic activity of the Au/bulk $CeO_2$ catalytic system.

**Table 3.4:** Benzyl alcohol oxidation reaction conditions and turnover frequencies using Au/bulk $CeO_2$ catalysts at varying reaction temperatures, times, and calcination temperatures. [a]

| Entry [b] | Calc. Temp. (°C) | Substrate / Catalyst [c] | Temp. (°C) | Time (h) | Conversion [d] (%) | TOF [d] ($h^{-1}$) | Selectivity (%) Aldehyde | Selectivity (%) Acid + Ester |
|---|---|---|---|---|---|---|---|---|
| 1 | 200 | 428:1 | 60 | 7 | 25 | 15.3 | 20 | 80 |
| 2 | 200 | 420:1 | 70 | 7 | 24 | 14.4 | 22 | 78 |
| 3 | 200 | 498:1 | 80 | 7 | 29 | 20.6 | 21 | 79 |
| 4 | 200 | 496:1 | 90 | 7 | 16 | 11.3 | 36 | 64 |
| 5 | 200 | 940:1 | 60 | 7 | 27 | 36.3 | 24 | 76 |
| 6 | 200 | 852:1 | 60 | 16 | 46 | 24.5 | 15 | 85 |
| 7 | 100 | 768:1 | 60 | 7 | 25 | 27.4 | 23 | 77 |
| 8 | 200 | 563:1 | 60 | 7 | 22 | 17.7 | 29 | 71 |
| 9 | 300 | 747:1 | 60 | 7 | 24 | 25.6 | 28 | 72 |

*a.* Reactions were performed in air using 7.5 mL $H_2O$ as a solvent

*b.* Dashed lines separate the various conditions which were varied; reaction temperature, time, and calcination temperature

*c.* Substrate/catalyst molar ratios were calculated assuming all of the Au sites are active

- Entries 1 – 6: 2.7 wt% Au loading; Entries 7 – 9: 1.8 wt% Au loading

*d.* Conversion error: ± 2 %; TOF error: ± 4.4 $h^{-1}$

The catalytic activity of the Au/bulk $CeO_2$ catalyst was measured for an assortment of benzyl alcohol oxidation reactions using different substrate to catalyst ratios. Typically, the higher the ratio (*i.e.* the lower the amount of catalyst used in the reaction) the lower the conversion. Entries 1 – 6 in Table 3.5 outline the various oxidation reactions that were performed in air. It can be seen that at substrate to catalyst ratios of ~ 440:1 – 1500:1 there is little change in the conversion of benzyl alcohol. Above that, the conversion starts to decrease. It can also be noted that on average, the TOF and selectivity towards benzaldehyde increased with increasing amount of substrate. These results indicated that the reactions might be mass-transport limited with respect to the presence of $O_2$ (g) at lower substrate to catalyst ratios. Under these conditions, $O_2$ (g) is the limiting reactant in the liquid phase, which decreases the observed catalytic activity.[106]

It has been previously shown that AuPd bimetallic NP catalysts exhibit similar limitations under these reaction conditions.[106] It was suggested that such limitations are almost unavoidable when using NP catalysts as they tend to be quite unstable under kinetically-limiting conditions.[106] To confirm this hypothesis, similar reactions were performed under a constant flow of $O_2$ (g) (entries 7 – 12, Table 3.5). It can be immediately seen that the addition of $O_2$ (g) greatly improves the percentage of benzyl alcohol conversion, from 27 % to 100 % when the substrate to catalyst ratio is ~ 440:1. Figure 3.7 illustrates the observed conversion differences between the reactions performed in air and in $O_2$ (g). As previously stated, the conversion remains relatively constant, when the reaction is performed in air, until tapering off above a ratio of ~ 1500:1. Conversely, under $O_2$ (g), the decrease in the conversion with increasing ratio is nearly linear ($R^2$ = 0.97) (see Figure 3.7). Analogously with the reactions performed in air, on average, the selectivity towards benzaldehyde increased with increasing substrate concentration when performed in $O_2$ (g). It is proposed here that this relationship is due to the reactivity of benzaldehyde in solution. Once formed, the aldehyde is free to further oxidize to benzoic acid (or benzyl benzoate) if the catalyst is sufficiently active. At higher substrate to catalyst ratios, there is a lower probability of benzaldehyde reacting further.

**Table 3.5:** Benzyl alcohol oxidation reaction conditions and turnover frequencies using Au/bulk $CeO_2$ catalysts (2.7 wt% Au loading) at varying substrate to catalyst ratios in both air and $O_2$ (g) atmospheres. [a]

| Entry [b] | Substrate / Catalyst [c] | Oxidant | Conversion [d] (%) | TOF [d] ($h^{-1}$) | Selectivity (%) Aldehyde | Acid + Ester |
|---|---|---|---|---|---|---|
| 1 | 438:1 | - | 27 | 16.9 | 16 | 84 |
| 2 | 940:1 | - | 27 | 36.3 | 24 | 76 |
| 3 | 1495:1 | - | 28 | 59.8 | 27 | 73 |
| 4 | 1788:1 | - | 23 | 58.7 | 36 | 64 |
| 5 | 1824:1 | - | 18 | 46.9 | 43 | 57 |
| 6 | 7544:1 | - | 8 | 86.2 | 63 | 37 |
| 7 | 445:1 | $O_2$ (g) | 100 | 63.5 | 0 | 100 [e] |
| 8 | 472:1 | $O_2$ (g) | 100 | 67.5 | 0 | 100 [e] |
| 9 | 829:1 | $O_2$ (g) | 68 | 80.5 | 6 | 94 |
| 10 | 1216:1 | $O_2$ (g) | 33 | 57.3 | 25 | 75 |
| 11 | 1471:1 | $O_2$ (g) | 23 | 48.3 | 10 | 90 |
| 12 | 1900:1 | $O_2$ (g) | 6 | 16.3 | 34 | 66 |

*a.* Reactions were performed using 7.5 mL $H_2O$ as a solvent at 60 °C for 7 hours

*b.* Dashed line separates the reactions which were performed in air and in $O_2$ (g)

*c.* Substrate/catalyst molar ratios were calculated assuming all of the Au sites are active

*d.* Conversion error: ± 2 %; TOF error: ± 4.4 $h^{-1}$

*e.* Benzoic acid was the only product

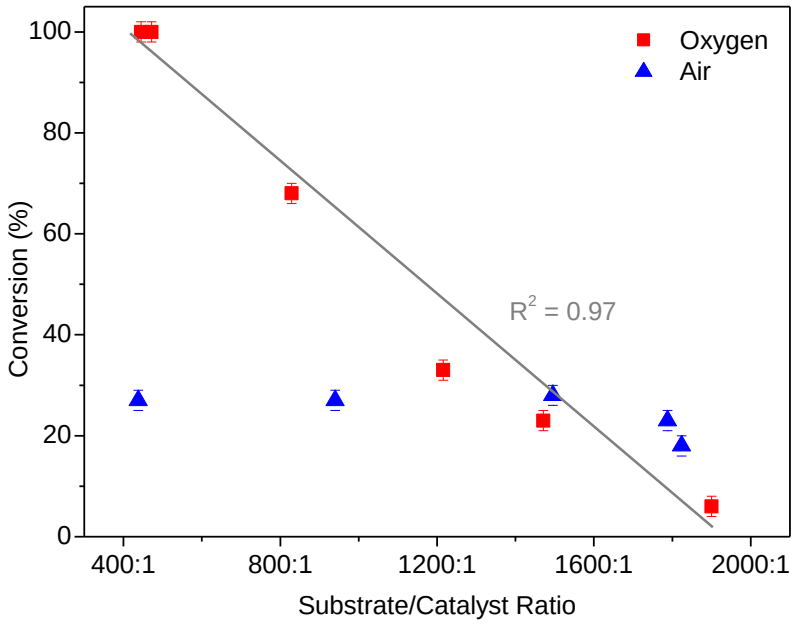


**Figure 3.7:** The percentage of benzyl alcohol conversion, in both air and $O_2$ (g) atmospheres, for the Au/bulk $CeO_2$ catalysts (2.7 wt% Au loading) at various substrate to catalyst ratios. The line of best fit is linear (y = -0.0685x + 127.35) for the reactions performed under $O_2$ (g).

In performing the oxidation reactions involving Au/bulk $CeO_2$ catalysts, several important conclusions can be made. First, increasing the reaction temperature does not overly affect the overall catalytic activity of the supported catalyst, but deactivation occurred with increasing reaction time. Secondly, increasing the calcination temperature of the catalyst does not appear to affect the overall activity. This could indicate that the supported Au NPs are not sintering significantly with increased calcination temperature. Most importantly, below a substrate to catalyst molar ratio of ~ 1500:1, mass-transport limitations exist when $O_2$ (g) is not supplied into the liquid phase fast enough. Using these results, testing the performance of other Au/$CeO_2$ catalysts could be performed more efficiently.

Utilizing these ideal reaction conditions, the catalytic activity of Au/$CeO_2$ NC and new $Au_{25}(SR)_{18}$/bulk $CeO_2$ catalysts was measured. The Au/$CeO_2$ NC catalysts were prepared in the same fashion as the Au/bulk $CeO_2$ catalysts, using a Au(III) salt as a precursor.[51] The new $Au_{25}(SR)_{18}$/bulk $CeO_2$ catalysts were prepared using the second procedure defined in Section 3.2.4, which was based on a literature procedure.[56] Table 3.6 outlines the conditions for the various catalytic reactions tested here. In the case of the Au/$CeO_2$ NC catalysts, comparable trends were observed from the Au/bulk $CeO_2$ catalysts. Under similar conditions, the $Au_{25}(SR)_{18}$/bulk $CeO_2$ catalysts, on the other hand, did not show any appreciable catalytic activity. Various other reactions were performed to determine if the calcination temperature, the substrate to catalyst ratio, and the atmosphere (air vs. $O_2$) were attributing factors in this lack of activity. Unfortunately, the $Au_{25}(SR)_{18}$/bulk $CeO_2$ catalysts were not active towards the oxidation of benzyl alcohol under any of the conditions tested here. This was surprising, as the literature has previously described these MPCs to be extremely successful catalysts for CO oxidation and nitrophenol reduction, and in both cases, their activation was reported to be a simple task.[56,109] It seems, however, that this is not the case for benzyl alcohol oxidation. It is postulated here that at these experimental calcination temperatures, the thiolate ligands, that initially stabilized the Au MPCs, may not have been completely removed from the system and were potentially poisoning their catalytic capabilities. XANES and EXAFS experiments were performed to compare the two catalytic systems ($Au_{25}(SR)_{18}$/bulk $CeO_2$ and Au/bulk $CeO_2$) to see if thiolate poisoning and / or Au oxidation was problematic in the $Au_{25}(SR)_{18}$/bulk $CeO_2$ systems, and to attempt to better understand the nature of the catalytic differences. This is further explored in Section 3.3.4.

**Table 3.6:** Benzyl alcohol oxidation reaction conditions and turnover frequencies using a variety of $Au/CeO_2$ NC and $Au_{25}(SR)_{18}$/bulk $CeO_2$ catalysts. [a]

| Entry [b] | Catalyst | NC size (nm) | wt% Au | Calc. Temp. (°C) | Substrate / Catalyst [c] | Conversion [d] (%) | TOF [d] ($h^{-1}$) | Selectivity [e] (%) | |
|---|---|---|---|---|---|---|---|---|---|
| | | | | | | | | -H | -COOH |
| 1 | $Au/CeO_2$ NC | 5.3 ± 0.7 | 3.6 | 200 | 552:1 | 22% | 17.3 | 21 | 79 |
| 2 | | 7.4 ± 0.8 | 9.7 | 200 | 1410:1 | 29% | 58.4 | 27 | 73 |
| 3 | | 7.2 ± 1.3 | 1.1 | 200 | 3588:1 | 9% | 46.1 | 46 | 54 |
| 4 [f] | | 5.9 ± 0.6 | 1.1 | 200 | 6217:1 | 3% | 26.6 | - | - |
| 5 | | 5.9 ± 1.0 | 1.6 | 200 | 13989:1 | 2% | 40.0 | - | - |
| 6 | $Au_{25}(SR)_{18}$/ bulk $CeO_2$ | - | 0.6 | 150 | 926:1 | 2% | 2.6 | - | - |
| 7 | | - | 0.6 | 150 | 1599:1 | 2% | 4.6 | - | - |
| 8 [f] | | - | 0.6 | 200 | 2340:1 | 2% | 6.7 | - | - |
| 9 [f] | | - | 2.8 | 350 | 1205:1 | 1% | 1.7 | - | - |
| 10 | | - | 2.8 | 350 | 1274:1 | 2% | 3.6 | - | - |

*a.* All reactions were performed using 7.5 mL $H_2O$ as a solvent at 60 °C for 7 hours

*b.* Dashed line separates the two catalytic systems

*c.* Substrate/catalyst molar ratios were calculated assuming all of the Au sites are active

*d.* Conversion error: ± 2 %; TOF error: ± 4.4 $h^{-1}$

*e.* –H refers to benzaldehyde; –COOH refers to benzoic acid + benzyl benzoate

*f.* Reactions performed under a constant flow of $O_2$ (g)

Although the final attempts to catalyze the oxidation of benzyl alcohol with $Au_{25}(SR)_{18}$/bulk $CeO_2$ catalysts did not succeed, invaluable information has been gained from the experiments. Figure 3.8 illustrates a comparison between the conversion percentages and TOFs of all of the catalytic systems described in this chapter versus the various substrate to catalyst ratios studied. In general, the supported catalysts, excluding the $Au_{25}(SR)_{18}/CeO_2$ systems, were much more catalytically active than the unsupported Au NPs. This can clearly be seen in the comparison of the TOFs, where the supported catalysts show TOFs almost double that of the unsupported Au NPs. This proves that the addition of ceria into the system significantly enhances the overall catalytic activity.

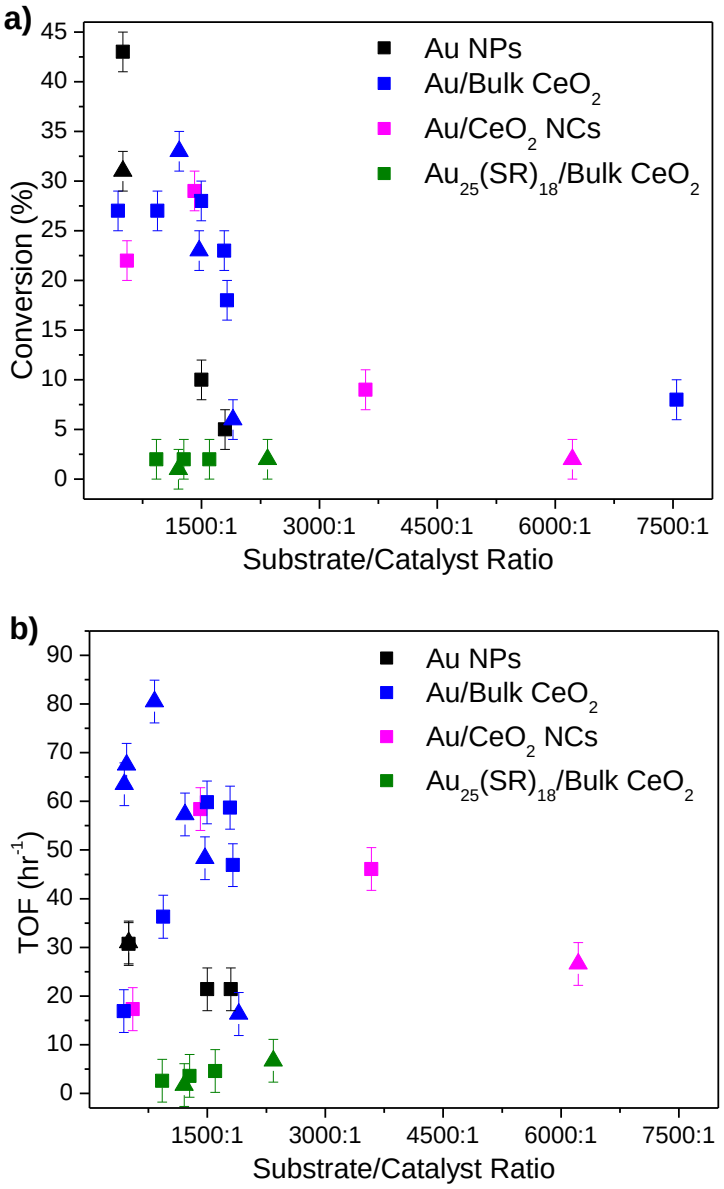


**Figure 3.8: a)** Conversion percentage of benzyl alcohol and **b)** TOFs as a function of the substrate to catalyst ratio for all of the Au and $Au/CeO_2$ catalytic systems studied. The square data points (■) represent reactions which were performed in air, while the triangular data points (▲) represent reactions which were performed under a constant flow of $O_2$ (g).

As was stated in Section 1.3.2, as a support, ceria can help to increase the overall activity of the supported NPs by storing and releasing oxygen, forming surface and bulk vacancies, and affecting the dispersion of supported metal NPs.[45] Surprisingly, however, the $Au/CeO_2$ NC catalysts showed similar activity to their bulk counter-parts, indicating that the nanostructure of the ceria was not playing a profound role during the catalytic reactions. This was an intriguing outcome as it has been proposed that the redox properties of ceria are both size and shape dependent.[46] Based on these catalytic results, it is suggested here that the ceria NCs are acting very similar to bulk ceria because of how the supports interact with the Au NPs. As mentioned in Section 3.3.2.2, a clear TEM image which allowed for the contrast of Au and ceria NCs in the $Au/CeO_2$ NC system (*c.f.* Figure 3.4e) was unobtainable, so the true nature of the particles remains a mystery. Figure 3.9 illustrates another TEM image of the $Au/CeO_2$ NC system. From this image, it is very hard to distinguish whether the observed particles are ceria NCs, Au NPs, or both. It is evident that further investigation is needed in order to optimize the $Au/CeO_2$ NC catalytic system.

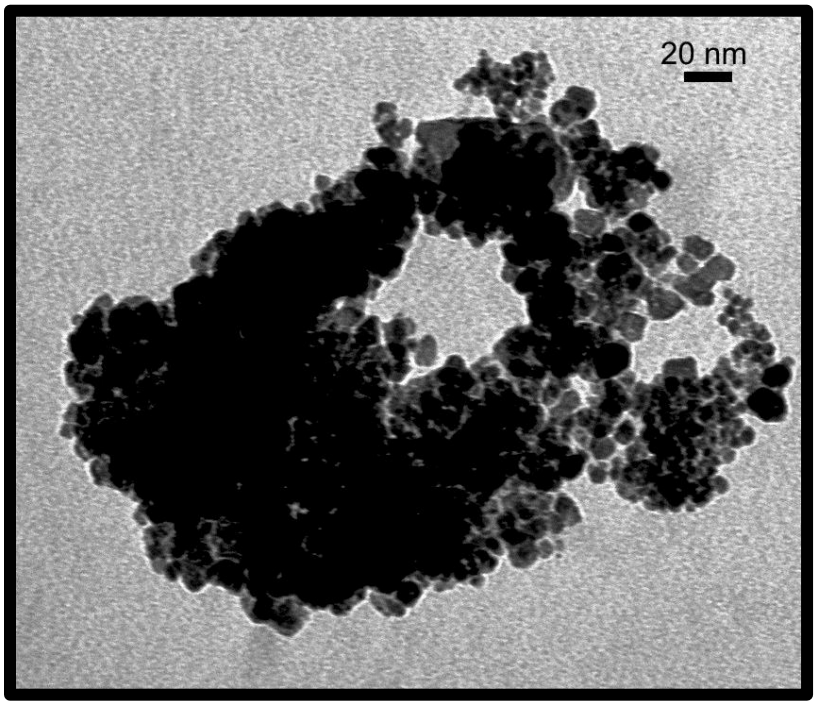


**Figure 3.9:** TEM image of the $Au/CeO_2$ NC catalytic system

### 3.3.4. Au $L_3$-edge XAS

Au $L_3$-edge XAS spectra were collected from the Au/bulk $CeO_2$ and $Au_{25}(SR)_{18}$/bulk $CeO_2$ catalytic systems described in the previous sections. The Au/bulk $CeO_2$ system had a 2.7 wt% Au loading and was calcined at 200 °C, while the $Au_{25}(SR)_{18}$/bulk $CeO_2$ system had a 2.8 wt% Au loading and was calcined at 350 °C. Both systems were analyzed prior to any catalytic reaction to see how their properties differed. After reaction, it was observed that the Au/bulk $CeO_2$ catalyst was much more active towards the oxidation of benzyl alcohol than the $Au_{25}(SR)_{18}$/bulk $CeO_2$ catalyst.

The white line in the Au $L_3$-edge XANES spectra arises from the transition of Au $2p_{3/2}$ electrons into unoccupied Au $5d_{5/2,3/2}$ states present above the Fermi level.[110] Figure 3.10 depicts the normalized Au $L_3$-edge XANES spectra from the two catalytic systems, as well as from the Au foil standard. It can be noted that both catalytic systems exhibit similar spectral features as that of bulk Au (foil), with some small differences. The white line intensity shows a slight increase from bulk Au < $Au_{25}(SR)_{18}$/bulk $CeO_2$ < Au/bulk $CeO_2$. These differences can be attributed to the possible electron redistribution in the Au 5d states just above the Fermi level.[110,111] This redistribution is very complex and will only be briefly touched on here. It has been previously reported that a more intense white line, relative to bulk Au, indicates an increase in the unoccupied Au 5d states just above the Fermi level.[111] Zhang *et al.* have established that smaller (capped) Au NPs show an increased white line intensity due to the increased surface area (*i.e.* a surface effect).[111] Recall that the Au NPs in the Au/bulk $CeO_2$ system studied here are slightly smaller (2.4 ± 0.5 nm) than those in the $Au_{25}(SR)_{18}$/bulk $CeO_2$ system (3.0 ± 0.5 nm), and hence show an increased white line intensity; as seen in Figure 3.4. It is proposed here that the smaller Au NPs in the Au/bulk $CeO_2$ system might have a slightly stronger metal-support interaction than those in the $Au_{25}(SR)_{18}$/bulk $CeO_2$ system. This could account for the lack of catalytic activity in the latter system.

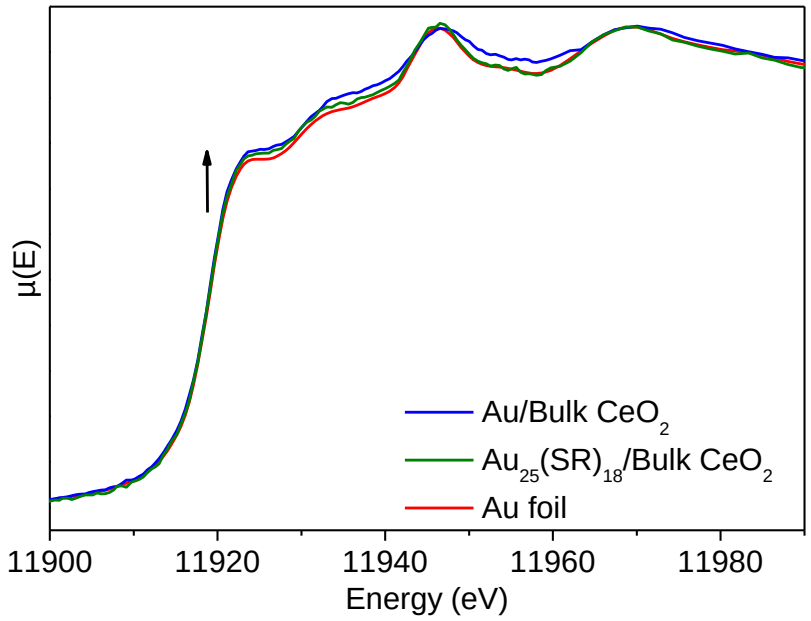


**Figure 3.10:** Au $L_3$-edge XANES spectra from the Au/bulk $CeO_2$ and $Au_{25}(SR)_{18}$/bulk $CeO_2$ catalysts, along with the Au foil standard. The arrow indicates the increase in white line intensity from Au foil to the Au/bulk $CeO_2$ catalyst.

To provide further insight into the local atomic environment of the two catalytic systems, the Au $L_3$-edge EXAFS spectra were collected. The EXAFS spectra in R space and the fitting results are presented in Figure 3.11 and Table 3.7, respectively. The Au/bulk $CeO_2$ system exhibited a lower coordination number (CN) than the $Au_{25}(SR)_{18}$/bulk $CeO_2$ system; 9.9 ± 1.5 compared to 12.7 ± 2.5. This indicated that the Au NPs in the Au/bulk $CeO_2$ system were smaller than those in the other system, which confirms the TEM results (Section 3.3.2.2). It was also evident from these fitting results that the $Au_{25}(SR)_{18}$ MPCs exhibited bulk-like behavior; as the CN of bulk fcc Au is 12. Unfortunately, due to time and sample constraints on the HXMA beamline, *k* data could only be collected up to a *k* value of 12. The inherent error in the CN and the Au-Au bond length ($R_{Au\text{-}Au}$) values could likely be lowered with higher *k*-range data. That being said, the aforementioned general trends were still apparent.

From the EXAFS fits, it is also clear that there is no Au-S contribution in the $Au_{25}(SR)_{18}$/bulk $CeO_2$ catalytic system. It has been previously reported that the Au-S contribution in $Au_{25}(SR)_{18}$ MPCs appears at ~ 1.9 – 2.3 Å, in R-space, as a sharp peak.[109] As this peak is absent from the collected EXAFS spectra, it is evident that the thiolate ligands have been completely removed from the system after calcination at 350 °C, and therefore are not poisoning their potential catalytic activity. It appears that since the MPCs are exhibiting bulk-like character (*i.e.* CNs near 12), the potential to oxidize benzyl alcohol with this system is small, especially since it is known that bulk Au is catalytically inert.[49]

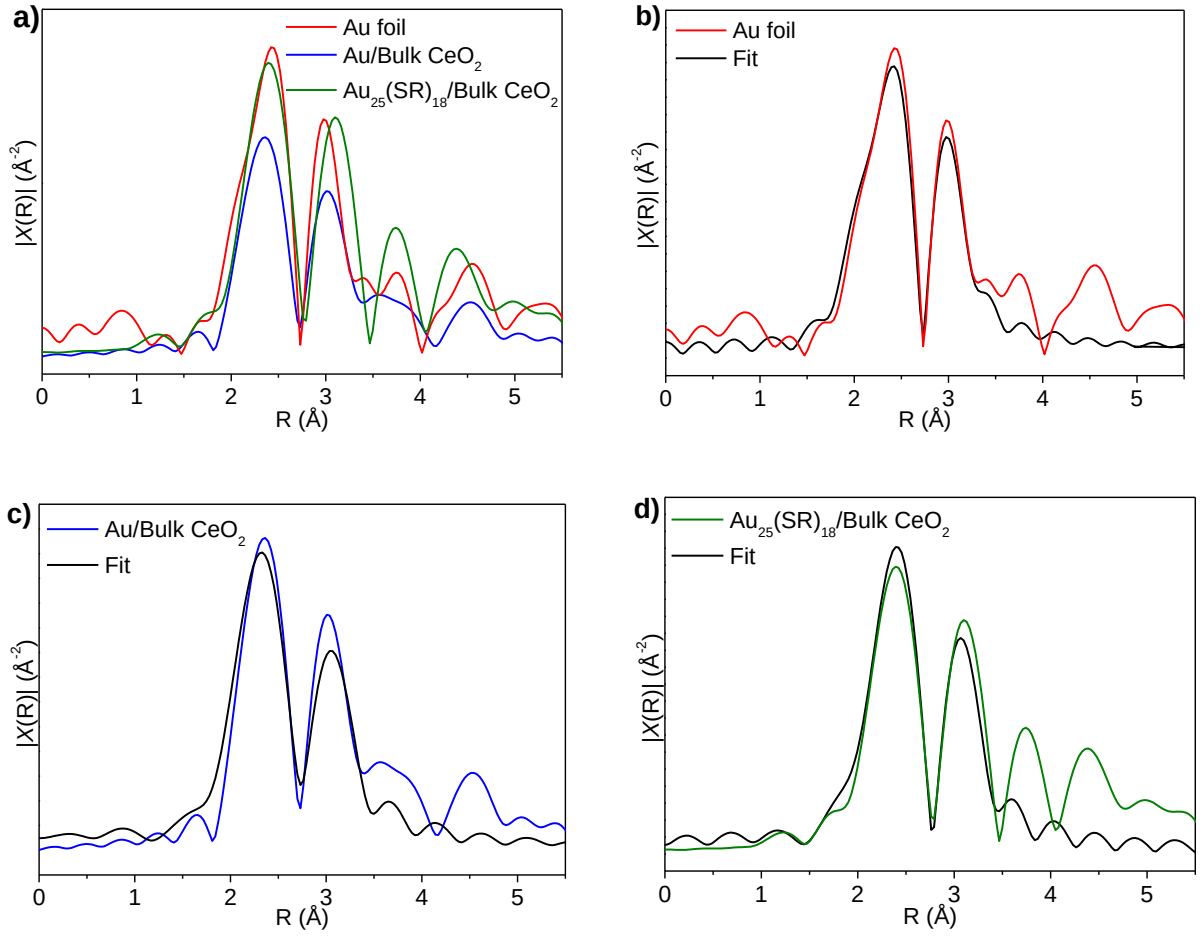


**Figure 3.11:** Au $L_3$-edge EXAFS spectra in R-space from **a)** Au foil, Au/bulk $CeO_2$ and $Au_{25}(SR)_{18}$/bulk $CeO_2$ catalysts, and **b – d)** theoretical fitting of Au foil, Au/bulk $CeO_2$ and $Au_{25}(SR)_{18}$/bulk $CeO_2$ catalysts, respectively. R-range fitting window: 1.85 – 3.45 Å.

**Table 3.7:** EXAFS fitting parameters for the $Au/CeO_2$ catalysts and the Au foil standard obtained from Artemis.[89]

| Sample | *k*-range ($Å^{-1}$) | CN | $R_{Au-Au}$ (Å) | $\sigma^2$ ($Å^2$) | $E_0$ shift (eV) | R factor |
|---|---|---|---|---|---|---|
| **Au foil** | 2.5 - 11.5 | 12 [a] | 2.861 ± 0.005 | 0.008 ± 0.001 | 3.6 ± 0.6 | 0.012 |
| **Au/bulk $CeO_2$** | 2.5 - 10.5 | 9.9 ± 1.5 | 2.845 ± 0.013 | 0.011 ± 0.002 | 5.0 ± 0.9 | 0.026 |
| **$Au_{25}(SR)_{18}$/bulk $CeO_2$** | 2.5 - 9.0 | 12.7 ± 2.5 | 2.883 ± 0.015 | 0.008 ± 0.003 | 5.8 ± 1.1 | 0.024 |

*a.* Fixed / set value for a Au fcc model

# 3.4. Conclusions

In conclusion, the activity of a variety of Au, $CeO_2$ and $Au/CeO_2$ catalysts has been studied through the oxidation of benzyl alcohol. During the analysis of the $^1H$ NMR spectra of the final reaction mixtures, it was determined that both bulk and NC ceria were not active catalysts for this reaction. It was also determined that Au NPs, Au/bulk $CeO_2$ and $Au/CeO_2$ NC systems, in the presence of $K_2CO_3$ and water, were active catalysts for this oxidation reaction at 60 °C in both an air and $O_2$ (g) atmosphere. Through the examination of a large number of oxidation reactions utilizing the Au/bulk $CeO_2$ catalytic system, it was found that a substrate to catalyst ratio of ~ 1500:1 was an ideal ratio as the reactions were not mass-transport limited under these conditions, with respect to the $O_2$ (g) in the system. It was also found that the catalytic activity was not overly affected by an increase in either calcination or reaction temperatures, while deactivation was apparent over time. Nevertheless, the TOFs of the active supported catalysts were all approximately double those of the unsupported Au NPs. Interestingly, it was established that that $Au/CeO_2$ NC catalysts showed very similar activity as the corresponding bulk system. This was attributed to the differing interactions between the Au NPs and the ceria support in both systems. Another surprising result was the fact that the synthesized $Au_{25}(SR)_{18}$/bulk $CeO_2$ catalysts were not active towards benzyl alcohol oxidation reactions under any of the conditions tested. This system, along with the active Au/bulk $CeO_2$ system, was further examined through the use of Au $L_3$-edge XANES and EXAFS. The spectra revealed that the catalysts exhibited different local coordination environments which could be

attributing to their contrast in catalytic activity; that is, that the $Au_{25}(SR)_{18}$/bulk $CeO_2$ catalysts have few, if any, under-coordinated surface sites available for catalysis.

This study has shown that when utilizing optimized reaction conditions, one can successfully compare the catalytic activities of a variety of different systems. It has also been shown that the addition of a ceria support greatly enhances the catalytic activity of the supported Au NPs. Furthermore, the utilization of supported ultra-small $Au_{25}(SR)_{18}$ MPCs did not show any activity towards the examined reactions, despite their small size (~ 1 nm before calcination).[57] This signified that the activation of such species for catalysis is a non-trivial task and that more work needs to be performed to understand how the MPCs can be activated for catalysis while retaining a significant number of active Au sites for catalysis.

# Chapter 4

# Conclusions

## 4.1. Summary

The work presented in this thesis describes the investigation of several ceria-based materials and their various properties. Chapter 2 examined the electronic properties of monodisperse ceria NCs through the use of high resolution X-ray characterization techniques, including XPS and XANES. The purpose of this study was to determine how the relative concentration of $Ce^{3+}$ ([$Ce^{3+}$]) changed with changes in the particle size, sample fraction, and the Ce precursor used during synthesis. This was an important study as there was contradictory information in the primary literature as to whether the Ce oxidation state varied on the surface of these nanostructures.[19,79,80] The presence of higher levels of $Ce^{3+}$, and thus oxygen vacancies, on the surface of the NPs has large implications in the potential applications of these ceria-based materials. The application of ceria supports decorated with Au NPs to catalysis was explored in Chapter 3. The catalytic activity of several Au, ceria, and $Au/CeO_2$ systems was analyzed through the oxidation of benzyl alcohol, and studied by XAS. The conclusions of the two studies presented in this thesis are summarized in the following sub-sections, followed by implications and future work in Sections 4.2 and 4.3, respectively.

### 4.1.1. Electronic Properties

The electronic properties of hydrothermally-synthesized ceria NCs were investigated in Chapter 2. High resolution XPS was used to characterize the presence of multiple oxidation states within the materials. Upon analysis of the Ce 3d core-line XPS spectra collected after a single sweep, it was determined that the [$Ce^{3+}$] within the ceria NCs was independent of the particle size and Ce precursor used. The calculated values ranged from ~ 7 to < 10 % regardless of the tested conditions. During this analysis, it became evident that the samples were becoming damaged / photoreduced over time. This was confirmed by comparing the aforementioned Ce 3d

XPS spectra with those that were collected after averaging 20 sweeps of each spectrum. These Ce 3d XPS spectra indicated that $Ce^{4+}$ was being reduced with increasing X-ray exposure. Interestingly, it was also found that the degree of reduction was also independent of the individual sample conditions, as the calculated [$Ce^{3+}$] values ranged from ~ 16 to 21 % for the samples tested. To determine if this damage / photoreduction was occurring throughout the samples, Ce 4d XPS spectra were collected. It was determined that the X-ray induced damage occurred more at the surface of the ceria NC samples, validating previously reported results.[82]

To further investigate the electronic structure of the synthesized ceria NCs, Ce $M_{4,5}$- and $N_{4,5}$-edge XANES spectra were collected. From these spectra it was evident that the ceria NC samples were experiencing a higher degree of $Ce^{4+}$ photoreduction (damage) than the collected XPS spectra. It was shown that the increased brightness of synchrotron radiation used to collect the XANES spectra reduced the $Ce^{4+}$ located at the surface of the ceria NCs much more rapidly than when laboratory-based XPS experiments were performed. This was confirmed by detuning the undulator of the SGM beamline to examine the effects that both a high and low photon flux had on the samples. It was demonstrated that the higher the photon flux, (*i.e.* the higher the intensity of the X-ray beam), the greater the observed reduction of $Ce^{4+}$ within the samples.

The findings of this study demonstrate that high resolution XPS is an extremely useful technique for examining the electronic structure of ceria NCs. It has been conclusively shown that the [$Ce^{3+}$] within the ceria NC samples is independent of all of the tested sample conditions, *i.e.* particle size and Ce precursor used during synthesis. It has also been shown that increased exposure to high intensity X-ray radiation damages the NCs by reducing the surface $Ce^{4+}$ to $Ce^{3+}$ over time. This indicates that even though X-ray characterization techniques can provide invaluable electronic / structural information, the way in which the spectra are collected is extremely important in order to prevent artifacts in the data related to beam damage. These results will add to the development of a more profound understanding of the properties of ceria nanostructures.

## 4.1.2. Catalytic Applications

The catalytic activity of many Au and ceria systems was explored in detail in Chapter 3. The ceria NCs which were studied in Chapter 2 were investigated as potential catalysts for the aqueous phase oxidation of benzyl alcohol to benzaldehyde. Through the analysis of the resulting $^{1}$H NMR spectra, the relative yields and TOFs of each reaction could be calculated utilizing the integrations of the desired product peaks. In doing this, it was determined that neither bulk ceria nor ceria NCs were active catalysts for this oxidation reaction. It was also determined that the addition of Au into the system greatly enhanced the overall catalytic activity of the system. Polymer-stabilized Au NPs, Au/bulk $CeO_2$ and Au/$CeO_2$ NCs were found to be active catalysts for the conversion of benzyl alcohol to benzaldehyde, benzoic acid and benzyl benzoate under mild oxidative conditions. It was also found that the optimized reaction conditions took place at 60 °C in the presence of $K_2CO_3$ and water in both air and $O_2$ (g) atmospheres.

The Au/bulk $CeO_2$ catalytic system was the most comprehensively studied. It was established in this study that at (or above) a substrate to catalyst ratio of ~ 1500:1, the system was no longer restricted by mass-transport limitations with respect to $O_2$ (g). It was also ascertained that the catalytic activity of this system was not affected by changes in the calcination or reaction temperatures. The activity did, however, decrease over time, indicating that some deactivation had occurred. In comparison to the unsupported Au NP catalysts, the TOFs of the Au/bulk $CeO_2$ catalysts were approximately doubled when similar conditions were employed. This proved that the ceria support played an important role during the catalytic reaction. Interestingly, it was found that the Au/$CeO_2$ NC catalysts demonstrated similar catalytic activities as the Au/bulk $CeO_2$ system.

To investigate whether ultra-small Au MPCs could be used to generate efficient Au/$CeO_2$ catalysts, a variety of different $Au_{25}(SR)_{18}$/bulk $CeO_2$ systems were studied. Disappointingly, it was determined that these systems were not active towards the oxidation of benzyl alcohol under any of the tested conditions. To develop a better understanding of why this was the case, Au $L_3$-edge XANES and EXAFS spectra were collected on the activated $Au_{25}(SR)_{18}$/bulk $CeO_2$ system, as well as the catalytically active Au/bulk $CeO_2$ system. The spectra revealed that the Au NPs in the Au/bulk $CeO_2$ system were smaller than those in the $Au_{25}(SR)_{18}$/bulk $CeO_2$ system,

confirming the results obtained by TEM, and that the latter system exhibited bulk-like characteristics. The supported Au MPC system exhibited very similar spectral features as that of the bulk Au standard, which may indicate why no catalytic activity was observed in this Au MPC system as bulk Au is known to be catalytically inert.[49]

## 4.2. Significance and Implications

Taken together, the studies presented in Chapters 2 and 3 help to provide a better understanding of the intricate properties of certain ceria nanostructures. More specifically, the role of the [$Ce^{3+}$] on the surface of (002)-terminated ceria NCs which can significantly affect catalytic applications. As mentioned in Section 4.1.1, it was determined that the [$Ce^{3+}$] on the surface of ~ 3 – 10 nm ceria NCs was independent of the particle size. It is known that the degree of oxygen vacancies / defects at the surface of NPs affects how easily the particles can reversibly absorb and release oxygen, which therefore affects the potential catalytic activity of the NPs.[2] The results presented here show that there are similar levels of $Ce^{3+}$ on the surface of both small and larger particles. This implies that even though smaller particles have a larger surface area, and therefore a larger number of possible defect sites, their potential catalytic activity would be similar to that of the larger particles. This was confirmed in the analysis of the benzyl alcohol oxidation reactions performed using the Au/bulk $CeO_2$ and Au/$CeO_2$ NC catalytic systems. It was found that under comparable conditions, both systems exhibited very similar catalytic activities.

An extensive systematic study of the differences between Au/bulk $CeO_2$ and Au/$CeO_2$ NC catalytic systems has yet to be performed in the literature. It has been previously shown, however, that Au NPs (2 – 5 nm) supported on nanocrystalline ceria (~ 5 nm) are much more catalytically active than Au NPs supported on conventional (bulk) ceria for the oxidation of 3-octanol, with TOFs of ~ 425 $h^{-1}$ and ~ 150 $h^{-1}$, respectively.[51] That being said, the nanocrystalline ceria support used in the prior study did not have defined corners and edges, as the ceria NCs studied here do. These important features could be the reason for the observed differences in electronic and catalytic properties of the ceria nanostructures studied here with those from the previous report.[51] Although Au/$CeO_2$ NCs and Au/$CeO_2$ nanorods (NRs) have also been

previously shown to be active benzyl alcohol oxidation catalysts, with TOFs of 193 $h^{-1}$ and 108 $h^{-1}$, respectively, the referenced study did not include a comparison to the bulk ceria counter-part.[55] The Au NPs and ceria nanostructures described in this previous study were also much larger than those studied here; with Au NPs in the range of 2 – 8 nm, ceria NCs ranging from 20 – 60 nm, and ceria NRs with a broad length distribution between 30 – 200 nm.[55] Due to the large size of these nanostructures, it is difficult to make a comparison with the results obtained in this thesis. Therefore, the findings presented here imply that the addition of a ceria NC support does not advantageously affect the catalytic activity of the supported Au NPs. Nevertheless, a definite conclusion has yet to be made and a more in-depth study is required, as will be discussed in Section 4.3.2.

While the use of ultra-small Au MPCs as catalysts has gained significant interest over the past few years, this thesis has shown that activating these clusters for catalysis may be a more difficult task than suggested by supporting literature.[56,57,109] Numerous attempts were made during this thesis to synthesize $Au_{25}(SR)_{18}/CeO_2$ composites using previously reported procedures.[56,57] TEM results (*c.f.* Figure 3.4d) show that this has been accomplished, with slight growth of Au NPs occuring after calcination. After analysis of the benzyl alcohol oxidation reactions, however, it was found that the synthesized $Au_{25}(SR)_{18}/CeO_2$ systems were not catalytically active under any of the conditions tested. As stated in Section 4.1.2, the collected XANES and EXAFS spectra revealed that the Au MPCs exhibited bulk-like characteristics, indicating that they were not in fact 'nanoclusters'. Many of the previously published studies do not include TEM analyses of the Au MPCs once they have been calcined and supported on a metal oxide support (*i.e.* activated for catalysis).[56,112] This leads one to question whether or not the Au MPCs were still present after high-temperature treatments or if larger Au NPs had formed. With that in mind, the aforementioned studies did show an increased catalytic activity of the supported 'Au MPC' systems as compared to typical Au NPs, indicating that activation should be possible.[56,57,109,112] Although it is clear that other researchers have successfully activated Au MPCs for catalytic reactions in the past, it does not appear to be a trivial task.[56,112] Further optimization of the $Au_{25}(SR)_{18}/CeO_2$ system is needed in order to activate the particles and successfully oxidize benzyl alcohol.

## 4.3. Future Work

This thesis has provided indispensible information regarding the electronic and catalytic properties of various ceria-based materials. Nonetheless, further experimentation is required to make any significant conclusions on the catalytic applications of the systems studied here. The following sub-sections describe the proposed directions of future research; including enhanced characterization and optimization of the systems studied here, as well as additional experiments that would add value to this work.

### 4.3.1. Characterization and Optimization of the $Au/CeO_2$ Catalytic Systems

The ability to image NPs is an extremely useful characterization tool as it allows one to visualize the morphology and particle distribution of the system under investigation. Throughout this thesis, conventional bright field (BF) TEM images were taken of all of the synthesized NPs. As was noted in Chapter 3, it is hard to distinguish between Au and ceria using BF TEM imaging, therefore increasing the error in the measured particle sizes. To gain more insight into the size distribution and dispersion of the Au NPs on the ceria supports in the studied $Au/CeO_2$ catalytic systems, it would be extremely beneficial to take high resolution dark field (DF) TEM images. As Au has a higher Z value than Ce (and O), the Au NPs would appear brighter than the ceria support (*c.f.* Section 1.4.1). This would be useful when imaging the $Au/CeO_2$ NC system. TEM images could also be taken of the systems after catalytic reactions to see how / if they have changed. Such a study would provide more insight into how the particles interact with each other, and if the particles can be recovered after reaction. Once DF TEM images of the $Au/CeO_2$ NC system are collected, further future work on the optimization of the system could be pursued, including the prevention of either Au or ceria sintering / agglomeration after calcination.

Although the collected Au $L_3$-edge XANES and EXAFS spectra presented in Chapter 3 (Section 3.3.4) provided some information on the electronic structure of the synthesized Au/bulk $CeO_2$ and $Au_{25}(SR)_{18}$/bulk $CeO_2$ catalytic systems, more data could be collected to complete the picture. In studying these two catalytic systems, it might be useful to collect spectra from

samples which were calcined at similar temperatures and before and after catalytic reactions have taken place. It would also be beneficial to collect multiple scans of each spectrum to increase the signal to noise ratio of both the XANES and EXAFS portions of the spectrum. EXAFS spectra should be collected to a higher value of *k* to increase the resolution of the data. The differences in the coordination environments and oxidation states of the two Au species (NPs and MPCs) could then be quantified. If all of this was accomplished, the obtained results would give a more accurate picture as to why the Au/bulk $CeO_2$ system was catalytically active towards the oxidation of benzyl alcohol while the $Au_{25}(SR)_{18}$/bulk $CeO_2$ system was not. Another interesting study would be to look at how the [$Ce^{3+}$] on the surface of the ceria support is affected by the addition of Au NPs or MPCs. As in Chapter 2, Ce 3d and 4d XPS spectra could be collected from the two catalytic systems to investigate if the observed catalytic activity correlates with an increased [$Ce^{3+}$]. Au 4f XPS spectra could also be collected to add to this investigation.

### 4.3.2. Additional Catalytic Experiments

Using the Au/bulk $CeO_2$ catalyst in the presence of $O_2$ with a substrate to catalyst ratio of ~ 450:1, it was found that benzyl alcohol was selectively oxidized to benzoic acid with 100% conversion (*c.f.* Table 3.5). This was an interesting result as it has been previously shown that benzaldehyde is typically the major product.[105] Investigating how the selectivity of the reaction can be controlled through altering various reaction conditions would be an interesting future study. Testing the recyclability of the Au/$CeO_2$ catalytic systems would also prove to be a valuable future study.

This thesis solely focused on catalysts which could oxidize benzyl alcohol under mild aqueous (and basic) conditions. Future work should focus on analyzing the versatility of the catalyst using other substrates. As benzyl alcohol is a primary alcohol, both secondary and tertiary alcohols could be tested to see how the catalytic activity is affected. Initially, substrates in the same family could be tested, for example, α-methylbenzyl alcohol and α,α -dimethylbenzyl alcohol to see how the addition of each methyl group would affect the activity of the reaction. Any number of mono-, di- and tri-substituted alcohols could then be tested and analyzed, for example, 1-butanol, 2-butanol, 2-buten-1-ol, and 1,4-butanediol.[106] While testing

the versatility of the $Au/CeO_2$ catalytic systems, it would be interesting to also examine the activity towards the oxidation of CO. There have been many previous reports on how nanostructured ceria and $Au/CeO_2$ composites are highly catalytically active towards the oxidation of CO.[46,48,49,55,56,112] This study would add great value to the work that has already been accomplished in this thesis.

This thesis has investigated several ceria- and $Au/CeO_2$-based materials and has described their electronic properties and catalytic applications with the aim to promote a deeper and more profound understanding of the observed changes. Some additional experiments have been proposed for future studies to help complete the overall picture. These further studies will allow for a more in-depth understanding and refinement of the catalytic systems developed in this work.

# References


1. C. Sun; H. Liab; L. Chen. *Energy Environ. Sci.*, **2012**, 5, 8475–8505.
2. R. Rao; B.G. Mishra. *Bull. Catal. Soc. India.* **2003**, 2, 122-134.
3. P.X. Huang; F. Wu; B.L. Zhu; X. P. Gao; H. Y. Zhu; T.Y. Tan; W.P. Huang; S.H. Wu; D.Y. Song. *J. Phys. Chem. B.* **2005**, 109, 19169-19174.
4. X. Nie; H. Qian; Q. Ge; H. Xu; R. Jin. *ACS Nano.* **2012**, 6, 6014-6022.
5. H.C. Yao; Y.F. Yu Yao. *J. Catal.* **1984**, 86, 254-265.
6. E.P. Murray; T. Tsai; S.A. Barnett. *Nature.* **1999**, 400, 649-651.
7. V. V. Kharton; F. M. Figueiredo; L. Navarro; E.N. Naumovich; A.V. Kovalevsky; A.A. Yaremchenko; A.P. Viskup; A. Carneiro; F.M.B. Marques; J.R. Frade. *J. Mater. Sci.* **2001**, 36, 1105-1117.
8. N. Izu; W. Shin; I. Matsubara; N. Murayama. *Sens. Actuators, B.* **2003**, 94, 222-227.
9. P. Palmisano; S.P. Hernandez; M. Hussain; D. Fino; N. Russo. *Chem. Eng*. **2011**, 176–177, 253-259.
10. S. Yabe; T. Sato. *J. Solid State Chem.* **2003**, 171, 7-11.
11. J. Kaspar; P. Fornasiero; M. Graziani. *Catal. Today.* **1999**, 50, 285-298.
12. N. Guillen-Hurtado; V. Rico-Perez; A. Garcia-Garcia; D. Lozano-Castello; A. Bueno-Lopez. *Dyna.* **2012**, 79, 114-121.
13. R. Di Monte; J. Kaspar. *Top. Catal.*. **2004**, 28, 47-57.
14. N.Q. Minh. *Solid State Ionics***. 2004**, 174, 271–277.
15. S.C. Singhal. *Solid State Ionics***. 2000**, 135, 305–313.
16. S.D. Park; J.M. Vohs; R.J. Gorte. *Nature*. **2000**, 404, 265–267.
17. D. Zhang; F. Niu; H. Li; L. Shi; J. Fang. *Powder Technol.* **2011**, 207, 35-41.
18. S. Yang; L. Gao. *J. Am. Chem. Soc.* **2006**, 128, 9330-9331.
19. C. Paun; O.V. Safornova; J. Szlachetko; P.M. Abdala; M. Nachtegaal; J. Sa; E. Kleymenov; A. Cervellino; F. Krumeich; J.A. van Bokhoven. *J. Phys. Chem. C.* **2012**, 116, 7312-7317.
20. H-L. Lin; C-Y. Wu; R-K. Chiang. *J. Colloid Interface Sci*. **2010**, 341, 12-17.
21. T. Yu; J. Joo; Y.I. Park; T. Hyeon. *Angew. Chem*. **2005**, 117, 7577-7580.
22. S. Samiee; E.K. Goharshadi. *Mater. Res. Bull.* **2012**, 47, 1089–1095.

23. G.Z. Cao; Y. Wang. *Nanostructures & Nanomaterials: Synthesis, Properties & Applications*. London: Imperial College Press, **2004**. Print.
24. V.M. Rotello. *Nanoparticles: Building Blocks for Nanotechnology*. New York: Springer Science + Business Media, Inc, **2004**. Print.
25. M. Yoshimura; K. Byrappa. *J. Mater. Sci.* **2008**, 43, 2085–2103.
26. A. Trovarelli. *Catalysis by Ceria and Related Materials.* London: Imperial College Press, **2002**. Print.
27. T. Adschiri; K. Arai K; Y-P. Sun (ed). *Supercritical fluid technology in materials science and engineering*. New York: Marcel Dekker Inc., **2002**, Print.
28. J. Zhang; S. Ohara; M. Umetsu; T. Naka; Y. Hatakeyama; T. Adschiri. *Adv. Mater.*, **2007**, 19, 203–206.
29. M. Kakihana. *J. Sol-Gel Sci. Technol.* **1996**, 6, 7-55.
30. D. Zhang; X. Du; L. Shi; R. Gao. *Dalton Trans.* **2012**, 41, 14455-14475.
31. X.-M. Liu; W-L. Gao; J. Zhang. *J. Phys. Chem. Sol.* **2011**, 72, 1472–1476.
32. Y. Zhang; F. Hou; Y. Tan. *Chem. Commun*., **2012**, 48, 2391–2393.
33. L. Liao; H.X. Mai; Q. Yuan; H.B. Lu; J.C. Li; C. Liu; C.H. Yan; Z.X. Shen; T. Yu. *J. Phys. Chem. C*. **2008**, 112, 9061–9065.
34. K.B. Zhou; Z.Q. Yang; S. Yang. *Chem. Mater*. **2007**, 19, 1215–1217.
35. C. Sun; J. Sun; G. Xiao; H. Zhang; X. Qiu; H. Li; L. Chen. *J. Phys. Chem. B*. **2006**, 110, 13445–13452.
36. K.S. Lin; S. Chowdhury. *Int. J. Mol. Sci.* **2010**, 11, 3226–3251.
37. Q. Yuan; H.-H. Duan; L.-L. Li; L.-D. Sun; Y.-W. Zhang; C.-H. Yan. *J. Colloid Interface Sci*. **2009**, 335, 151–167.
38. H-X. Mai; L-D. Sun; Y-W. Zhang; R. Si; W. Feng; H-P. Zhang; H-C. Liu; C-H. Yan. *J. Phys. Chem. B.* **2005**, *109*, 24380-24385.
39. Z. Yang; T. K. Woo; M. Baudin; K. Hermansson. *J. Chem. Phys*. **2004**, 120**,** 7741-7749.
40. Q. Wu; F. Zhang; P. Xiao; H.S. Tao; X.Z. Wang; Z. Hu; Y.N. Lu. *J. Phys. Chem. C*. **2008**, 112, 17076–17080.
41. T. Taniguchi; K. Katsumata; S. Omata; K. Okada; N. Matsushita. *Cryst. Growth Des.* **2011**, 11, 3754–3760.
42. A. Wei. *Chem. Commun*. **2006**, 1581-1591.

43. I. Chorkendorff; J.W. Niemantsverdriet. *Concepts of Modern Catalysis and Kinetics, Second Edition.* Weinheim: Wiley-VCH Verlag GmbH & Co. KGaA, **2007**. Print.
44. P. Miedziak; M. Sankar; N. Dimitratos; J.A. Lopez-Sanchez; A.F. Carley; D.W. Knight; S.H. Taylor; C.J. Kiely; G.J. Hutchings. *Catal. Today*. **2011**, 164, 315–319.
45. A. Trovarelli. *Catal. Rev. Sci. Eng*. **1996**, 38, 439-520.
46. Tana; M. Zhang; J. Li; H. Li; Y. Li; W Shen. *Catal. Today.* **2009**, 148, 179–183.
47. Z. Yang; T. K. Woo; M. Baudin; K. Hermansson. *J. Chem. Phys*. **2004,** 120**,** 7741-7749.
48. M. Haruta; T. Kobayashi; H. Sano; N. Yamada. *Chem. Lett.* **1987**, 405–408.
49. A. Corma; H. Garcia. *Chem. Soc. Rev.*, **2008**, 37, 2096–2126.
50. P. Haider; B. Kimmerle; F. Krumeich; W. Kleist; J. Grunwaldt; A. Baiker. *Catal. Lett.* **2008**, 125, 169–176.
51. A. Abad; P. Concepcion; A. Corma; H. Garcia. *Angew. Chem. Int. Ed.* **2005**, 44, 4066 – 4069.
52. Y. Azizi; C. Petit; V. Pitchon. *J Catal.* **2008**, 256, 338-344.
53. Q. Fu; H. Saltsburg; M. Flytzani-Stephanopoulos. *Science.* **2003**, 301, 935-938.
54. X-S. Huang; H. Sun; L-C. Wang; Y-M. Liu; K-N. Fan; Y. Cao. *Appl. Catal. B.* **2009**, 90, 224–232.
55. Y. Guan; D.A.J.M. Ligthart; O. Pirgon-Galin; J.A.Z. Pieterse; R.A. van Santen; E. J. M. Hensen. *Top Catal.* **2011**, 54, 424–438.
56. X. Nie; H. Qian; Q. Ge; H. Xu; R. Jin. *ACS Nano.* **2012**, 6, 6014-6022.
57. A. Shivhare; S.J. Ambrose; H. Zhang; R.W. Purves; R.W.J. Scott. *Chem. Commun.*, **2013**, 49, 276-278.
58. M. Zhu; C.M. Aikens; F.J. Hollander; G.C. Schatz; R. Jin. *J. Am. Chem. Soc.*, **2008**, 130, 5883–5885.
59. R.F. Egerton. *Physical Principles of Electron Microscopy: An Introduction to TEM, SEM, and AEM*. New York: Springer Science + Business Media Inc., **2005**. Print.
60. L. Reimer. *Transmission Electron Microscopy: Physics of Image Formation and Microanalysis*. Germany: Spinger-Verlag, **1993**. Print.
61. B. Fultz; J. Howe. *Transmission Electron Microscopy and Diffractometry of Materials*. Germany: Springer-Verlag, **2007**. Print.

62. C.B. Minella; E. Pellicer; E. Rossinyol; F. Karimi; C. Pistidda; S. Garroni; C. Milanese; P. Nolis; M.D. Baró; O. Gutfleisch *et al*. *J. Phys. Chem. C.* **2013**, 117, 4394-4403.

63. W. Rasband. Image J, Version 1.45s; National Institutes of Health: Bethesda, MD, **2011**. Available from rsbweb.nih.gov/ij/download/html.

64. D. Briggs. *Surface analysis of polymers by XPS and static SIMS*. Cambridge: Cambridge University Press, **1998**. Print.

65. J.C. Vickerman; I.S. Gilmore (eds.). *Surface analysis: the principal techniques*. Wiley, Chichester: Wiley, **2009**. Print.

66. O.I. Klyushnikov. *J. Structural Chemistry*. **1998**, 39, 1147-1150.

67. N. Fairley. CasaXPS, Version 2.3.16, Casa Software Ltd., Teighnmouth, Devon, UK, **2003** <www.casaxps.com>.

68. R.L. Martin; D.A. Shirley. *J. Chem. Phys.* **1976**, 64, 3685–3689.

69. P. van der Heide. *X-ray Photoelectron Spectroscopy: An Introduction to Principles and Practices*. New Jersey: John Wiley & Sons Inc., **2012**. Print.

70. X-ray Attenuation Length. <http://henke.lbl.gov/optical_constants/atten2.html>

71. J. Yano; V.K. Yachandra. *Photosynth. Res*. **2009**, 102, 241–254.

72. T.K. Sham. *Chemical Applications of Synchrotron Radiation: Part II: X-ray Applications*. Singapore: World Scientific Publishing Co. Pte. Ltd., **2002**, Print.

73. A. Owens. *Nucl. Instrum. Methods Phys. Res., Sect. A.* **2012**, 695, 1-12.

74. A.J. Achkar; T.Z. Regier; H. Wadati; Y.-J. Kim; H. Zhang; D. G. Hawthorn. *Phys. Rev. B.* **2011**, 83, 081106-1 – 081106-4.

75. A.J. Achkar; T.Z. Regier; H. Wadati; Y.-J. Kim; H. Zhang; D.G. Hawthorn. *Canadian Light Source, Instrumentation and Techniques, Activity Report*. **2009**, 158-159.

76. S. Tsunekawa; T. Fukuda; A. Kasuya. *Surf. Sci*. **2000**, 457, L437-L440.

77. F. Zhang; S.W. Chan; G.E. Spanier; E. Apak Q. Jin; R.D. Robinson; I.R. Herman. *Appl. Phys. Lett.* **2002**, 80, 127-129.

78. S. Turner; S. Lazar; B. Freitag; R. Egoavil; J. Verbeeck; S. Put; Y. Strauven; G. Van Tendeloo. *Nanoscale*, **2011**, 3, 3385-3390.

79. L. Wu; H.J. Wiesmann; A.R. Moodenbaugh; R.F. Klie; Y. Zhu; D.O. Welch; M. Suenaga. *Phys. Rev. B.* **2004**, 69, 125415-125423.

80. S.Y. Chen; Y.H. Lu; T.W. Huang; D.C. Yang; C.L. Dong. *J. Phys. Chem. C.* **2010,** 114, 19576–19581.

81. E. Paparazzo. *Surf. Sci.* **1990**, 234, L253-L258.

82. E. Paparazzo; G.M. Ingo; N. Zacchetti. *J. Vac. Sci. Technol., A.* **1991**, 9, 1416-1420.

83. F. Zhang; P. Wang; J. Koberstein; S. Khalid; S.W. Chan. *Surf. Sci.* **2004**, 563, 74-82.

84. PANalytical B. V. **2009**. X'Pert HighScore Plus. Version 3.0. Almelo, Netherlands.

85. A.P. Grosvenor; R.G. CavelL; A. Mar. *J. Solid State Chem.* **2007**, 180, 2702–2712.

86. T. Regier; J. Krochak; T.K. Sham; Y.F. Hu; J. Thompson; R.I.R. Blyth. *Nucl. Instrum. Methods Phys. Res., Sect. A,* **2007**, 582, 93–95.

87. A. Thompson; D. Attwood; E. Gullikson; M. Howells; K.J. Kim; J. Kirz; J. Kortright; I. Lindau; P. Pianetta; A. Robinson *et al*. X-Ray Data Booklet, Lawrence Berkeley National Laboratory, Berkeley, CA, **2009**.

88. Y.F. Hu; L. Zuin; R. Reininger; T.K. Sham. *AIP Conf. Proc.*, **2007**, 879, 535–538.

89. B. Ravel; M. Newville. *J. Synchrotron Radiat.,* **2005**, 12, 537–541.

90. G. Kaindl; G.K. Wertheim; G. Schmiester; E.V. Sampathkumaran. *Phys. Rev. Lett.* **1987**, 58, 606-609.

91. F. Larachi; J. Pierre; A. Adnot; A. Bernis. *Appl. Surf. Sci.* **2002**, 195, 236-250.

92. P. Burroughs; A. Hamnett; A.F. Orchard; G. Thornton. *J. Chem. Soc. Dalton Trans.* **1976**, 17, 1686-1698.

93. D.R. Mullins; S.H. Overbury; D.R. Huntley. *Surf. Sci.* **1998**, 409, 307-319.

94. A.P. Grosvenor; R.G. Cavell; A. Mar. *Phys. Rev. B.* **2006**, 74, 125102-125111.

95. D.D. Sarma; P. Vishnu Kamath; C.N.R. Rao. *Chem. Phys.* **1983**, 73, 71–82.

96. M.L. Trudeau; A. Tschope; J.Y. Ying. *Surf. Interf. Anal.* **1995**, 23, 219-226.

97. D.E. Ramker; C.T. White; J.S. Murday. *J. Vac. Sci. Technol.* **1981**, 18, 748-749.

98. S. Tanuma; C.J. Powell; D.R. Penn. *Surf. Interf. Anal.,* **1994**, 21, 165-176.

99. S. Tougaard. QUASES – IMFP – TPP2M. Quases-Tougaard Inc. 2000-2010.

100. S.O. Kucheyev; B.J. Clapsaddle; Y.M. Yang; T. van Buuren; A.V Hamza. *Phys. Rev. B.* **2007**, 76, 235420-235424.

101. J.B. Parise; G.E. Brown Jr. *Elements*. **2006**, 2, 37-42.

102. A. Owens. *Nucl. Instrum. Methods Phys. Res., Sect. A.* **2012**, 695, 1-12.

103. M. Alhumaimess; Z. Lin; W. Weng; N. Dimitratos; N.F. Dummer; S.H. Taylor; J.K. Bartley; C. J. Kiely; G.J. Hutchings. *Chem Sus Chem*. **2012**, 5, 125 – 131.

104. V.R. Choudhary; D.K. Dumbre. *Ind. Eng. Chem. Res.* **2009**, 48, 9471–9478.

105. S. Mandala; K.K. Bandob; C. Santraa; S. Maityc; O.O. James; D. Mehtad; B. Chowdhurya. *Applied Catalysis A: General*. **2013**, 452, 94– 104.

106. W. Hou; N. A. Dehm; R. W. J. Scott. *J. Catal*. **2008**, 253, 22-27.

107. H. E. Gottlieb; V. Kotlyar; A. Nudelman. *J. Org. Chem*. **1997**, 62, 7512-7515.

108. J. Lv; Y. Shen; L. Peng; X. Guo; W. Ding. *Chem. Commun.*, **2010**, 46, 5909–5911.

109. A. Shivhare; D.M. Chevrier; R.W. Purves; R.W.J. Scott. *J. Phys. Chem. C*. **2013**, Submitted manuscript.

110. A. Bzowski; Y.M. Yiu; T.K. Sham. *Phys. Rev. B.* **1995**, 51, 9515-9520.

111. P. Zhang; T.K. Sham. *Phys. Rev. Let.* **2003**, 90, 245502-1 – 245502-4.

112. G. Li; R. Jin. *Acc. Chem. Res.* **2013**, 46, 1749-1758.